MEASUREMENT OF ATMOSPHERIC CONCENTRATION OF CO_2 IN THE HUDSON BAY LOWLANDS: AN APPLICATION OF A LAGRANGIAN PARTICLE DISPERSION MODEL (STILT)

OLALEKAN BALOGUN

A THESIS SUBMITTED TO

THE FACULTY OF GRADUATE STUDIES

IN PARTIAL FULFILLMENT OF THE REQUIREMENTS

FOR THE DEGREE OF MASTER OF SCIENCE

GRADUATE PROGRAM IN GEOGRAPHY

YORK UNIVERSITY

TORONTO, ONTARIO

DECEMBER 2015

ABSTRACT

Much of our understanding of the terrestrial carbon cycle comes from measurements of atmospheric CO_2 mixing ratios on continental towers and the inferred terrestrial fluxes needed to match the observations. The surface flux information retrieved from CO_2 concentrations at tower sites contain an integrated signal of CO_2 exchange representing footprint areas of 10^3–10^4 km^2. Atmospheric CO_2 concentrations are modified not only by surface sources and sinks, but also by horizontal advection and vertical mixing on the way to the measurement tower. The capability of transport models to accurately represent air parcel trajectories and concentration footprints is crucial in inverse analysis. This study employs the Stochastic Time-Inverted Lagrangian Transport model (STILT) driven by meteorological inputs from the North American Regional Reanalysis (NARR), and coupled with the CarbonTracker data assimilation system (CT2013) to simulate atmospheric CO_2 concentrations in the Hudson Bay Lowlands. The primary objectives include: (1) Characterize daily, seasonal and interannual variations of atmospheric CO_2 for a 5-year (2008-2012) period; (2) Evaluate the performance of the STILT model, and CarbonTracker flux estimates. STILT-modelled CO_2 concentrations compare reasonably against observations. The mean model bias was -0.57 ppm at Churchill, and -2.44 ppm at Fraserdale. Smoothed seasonal curves fitted to the daily afternoon data revealed that model bias was highest during summertime, particularly over the Fraserdale region. Overall, the disparity between modelled and observed results are attributed to transport errors related to advection and PBL mixing.

DEDICATION

To my parents

ACKNOWLEDGEMENTS

Dr. Richard Bello, and Dr. Kaz Higuchi – For your motivation, supervision, and patience.

Yvonne Yim, and Dr. Raju Das – I appreciate you so much.

Dr. Tally Drezner, and Dr. Tarmo Remmel – For your statistical guidance.

Douglas Chan, Elton Chan, and Doug Worthy – For your expert advice and data contribution.

Derek Mallia, and Christopher Gerbig – For all your help with STILT setup and configuration.

Carol Weldon, and Dr. Robert McLaren – For all your support.

Alex Kent, Yikalo Araya, Alex Singh, and Diego Sotomayor – For making gradschool complete.

Pelin Asci, and Marzena Marosz-Wantuch – For your kindness and genuine encouragement.

Ryan Rimas, Kimisha Ghunowa, Tasnuva Rashid, and Jennifer Rup – For all the fun we had!

Ayo Olagesin, Victoria Owaseye, Jael Patrick, and Samuel Ayinde – Friends in High Places.

Elizabeth Grace Martindale, and Lubuya Wavounda – You inspired me.

The Michael-Taiwos, Baloguns, Awojides, and Kalejayes – There's nothing better than family.

My parents; Esther O. and Nosiru A. Balogun – You were always there, every step of the way.

HS; Allos Parakletos – my best friend and counsellor.

TABLE OF CONTENT

LIST OF FIGURES

LIST OF TABLES

1.0 INTRODUCTION

1.1 Long-Term Monitoring of Atmospheric Greenhouse Gases

In recent years, our understanding of the climate system has improved significantly. Several areas of research have focused on understanding and explaining the dynamic nature of atmospheric processes, oceans, and land surfaces, as well as their complex physical, chemical and biological interactions. There have been better and more observations, further advancement in climate modelling, and increased understanding of climate system feedbacks. Furthermore, there has been remarkable progress in interpreting and quantifying observed changes in global and regional climate. For example, new evidence abounds from observations of the climate system, paleoclimate archives, theoretical studies of climate processes, and simulations using climate models that the atmosphere and ocean have warmed, the amounts of snow and ice have diminished, and sea level has risen (IPCC, 2013). These alterations in the climate system are attributed to changes in atmospheric composition, particularly in the concentrations of carbon dioxide, methane, and nitrous oxide.

Accurate long-term monitoring of atmospheric mixing ratios of greenhouse gases is essential to better interpret past and present global carbon cycles. This will facilitate predictions of future atmospheric levels of these greenhouse gases for given scenarios of various sources and sinks. Carbon dioxide has been monitored for several decades by an increasing number of measurement stations around the world, with careful attention to the calibration and methodology of the measurements (Masarie and Tans, 1995). Initially, most of these measurements were made primarily in the marine boundary layer, remote locations and on mountain tops, but continental

areas were considerably underrepresented (Tans, 1991). While such measurements were useful for estimating CO_2 exchange on a global scale (Fan et al., 1998; Bousquet et al., 2000; Gurney et al., 2002), continental and regional scale assessment had very large uncertainties. Several studies suggested that a new network of sites over the continents were indispensable to improve estimates of regional atmosphere-biosphere CO_2 exchange (Tans et al., 1996; Gloor et al., 2000). Of great importance was the approach proposed by Tans (1991) to determine CO_2 mixing ratios representative of continental areas. These methods were designed to capture regionally representative atmospheric concentrations, with minimal interference from local sources and sinks (Tans et al., 1996). Subsequent studies demonstrated the relevance of continuous monitoring of CO_2 on tall continental towers (Bakwin et al., 1995; Bakwin et al., 1998). Some of the extensively studied sites include (Bakwin et al., 2004); the 447-m tall WLEF television transmitter tower in Northern Wisconsin, USA (45.95◦N, 90.27◦W, LEF), the Harvard Forest Environmental Measurement Site in Central Massachusetts, USA (42.52◦N, 72.18◦W, HVD), the 610-m tall tower located in eastern North Carolina (35.37°N, 77.39°W), the Old Black Spruce site of the BOREAS Northern Study Area near Thompson, Manitoba, Canada (55.88◦N, 98.48◦W, OBS), and the Hegyh´ats´al, Hungary, tower site (46.95◦N, 16.65◦E, HUN).

The Global Atmosphere Watch (GAW) programme of the World Meteorological Organization (WMO) has continued to play a crucial role in promoting systematic and reliable observations of the global atmosphere. Through its partnership with the Members of WMO and several contribution networks and collaborating organizations, the GAW programme helps coordinate the measurement, analysis and dissemination of reliable scientific data. This long-term information about the changing composition of the atmosphere helps to advance scientific research

geared towards the understanding of carbon interactions and exchange between the atmosphere, oceans and biosphere.

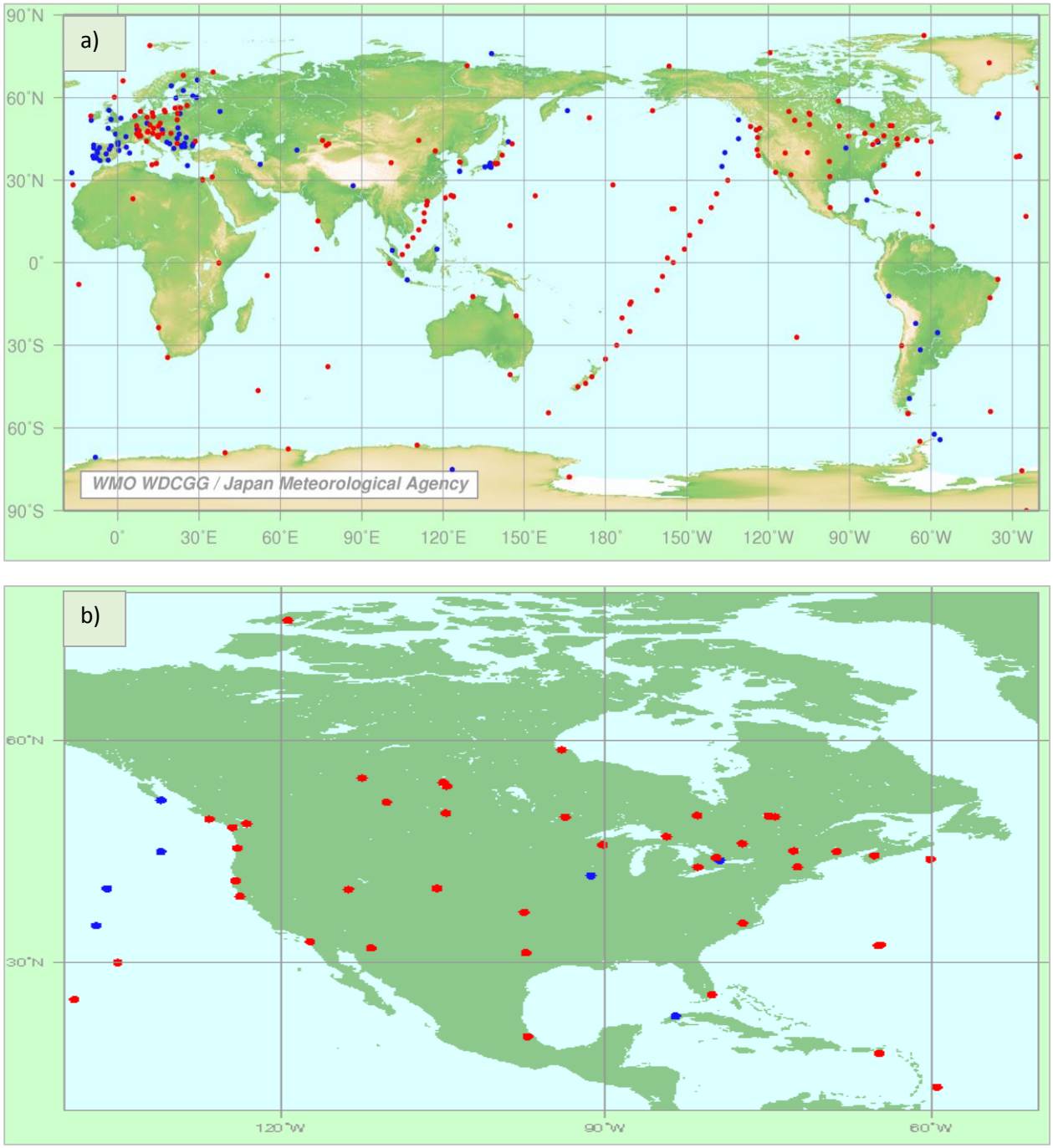

Figure 1.1. The distribution of the fixed stations that contribute data to the World Data Centre for Greenhouse Gases (WDCGG). The symbol " • " denotes that the data from the station has been updated in the last 365 days. (a) Global. (b) North America.

1.2 Atmospheric CO_2 Concentrations and Carbon Flux Studies

Annual accumulation of atmospheric CO_2 has varied significantly from year to year, ranging from about 1 GtC per year to as high as 6 GtC per year (Conway et al., 1994). This variation is mainly due to variations in the ocean and land fluxes, with the global carbon sink ranging from about 1 GtC per year to as much as 5 GtC per year (Keeling et al., 1995; Francey et al., 1995). To determine the spatial distribution of these carbon sources and sinks, a wide range of methods have been employed, each covering specific spatial scales; these include Eddy-covariance (EC) measurements (Baldocchi et al., 2001), and atmospheric inversions of measured CO_2 mixing ratios (Gloor et al., 2001; Gurney et al., 2002).

Direct measurements of terrestrial carbon flux using eddy covariance (EC) techniques have been widely used to interpret and predict the role of terrestrial ecosystems in the global carbon balance (Baldocchi et al., 2001). Currently, there are over 250 sites across the world where eddy covariance and other methods are being used to continuously assess carbon balance. (J. M. Chen et al., 2007). The EC approach provides information on a fine temporal and spatial scale (Law et al., 2002), however, these measurements are limited because the average footprint, or influence area of upwind surface flux does not typically exceed 1-3 km^2 (B. Chen et al., 2008). Therefore, much of our current understanding of the global carbon cycle is derived from long-term observations and analysis of atmospheric CO_2 mixing ratios. These studies employ atmospheric transport models to link observed mixing ratios to spatially resolved surface fluxes, thereby retrieving information on atmosphere-biosphere exchange. Global scale (~51 x 10^7 km^2) carbon balance estimates using data from global flask networks have been extensively interpreted and significantly improved through atmospheric inverse modelling (Keeling et al., 1989; Tans et al., 1990; Conway et al., 1994; Enting et al., 1995; Fan et al., 1998; Bousquet et al., 1999; Gurney et

al., 2002). This progress in carbon budget studies have been restricted to the extreme ends of the spatial-scale spectrum, either the global inverse modelling or the EC measurements. Complex terrain and landscape heterogeneity complicates extrapolation from eddy covariance measurements to the regional scale, and limited spatial coverage by the global observational networks restricts downscaling from global to the regional scale (Gurney et al., 2002; Helliker et al., 2004). Consequently, carbon estimates at the intermediate level—the regional scale (10^3 to 10^6 km^2)—is still an active area of research interest that requires further development. Reliable estimates of regional carbon fluxes are essential to improving our understanding of the carbon cycle, as well as predicting the feedback between climate change and the carbon cycle (Friedlingstein et al., 2003; Fung et al., 2005; Crevoisier et al., 2006).

Measurements of atmospheric CO_2 mixing ratios on continental towers have been very useful for inverse model studies at the regional scale (Wofsy and Harriss, 2002). Surface flux information retrieved from CO_2 concentration data measured at tall towers (>∼100 m) provide a powerful constraint on 'bottom-up' flux models. This is because such information contain an integrated signal of CO_2 exchange representing footprint areas of up to 10^5 km^2 (Gloor et al., 2001; Lin et al., 2004b), which are several orders of magnitude larger than the direct flux measurements using EC techniques. In addition, studies of the CO_2 balance of the ABL have greatly improved our understanding of regional carbon balance of the terrestrial surface (Helliker et al., 2004). Previously, several papers focused on describing the scalar rate of change in the ABL during its nonlinear daytime growth (De Bruin, 1983; McNaughton and Spriggs, 1986; Denmead et al., 1996; Raupach, 1995, 2000, 2001; Levy et al., 1999; Kuck et al., 2000; Lloyd et al., 2001; Styles et al., 2002) and the stable nocturnal accumulation (Pattey et al., 2002). This approach is limited to daytime estimates of surface fluxes and is impractical for long-term CO_2 balance estimates

(Fitzjarrald, 2002). Subsequently, other studies examined longer time period averages using continuous observations of atmospheric mixing ratios. Bakwin et al. (2004) examined CO_2 mixing ratios and atmosphere-surface exchange data from four temperate continental sites in the Northern Hemisphere. Their analysis focused on processes influencing the budget of CO_2 in the continental atmosphere on monthly and seasonal time scales. They employed a simple approach involving a parameterization of atmospheric transport by approximating advection as vertical exchange between the atmospheric boundary layer (ABL) and free troposphere (FT). The resulting estimates of surface exchange of CO_2 from CO_2 mixing ratio measurements are representative of a regional scale (i.e. ~10^6 km^2). Upon comparison with direct, local-scale eddy covariance measurements of net exchange with the ecosystems around the towers, the resulting fluxes were in reasonable agreement. Similarly, Helliker et al. (2004) applied a quasi-equilibrium approach for the terrestrial ABL to measurements of CO_2 and water vapor made within the ABL from a 396-m tall tower in Wisconsin. This concept is based on the argument that long-term (monthly) averages of continuous measurement of CO_2 mixing ratios in the ABL from tall towers show distinct differences from the background CO_2 in the Marine Boundary Layer (MBL) (Bakwin et al., 1998). The study demonstrated that these distinct differences of CO_2 reveal a balance between the surface fluxes and the exchange with the free troposphere. The resulting estimates of net CO_2 flux was in close agreement with eddy covariance measurements (Helliker et al., 2004).

However, the above studies attempted to interpret the signal of regional CO_2 exchange using tall tower concentration data by focusing on simple one-dimensional atmospheric boundary layer budgets that rely on gradients in CO_2 concentrations between the boundary layer and the free troposphere. These methods are restricted to monthly resolution by the need to smooth and average over several synoptic events. Moreover, the free tropospheric CO_2 mixing ratios above the towers

were represented by proxy measurements from the marine boundary layer, because of limited observations over the continents (Matross et al., 2006). This approach has been strongly criticized by Gerbig et al. (2003) and Lin et al. (2006), whose studies demonstrated that free tropospheric CO_2 concentrations differ significantly from the MBL reference over the continent, leading to biases in calculations of regional CO_2 flux. These differences result primarily from the time lag for vertical propagation of marine boundary layer concentration changes upwards from the surface into the free troposphere, as well as from meridional transport via meandering of the polar jet, and deep convective events (Gerbig et al., 2003a). Hence, there has been some remarkable progress in the development of more reliable methods that quantify and validate estimates of carbon balance at regional scale using atmospheric observations (Lin et al., 2006; Matross et al., 2006; J. M. Chen et al., 2007, B. Chen et al., 2008).

A 'receptor-oriented' analysis framework was introduced by Gerbig et al. (2003) which was designed to quantitatively interpret the atmospheric signatures of surface processes by linking concentrations at measurement locations (receptors) to surface fluxes in upwind regions. This modelling framework typically consists of three components: (1) an atmospheric transport model that quantitatively link spatially and temporally resolved upwind surface sources/sinks to concentration measurements at the measurement location; (2) an observation-based lateral boundary condition for CO_2, resolving vertical and meridional gradients; and (3) *a priori* CO_2 inventories and/or a model for surface fluxes (Gerbig et al., 2003b; Matross et al., 2006; Lin et al., 2006; Pathmathevan et al., 2006). Applications of this framework provides a basis to address the problems encountered when using data collected over the continent, including representation and aggregation error (Lin et al., 2006; Gerbig et al., 2003b; Kaminski et al., 2001), as well as the rectifier effect (Denning et al., 1996a,b).

Similarly, a number of approaches have been explored to extract the gross primary productivity (GPP) from atmospheric CO_2 concentration measurements. B. Chen et al. (2008) developed and compared two independent methods to extract the gross primary productivity (GPP) from atmospheric CO_2 concentration measurements. Employing an integrated ecosystem-boundary layer model for simulating ecosystem fluxes and atmospheric diffusion (B. Chen et al., 2004), the first method involves a PBL carbon budget approach that allows the estimation of regional GPP on a daily basis from the analysis of the hourly CO_2 concentration measured at several heights (30 m, 122 m, and 396 m) on the Wisconsin tall tower (B. Chen et al., 2006a, 2006b; J. M. Chen et al., 2007). The second method involves retrieving regional GPP by superimposing the daily concentration footprint on the underlying daily GPP field simulated using a spatially explicit ecosystem model driven by remote sensing inputs (B. Chen et al., 2008). The comparisons of these two independent regional GPP estimates, i.e., one is concentration-derived and the other is concentration footprint-integrated, have been conducted for a 28-m tower at an old black spruce site near White Swan Lake, Saskatchewan, Canada (B. Chen et al., 2008). Both methods agree well and the model used for GPP estimation within the footprint had good agreement with eddy covariance (EC) flux measurements, suggesting that these two methods are both useful for obtaining information on regional carbon flux (B. Chen et al., 2008).

1.3 Global Warming and the "Missing Carbon Sink"

Climate change is, perhaps, the most pressing environmental issue facing humans. The warming in the climate system is unequivocal and since the 1950s, many of the observed changes are unprecedented over decades to millennia (1PCC, 2013). Furthermore, there is clear evidence that the continued increase in the atmospheric burden of CO_2 is caused by anthropogenic emissions. However, what remains unclear is the understanding of the mechanisms and dynamics responsible for the removal of anthropogenic CO_2 from the atmosphere. Indeed, significant inter-annual changes in the global growth rate for CO_2 have often occurred (Keeling et al., 1989; Conway et al., 1994), and are attributed to both human activities and seasonal or year-to-year variations in biospheric fluxes (Keeling et al., 1976). To a large extent, the distribution, magnitude and prospects of anthropogenic CO_2 emissions are fairly well understood, but not so for the ocean and land fluxes. Our understanding of the response of global ecosystems to climate changes and anthropogenic perturbations is consequent upon accurate interpretation of the spatial distribution and magnitude of natural carbon sources and sinks. This will help explain the mechanisms for carbon sequestration and improve predictions of future trends in atmospheric CO_2 concentrations (Enting et al., 1995; Enting, 1999; Wofsy and Harris, 2002).

Several carbon cycle studies have concluded that a large net sink for CO_2 exists at temperate latitudes of the Northern Hemisphere to balance the global carbon cycle. Initially, it was uncertain whether the sink was predominantly oceanic (Keeling et al., 1989) or terrestrial (Tans et al., 1990). Further atmospheric measurements, stable isotope analysis, and inverse modelling from a globally distributed network of sampling stations have unanimously recognized the terrestrial biosphere of the northern mid-latitudes as the major component of this carbon sink (Tans et al., 1990; Denning, 1994; Ciais et al., 1995; Fan et al., 1998; Bousquet et al., 1999; Gurney et al.,

2002). However, uncertainties still abound and several other questions remain unsolved by the scientific community. For example: How is the northern carbon sink partitioned between Eurasia and North America (Fan et al., 1998; Bousquet et al., 1999)? What are the feedback-magnitude mechanisms between the natural carbon cycle of northern terrestrial ecosystems and the global climate system (Pacala et al., 2001; Caspersen et al., 2001; Field and Fung, 1999)? And how can we accurately estimate and predict the processes by which anthropogenic CO_2 is sequestered in nature (Heimann and Reichstein, 2008)?

The current capacity of North American ecosystems to absorb about 0.4 ± 1.3 PgC yr^{-1} (1 Petagram Carbon equals 10^{15} gC, or 1 billion metric ton C, or 3.67 billion metric ton CO_2) is not guaranteed to rise along with human emissions or to even remain stable at its present levels. The North American natural sink offsets about 20% of the emissions from the burning of fossil fuels in the U.S.A., Canada and Mexico combined (1.8 PgC yr^{-1}). Primarily, about 32% of this estimated sink is located in the deciduous forests along the East Coast, and 22% in the boreal coniferous forests (Peters et al., 2007). However, there are significant year-to-year variability in this terrestrial carbon budget depending on climate variations that alter regional temperatures, moisture conditions, and consequently, growing season length (Pacala et al., 2001; Zeng et al., 2005; J.M. Chen et al., 2006). For instance, widespread droughts in the U.S. west and Canada in 2002 resulted in land ecosystems being approximately neutral—neither a source nor a sink of CO_2. In contrast, 2011 and 2012 were the periods with the largest net annual input of CO_2 to the atmosphere from North America even though fossil emissions remained generally steady (1.7 and 1.9 PgC yr^{-1}) over this period. Consequently, North American terrestrial ecosystems may have been a net source of CO_2 to the atmosphere in 2011 and 2012 (Peters et al., 2007).

Furthermore, there is high uncertainties in the response of boreal forests to projected changes in climate, though evidence from field observations and biogeochemical modelling make it scientifically conceivable that boreal forest regions could tip into a different vegetation state under global warming (Lenton et al., 2008; Allen et al., 2010; IPCC, 2013). Some studies (Black et al., 2000) found that warming increased carbon uptake more than release in a boreal forest, while others (Goulden et al., 1998) showed the opposite. Indeed, the effect of temperature on the forest carbon cycle is highly variable depending on species, age and stand history (J. M. Chen et al., 2003).

1.4 Carbon in Canada's Boreal Forest and the Hudson Bay Lowlands

About 28% (552 million hectares) of the world's boreal zone lie within Canada's borders (Brandt et al., 2013). It extends from the Alaska border and northern British Columbia in the west to Newfoundland and Labrador in the east, within which some 3.09×10^6 km^2 are covered by forests and other wooded land (Price et al., 2013). This zone is bordered to the north by treeless arctic tundra and to the south by temperate forest or grassland. In addition, much of Canada's boreal zone features thousands of lakes, rivers and wetlands, with substantial areas underlain by permafrost (Price et al., 2013). Undoubtedly, the Canadian boreal zone plays a vital role in the global carbon cycle (Kurz et al. 2013; Lemprière et al. 2013). Since 1990, Canada's managed boreal forest has acted as C sink of 28 Tg C $year^{-1}$, removing CO_2 from the atmosphere to replace the 17 Tg of C annually harvested and store an additional 11 Tg of C $year^{-1}$ in ecosystem C pools (Kurz et al., 2013). Carbon uptake from net primary production and carbon release during heterotrophic respiration are the two main fluxes that determine the net carbon balance in this zone.

In some years or in certain areas, carbon release can be high due to large human or natural disturbances (Kurz et al., 2013). Uncertainties about the present and future carbon balance of Canada's boreal forest are high, as well as their response to global climate change. It is clear, however, that due to the decreasing sea ice, shorter periods of winter snow cover, and the associated arctic amplification, northern circumpolar boreal forests and tundra will continue to experience greater exposure to warming than other terrestrial biomes (Chapin et al. 2005; Foley 2005; Meehl et al. 2007; Trenberth et al. 2007).

The Hudson Bay Lowlands (HBL) region of Canada is an ecologically significant and widely studied boreal wetland region (Riley, 1982; Mortsch, 1990; Glooschenko et al., 1994). It is the second largest semi-continuous wetland region in the world (320, 000 km^2) accounting for an estimated 12% of the Earth's total wetlands (Glooschenko et al., 1994; Wang et al., 2008). The HBL region features a succession of wetland types including coastal marshes, fen and bog peatlands. Furthermore, the HBL climate is significantly influenced by the moderating effects of the Hudson Bay. It's anomalously cold temperatures in comparison with other regions at similar latitudes reflect the presence of ice cover over the Hudson Bay, which undergoes a complete cryogenic cycle each year. (Rouse, 1991). Similarly, the presence of permafrost in the region, which is the southernmost extent of permafrost in North America, is attributed to the Hudson Bay (Gough and Leung, 2002). Consequently, the importance of the Hudson Bay Lowlands, both in global climate modelling and carbon studies, cannot be overemphasized (Gagnon and Gough, 2005a; McLaughlin and Webster, 2014).

Two long-term continental tower sites are strategically located within the Hudson Bay Lowlands to provide regional scale information on greenhouse gas emissions and sinks. The Fraserdale tower site is located on the southern edge of the HBL and on the northern perimeter of

the boreal forest at 49°52'N, 81°37'W. The Churchill tower site is located at the northern edge of the HBL (58°45′N, 94°04′W) and on an ecotone between the Arctic tundra to the northwest and the boreal forest to the south. Numerous research studies have been conducted using atmospheric CO_2 data from the Fraserdale site (Higuchi et al., 2003; Chan et al., 2004; B. Chen et al., 2005; J. M. Chen et al., 2006; B. Chen et al., 2006a, 2006b).

The diurnal, seasonal and inter-annual variations in atmospheric CO_2 at the Fraserdale 40-m tall tower site have been well described and analyzed (Higuchi et al., 2003). These variations are attributed to the complex and dynamic interactions between the biospheric carbon fluxes and the daily evolution of the planetary boundary layer, particularly during the growing season. Averaged over the 7-yr period from 1990 to 1996, Higuchi et al. (2003) observed diurnal variations in atmospheric CO_2 on the order of 50 ppm or more. This observed diurnal CO_2 amplitude is attributed to changes in radiative fluxes which results in night-time CO_2 accumulation in a stable nocturnal boundary layer. Furthermore, the day-to-day variations in the CO_2 mixing ratios is determined mainly by the daily changes in the PBL dynamics associated with different synoptic weather systems or events. Climatologically, the seasonal minimum occurs in early August at Fraserdale, and the amplitude of the annual cycle is about 20 ppm, revealing the stronger influence of a seasonal vegetative cycle than those observed at background stations at similar or higher latitudes (Higuchi et al., 2003).

Using a 13-year (1990–1996, 1999–2004) hourly record, J. M. Chen et al. (2006) retrieved carbon cycle information from atmospheric CO_2 concentration measurements at the Fraserdale tower site. Based on their results, the retrieved Gross primary productivity (GPP) and ecosystem respiration (ER) values suggest that boreal ecosystems in the region around the Fraserdale tower were collectively a carbon sink of 10.8 ± 14.2 g C m^{-2} y^{-1} in the study period. In addition, the study

demonstrated an interesting temperature-dependent ecosystem signal; the results showed that in warmer years the planetary boundary layer was more depleted with CO_2, and that boreal ecosystem photosynthesis increased more than ecosystem respiration in those years (J. M. Chen et al., 2006).

1.5 Research Objectives

It is important to note that while several studies have focused on the Fraserdale site, only a few have been carried out at the Churchill tower site. In fact, to the best of my knowledge, there is no existing research work that uses the atmospheric CO_2 measurement data at the Churchill tower site to retrieve carbon cycle information in the region. Therefore, in this research work, atmospheric CO_2 data from the 60 m Churchill tower (58.75ºN, 94.07ºW) in northern Manitoba (Canada) are analyzed. The CO_2 data from the 40 m tower in Fraserdale, Ontario are used for spatial comparison.

First, the seasonal and inter-annual variations of atmospheric CO_2 mixing ratios for a 5-year (2008-2012) weekly flask measurement record are described. In addition, the diurnal and daily (day-to-day) patterns are explored using continuous (hourly) atmospheric CO_2 data for the year 2012. The overall aim is to characterize daily, seasonal and interannual variations of CO_2 in the region, and to quantify the relative influence of vegetation on atmospheric CO_2 mixing ratios at Churchill and Fraserdale. The study aims to derive carbon cycle information from atmospheric CO_2 measurements, and consequently, demonstrate the influence of local–regional biospheric emissions and sinks on the carbon balance of the Hudson Bay Lowlands (HBL). Indeed, the concentration footprints of tower observations are several orders of magnitude larger than the conventional direct flux measurements using eddy covariance (EC) techniques. Therefore, by

retrieving an integrated signal of CO_2 exchange representing footprint areas of 10^3–10^4 km^2 (Lin et al., 2003), this study will help improve our understanding of carbon balance in the coastal HBL.

Second, a Lagrangian Particle Dispersion Model (LPDM) framework is employed to simulate atmospheric CO_2 concentration at the Churchill and Fraserdale tower sites. Model results are compared with CarbonTracker measurements, as well as tower observations. Differences between all three results are assessed with respect to some notable characteristics of the CO_2 seasonal cycle; (i) timing of the seasonal minimum; (ii) magnitude of the seasonal minimum, and (iii) seasonal amplitude. Here, the main objectives are to assess the accuracy of the STILT model, and examine various sources of model errors. This study seeks to address questions such as: What factors might be responsible for biases in simulated CO_2 concentrations? How would uncertainties in *a priori* surface flux fields influence model results? Do the model biases vary significantly between Churchill and Fraserdale? And what is the seasonal pattern of these biases?

Finally, the influence of the Hudson Bay on STILT model performance is briefly explored. It is anticipated that environmental conditions such as wind speeds and direction would have noticeable impact on simulated atmospheric CO_2 concentrations. This is because, atmospheric CO_2 concentrations are modified not only by surface sources and sinks, but also by horizontal advection and vertical mixing, on the way to the measurement tower. This study seeks to determine how model transport errors may be exacerbated by the advective influence of the Hudson Bay.

2.0 THEORETICAL BACKGROUND

2.1 Atmospheric Concentration of Chemical Species

The structure, composition and dynamics of the Earth's atmosphere are some of its most defining attributes when compared to other planets in the solar system. This unique atmosphere drives the weather systems, blocks (some of) the sun's potentially harmful radiation, provides free oxygen, and indeed, sustains all life forms on Earth. Most of the atmosphere is made up of Nitrogen (78%) and oxygen (21%), and the remaining 1% of the atmospheric gases are referred to as trace gases. Interestingly, some of these so-called trace gases, despite their relative shortage, play a very crucial role in the Earth's radiative balance. Greenhouse gases such as water vapor, carbon dioxide, methane, nitrous oxide, and ozone help regulate the Earth's temperature by trapping outgoing thermal infrared radiation, thereby maintaining an average surface temperature of about 15 ^{o}C. The net result is an upward transfer of infrared radiation from warmer levels near the earth's surface to colder levels at higher altitudes. Without this so-called greenhouse effect, Earth's surface would be 30 degrees Celsius cooler, perhaps making it too cold for life to thrive.

However, since the mid-18th century, the atmospheric concentrations of CO_2, CH_4, and N_2O have increased substantially. In 2011 the concentrations of these greenhouse gases were 391 ppm, 1803 ppb, and 324 ppb, exceeding the pre-industrial levels by about 40%, 150%, and 20%, respectively (IPCC, 2013). The rising concentrations of these heat-trapping gases result in higher opacity of the atmosphere, increased absorption of infrared radiation, and consequently, warmer surface air temperatures. This outcome is called the enhanced greenhouse effect, and is characterized by complex climate system responses and feedbacks.

The central objective of atmospheric chemistry has long been to understand the factors controlling the concentrations of chemical species in the atmosphere. Generally, there are four main processes that determine the atmospheric composition of any given trace gas; emissions (sources), chemistry, transport, and deposition (sinks). With rising atmospheric abundances of greenhouse gases being linked to the imbalance between their sources and sinks, as well as distribution by transport processes, there is a more urgent need to apply simple principles of physics and chemistry to describe a complex system such as the atmosphere.

2.2 Atmospheric Transport and the Planetary Boundary Layer

The troposphere is the lowest layer of the earth's atmosphere, extending from the surface upward to about 8-17 km. It is the most important portion of the atmosphere accounting for about 80% of the total mass. The troposphere also contains the bulk of atmospheric water vapor, the majority of clouds and almost all weather activities. Furthermore, transport processes and their associated transfer of heat, mass, and momentum modify the attributes of the lowest few kilometers of the atmosphere. This lowest part of the troposphere that typically responds to temporal and spatial changes in surface properties is called the planetary (atmospheric) boundary layer (PBL). The height of the PBL is about 1-3 km, ranging from its maximum over deserts and boreal forests, to a minimum over wetland regions. It is turbulent, well-mixed, and is characterized by the emission, transport and dispersion of trace gases and air pollutants. Therefore, the PBL is of great significance in atmospheric chemistry, and dispersion modelling.

When trace gases or pollution plumes are emitted into the PBL, they are subjected to both horizontal dispersion by the mean wind and vertical dispersion by turbulent eddies. Heating and

friction at the Earth's surface creates atmospheric turbulence in the PBL which move trace gases such as CO_2 and CH_4 toward (deposition/sink) or away (emission/source) from the surface. Eddy motions generated by friction related to the roughness of the ground or irregular topography are commonly called mechanical turbulence. The frictional drag of the surface causes rapid fluctuations in wind speed and direction, and influences the transport and dispersion of atmospheric trace gases and pollutants. Moreover, surface heating causes atmospheric instability which generates convective turbulence that extends to even greater altitudes in the atmosphere. The strength of this so-called thermal turbulence depends on the intensity of surface heating, which in turn is determined by the time of day or season. During daytime (in summer), intense solar heating increases surface air temperature resulting in atmospheric instability and the development of the convective boundary layer (CBL). Buoyancy in this unstable atmosphere accelerates both upward and downward movements of air promoting strong vertical mixing of atmospheric constituents (such CO_2 and CH_4). At nighttime, the Earth's surface cools rapidly and stable conditions develop near the surface. Particularly during calm conditions, the nocturnal boundary layer (NBL) is typically shallow, rarely exceeding 300 m. Thus, the stable stratification in the NBL suppresses turbulence and vertical mixing, resulting in accumulation of pollutants or increased concentration of greenhouse gases near the ground. Above the NBL, remnants of the daytime CBL form a residual layer, which remains well-mixed, but disconnected from the surface. Consequently, there is strong vertical gradients in atmospheric mixing ratios of trace gases during calm winter nights, for example. It is therefore evident that accurate diagnosis of emissions and sinks of greenhouse gases from atmospheric concentration requires a realistic representation of PBL dynamics. In order to accomplish this enormous task, the capacity to model atmospheric (turbulent) flow is crucial.

2.3 Lagrangian Modelling of the Atmosphere

Atmospheric transport models are employed in an attempt to provide a quantitative understanding of physical and chemical processes in the atmosphere. This approach offers realistic approximations necessary to adapt the real, complex atmosphere into a model system. There are two basic types of model references used in atmospheric science; Eulerian and Lagrangian (Byers, 1974; Dutton, 1986). Characteristically, the Eulerian perspective describes the composition and dynamics of the atmosphere within fixed domains in space, while the Lagrangian perspective follows an air parcel as it moves with the flow, describing its trajectory as well as observed changes in its composition. The Lagrangian reference frame can be expressed as:

$$\frac{\mathrm{D}\psi}{\mathrm{D}t} = S, \tag{a}$$

Where ψ is any state variable associated with the air parcel (i.e., trace gas concentration, temperature or moisture), and S is a generic source term. Therefore, equation (a) represents the rate of change of a specified air parcel variable as it moves with the flow. Similarly, using the definition:

$$\frac{\mathrm{D}\mathbf{x}}{\mathrm{D}t} = u, \tag{b}$$

x denotes the location of the air parcel, and $\boldsymbol{u}$ is the velocity. Since the equation represents the rate of change of the air parcel's position, integrating the velocity $\boldsymbol{u}$ over various time steps will mark out its trajectory. The resulting simplest first-order ("zero acceleration") solution is given as (Stohl, 1998a):

$$\mathbf{x}(t_0 + \Delta t) = x(t_0) + \mathbf{u}(t_0) \cdot \Delta t + \ldots, \quad \text{(c)}$$

In order words, equations (a), (b), and (c) show that Lagrangian modelling can be employed to track greenhouse gases by determining the trajectory of the air parcels, x(t), and the trace gas concentrations (where $\psi = C$) at the different locations $\mathbf{x}$ and times t. Accordingly, Lagrangian modelling are also referred to as "trajectory modelling".

With advances in computer modelling in the early 1990s, trajectory models were used to study a wide variety of atmospheric phenomena, for example: in synoptic meteorology, to investigate airmass flow around mountains (Steinacker, 1984); in climatology, to identify pathways of water vapor transport (D'Abreton and Tyson, 1996); and in environmental science, to establish source-receptor relationships of air pollutants (Stohl, 1996a). Today, these Lagrangian models have grown in popularity and relevance, with over a hundred scientific papers currently published every year (Lin, 2012). Such studies utilize diverse types of Lagrangian models which can be broadly categorized into four approaches based on their representations of air parcels.

Mean trajectory models assume that air parcels retain their individual identities, and a single line is adequate to describe each parcel's motion (Lin, 2012). This assumption is however, problematic because the boundaries of an air parcel are not well-defined (Bohren and Albrecht, 1998). Typically, a parcel of air is unable to preserve its identity due to molecular and turbulent diffusion. As a result, mean trajectory models track the path of air parcels by focusing only on the mean velocity component $\bar{\mathbf{u}}$, but neglect the turbulent, stochastic component $\mathbf{u}'$ in the Reynolds decomposition of $\mathbf{u}$ (Reynolds, 1895):

$$\mathbf{u} = \bar{\mathbf{u}} + \mathbf{u}'. \quad \text{(d)}$$

For dimensionless Reynolds number (Re) greater than a critical value of ~5000, smooth laminar motion undergoes a transition to turbulent motion, which is inherently unstable. Since this critical Reynolds number is almost always exceeded within the troposphere, atmospheric motion is inevitably turbulent in nature (Salby, 2012). Therefore, mean trajectory models poorly represent average transport within the planetary boundary layer (PBL), where turbulence is strong, but may be valid in the stratosphere or in laminar flow regimes (Stohl and Wotawa, 1993).

In an attempt to solve the identity preservation problem, Lagrangian box models represent several air parcels as an aggregate. A variant of this approach is the column model which follows the chemical evolution of a well-mixed column of air travelling along the surface and extending vertically to some specified mixing depth, typically the top of the PBL (Eliassen et al., 1982; Jacob, 1999). Examples of the Lagrangian box models which have been applied to simulate atmospheric chemistry include, the single trajectory-based ELMO-2 model (Strong et al., 2010) and the multiple trajectory-based CiTTyCAT model (Pugh et al., 2012). This modelling approach still has large uncertainties due to distortion of the box by intense turbulent mixing and strong wind shear (Seaman, 2000).

Gaussian puff models provide a more accurate trajectory information by accounting for the effects of turbulent dispersion. Here, air parcels are represented as fluid elements (or "puffs") that continue to grow in size. Following G. I. Taylor's classical work (Taylor, 1921) which describes plume dispersion in stationary homogeneous turbulence, the puffs normally adopt Gaussian distributions in all three dimensions. Gaussian puff models such as CALPUFF have been used for a wide variety of pollution dispersion and air quality assessment studies (Scire et al., 2000; Walcek, 2002). However, such models are unable to satisfactorily resolve the complex interaction between

turbulence and wind shear in the PBL, and thus, require supplementary parameterizations such as puff splitting (Walcek, 2002).

Particle models simulate $\mathbf{u}'$ by representing air parcels as particles of equal mass that are transported with random velocities generated by a Markov process (Thomson and Wilson, 2012). Thus, an ensemble of particles, each undergoing random impacts in the field of eddies and following diverse dispersion paths, is simulated to capture the stochastic effects of turbulence. These Lagrangian particle dispersion models (LPDMs) are the most accurate and sophisticated of the Lagrangian models, tracking thousands to hundreds of thousands of particles in three dimensions, in order to provide a well-representative characterization of the plume's trajectory. This modelling approach is often referred to as one- or single-particle modelling, since it treats the motion of each particle as completely independent of that of other particles by employing a set of stochastic differential equations for velocity and position increments. Examples of the most commonly used LPDMs include HYPACT (Walko et al., 2001), STILT (Lin et al., 2003), FLEXPART (Stohl et al., 2005), and NAME (Jones et al., 2007).

2.4 Backward-Time Lagrangian Particle Dispersion Models

Since Taylor's (1921) landmark paper on Lagrangian analysis of the continuous movements of particles in stationary homogeneous turbulence, there has been significant improvements in Lagrangian stochastic modelling (Sawford, 1985; Thomson, 1987; Wilson and Sawford, 1996; Rodean, 1996; Thomson and Wilson, 2012). In particular, backward-time LPDMs

have been developed to derive the trajectories of air parcels by using a time-reversed method. This is achieved by integrating equation (c) backward in time:

$$\mathbf{x}(t_0 - \Delta t) = x(t_0) - \mathbf{u}(t_0) \cdot \Delta t + \ldots, \quad \text{(e)}$$

Lagrangian modelling involving time-reversed simulations, which are also referred to as "receptor-oriented" (Gerbig et al., 2003b) have been increasingly applied to a wide variety of scientific endeavors. Such studies benefit from the computational efficiency of the backward-time method compared to their forward-time counterparts, especially when the number of upwind elements (e.g. sources and sinks) far exceed the number of receptors (e.g. measurement tower site). The approach presents different information including "footprints" (Lin et al., 2003), "retroplumes" (Stohl et al., 2003) and "touchdown velocities" (Flesch et al., 1995; Wilson et al., 2012).

Backward-time LPDMs have been particularly useful in inverse studies for diagnosing emissions of trace gases from atmospheric concentrations. These LPDMs have been applied at local, regional, and global scales to retrieve information about surface fluxes of greenhouse gases (GHGs) from anthropogenic sources and natural systems. This is possible because the LPDMs running backward in time have the capability to compute and map out the sensitivity (i.e. "footprint") of observed GHG mixing ratios at a particular measurement location (i.e. the "receptor") to upwind source–sink locations (Lin et al., 2003; Seibert and Frank, 2004). The resulting surface–atmosphere exchange fluxes serve as regional or continental constraints in inverse model calculations (Gerbig et al., 2003b; Lin et al., 2004b; Kort et al., 2008; Stohl et al., 2009; Kort et al., 2010; Gourdji et al., 2013; Miller et al., 2014).

Introducing a "receptor-oriented" atmospheric modelling (ROAM) framework, Gerbig et al. (2003) constrained regional-scale terrestrial carbon fluxes with atmospheric observations over

the North American continent. This ROAM analysis framework includes a transport model, parameterizations for biosphere and fossil fuel fluxes, and a statistical model to create the lateral boundary conditions. ROAM was applied to observations collected during the CO_2 Budget and Rectification Airborne (COBRA) study in the year 2000, allowing quantitative comparison between the top-down constraint on fluxes from airborne observations of CO_2 with the bottom-up constraint of measurements from eddy covariance in a Bayesian synthesis inversion. They calculated vegetation signals along the COBRA flight track as the difference between measured CO_2 and the sum of advected boundary mixing ratios and fossil fuel combustion signal. The measurement-derived vegetation signals were then used to constrain large-scale biosphere-atmosphere exchange fluxes from upscaling of AmeriFlux measurements. Estimates of net fluxes at continental scale were obtained from the optimized biosphere model, constrained to be consistent with the COBRA observations and with the AmeriFlux data (Gerbig et al., 2003b).

Emissions of two non-CO_2 greenhouse gases over large areas of the U.S. and southern Canada were constrained using a backward-time Lagrangian particle dispersion model, and airborne measurements of methane and nitrous oxide (Kort et al., 2008). The atmospheric measurements were obtained from the CO_2 Boundary Layer Regional Airborne–North America (COBRA-NA) campaign in May and June, 2003. Air parcel trajectories as well as concentration footprints were calculated using the Stochastic Time-Inverted Lagrangian Transport (STILT) model, driven with meteorological fields from the Weather Research and Forecasting (WRF) model. To compute the associated surface flux contributions to the mixing ratios at the receptor, the footprints were multiplied by *a priori* emission fields from 'JK' wetland inventory (Bergamaschi et al., 2007), the EDGAR 32FT2000 inventory (Olivier et al., 2005), and the GEIA (Bouwman et al., 1995). The mixing ratio enhancements due to surface fluxes was then added to

a background concentration advected from the domain boundary. Results suggest the EDGAR inventory for CH_4 accurately accounts for emissions over much of the U.S. and southern Canada (accurate to 8 ± 14%), while both EDGAR and GEIA underestimated (by factors of 2.62 ± 0.50 and 3.05 ± 0.61, respectively) N_2O emissions (Kort et al., 2008).

Keller et al. (2012) derived European emissions of nine representative halogenated greenhouse gases (CFC-11, CFC-12, Halon 1211, HCFC-141b, HCFC-142b, HCFC-22, HFC-125, HFC-134a, HFC-152a) for the year 2009. The spatial coverage of the emission estimates were significantly increased by combining campaign measurements from Hungary with long-term atmospheric observations in Switzerland, Italy, and Ireland. Backward simulations with the Lagrangian particle dispersion model FLEXPART were used to obtain the source-receptor relationship (Stohl et al., 1998b, 2005). The FLEXPART model, driven by 3 hourly wind fields of the European Centre for Medium-Range Weather Forecasts (ECMWF) calculates the trajectories of tracer particles using the mean winds interpolated from the analysis fields plus random motions representing turbulence (Stohl and Thomson, 1999). A Bayesian inversion method that builds on least-squares optimization was employed to link atmospheric observations with model calculations. The results provided estimates of the spatial emission pattern over the area influencing the four measurement sites. Overall, the aggregated halocarbon emissions over the study area are estimated at 125 (106–150) Tg of CO_2 equiv/y, of which the hydrofluorocarbons (HFCs) account for the largest proportion with an average contribution of 41% (Keller et al., 2012).

It is clear from the above study examples that backward-time Lagrangian particle dispersion models have played a significant role in regional-scale surface flux estimations of various greenhouse gases. Certainly, the importance of these time-reversed LPDM simulations to inverse modelling frameworks cannot be overemphasized. The availability of trajectory

information which incorporates atmospheric phenomena such as mixing (Konopka et al., 2012), transport barriers (Sulman et al., 2012), turbulent eddies (Thomson and Wilson, 2012), and convection (Haertel, 2012), is one of the prime advantages of Lagrangian modelling. Additionally, LPDMs can provide subgrid-scale information, thereby resolving the finer-scale heterogeneity absent in Eulerian models (Lin et al., 2003). They also have the capability to capture the physics of turbulent transport in the "near-field" regime close to the sources, where turbulence is nondiffusive (Lin et al., 2012).

However, some uncertainties are inherent in transport model simulations. The dominant errors in trajectory calculations typically come from errors in the wind fields themselves (type 1 errors) or from type 2 errors due to the limited spatial and temporal resolution of the gridded wind fields (Stohl et al., 2001; Lin and Gerbig, 2005; Bowman et al., 2013). Other severe problems arise from vertical transport errors through convective transport in clouds and mixing within the planetary boundary layer (Gerbig et al., 2008; Kretschmer et al., 2012). It has been demonstrated that equally increasing both the spatial and temporal resolutions of the wind fields improve trajectory accuracy, compared to marginal improvements from solely higher spatial resolutions (Stohl, 1998a; Pisso et al., 2010; Bowman et al., 2013). Furthermore, LPDMs benefit appreciably from the use of time-averaged convective mass fluxes and time-averaged velocities instead of instantaneous winds. This has been shown in a number of diagnostic studies including Nehrkorn et al. (2010), Brioude et al. (2012), and Hegarty et al. (2013).

3.0 METHODOLOGY

3.1 Study Region

In Canada, long-term observations network for atmospheric measurements of CO_2, CH_4, CO, N_2O, H_2 and SF_6 provide the necessary data to identify seasonal variability and spatial distribution of greenhouse gases. Environment Canada's Greenhouse Gas Measurement Program began in 1975 and constitutes Canada's contribution to the World Meteorological Organization's (WMO) Global Atmosphere Watch Program. The measurement stations are carefully located across the country to collect local and regional scale information on greenhouse gas emissions from both natural (forests, wetlands) and non-natural (coal, oil and gas, agriculture, waste) sources. Currently, there are over 16 measurement sites, including the Churchill and Fraserdale tower sites.

3.1.1 Churchill, Manitoba

Churchill, Manitoba (58°45′N, 94°04′W) is a small port city located at the northern perimeter of the Hudson Bay Lowlands (HBL), and on an ecotone between the Arctic tundra to the northwest and the boreal forest to the south. Overall, the HBL is poorly drained, flat and dominated by extensive wetlands. Most of the region lies in northern Ontario but it also reaches into Manitoba and, to a lesser extent, Quebec. In particular, the Churchill area lies within the Coastal Hudson Bay Lowland ecoregion, along the western coast of Hudson Bay. This ecoregion is marked by short cool summers and very cold winters, with a mean annual temperature of about

-4 °C (ranging from 10.5 °C in summer and -19 °C in winter. Precipitation is between 400 mm in the northwest and 600 mm in the east.

Furthermore, the Coastal Hudson Bay Lowland region is part of the broad area of tundra and boreal forest transition where the latitudinal limit of tree growth is reached. The vegetation features very open stands of stunted white spruce and tamarack with secondary quantities of black spruce. In addition, a shrub layer of dwarf birch, willow or ericaceous shrubs, and a ground cover of sedge or lichen and moss is predominant (ESWG, 1995).

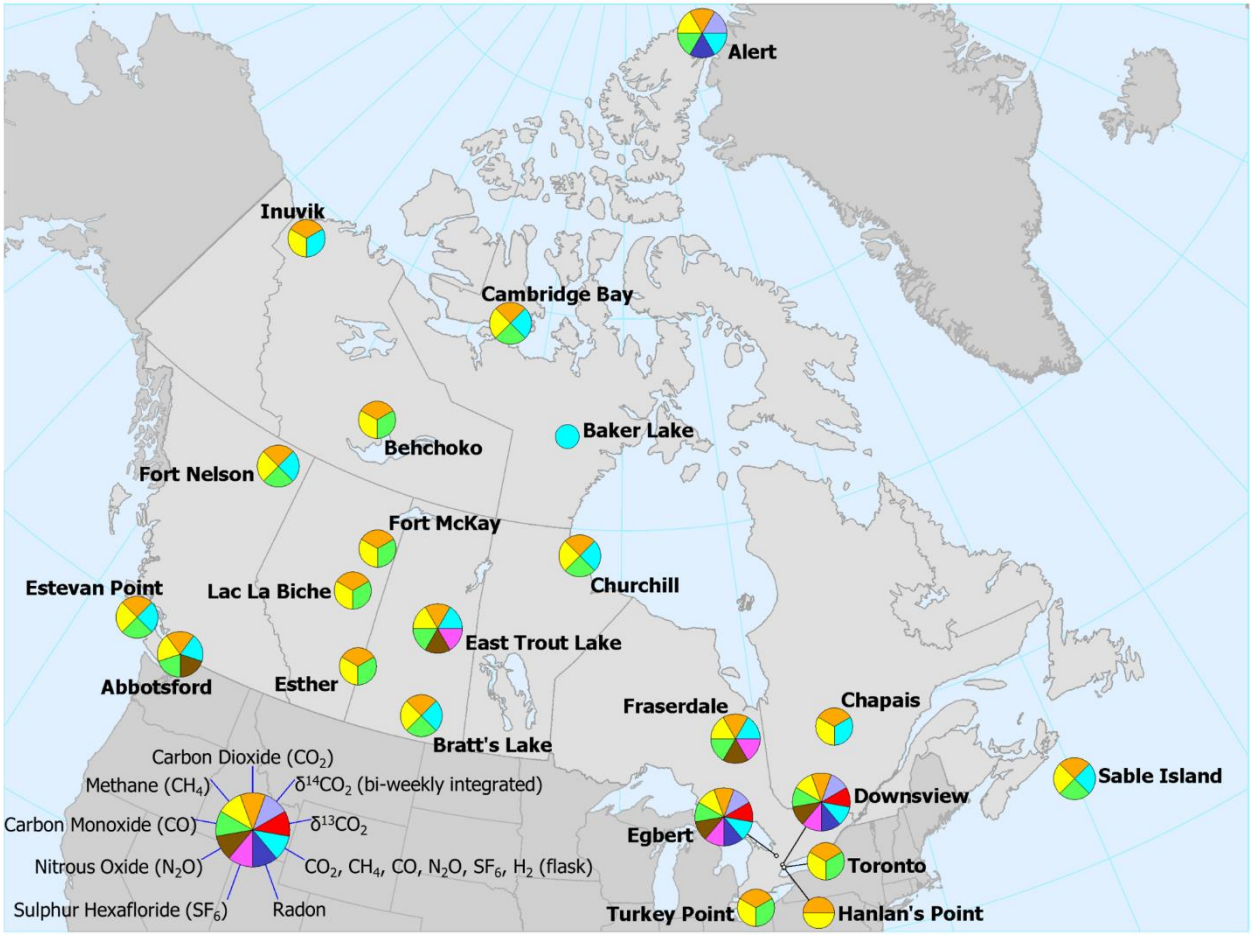

Figure 3. 1. Environment Canada Greenhouse gas measurement network. The stations are strategically located to provide regional scale information on greenhouse gas emissions from local and regional natural (forests, wetlands) and non-natural (coal, oil and gas, agriculture, waste) sources. (Source: Elton Chan, Environment Canada Climate Research Division).

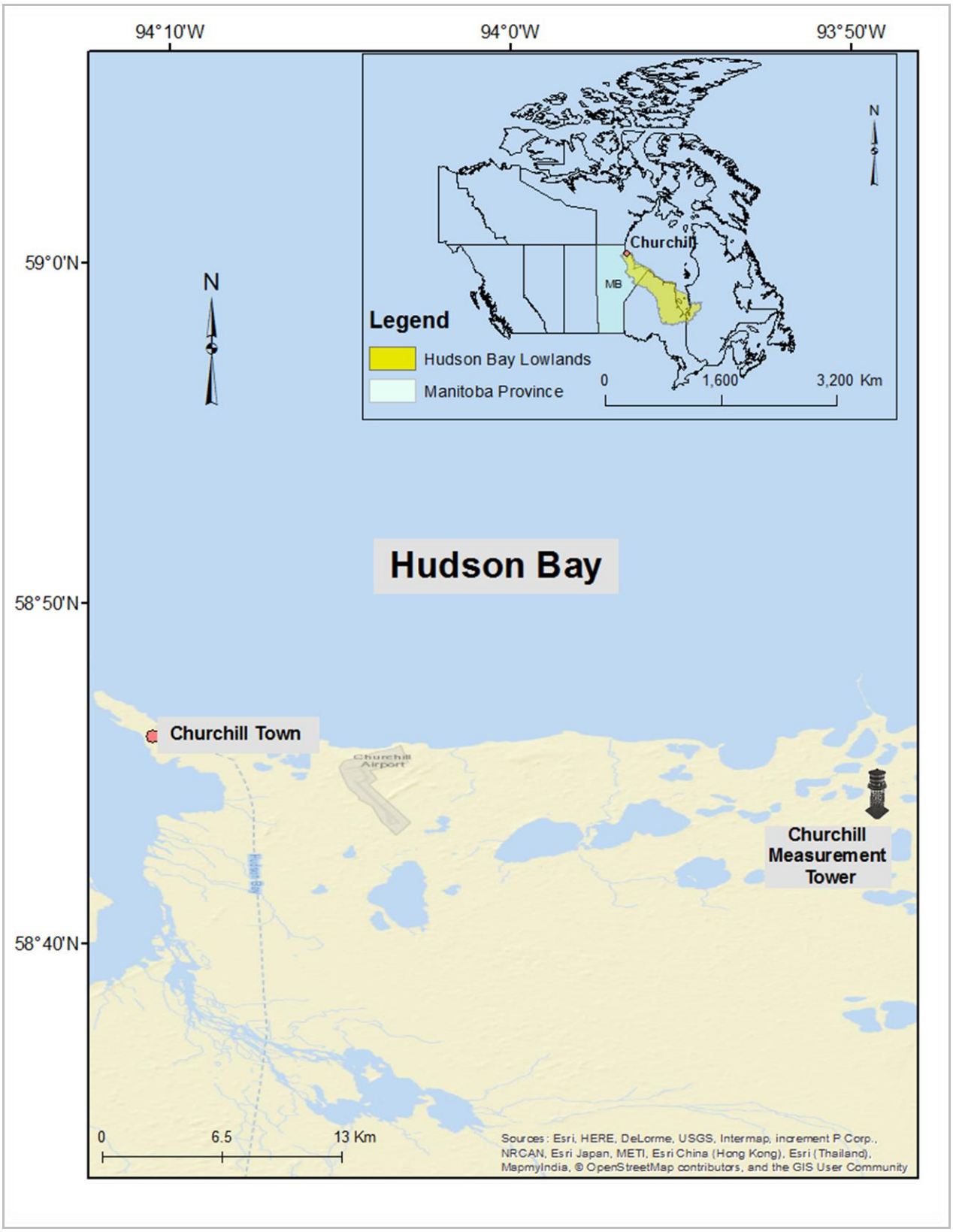

Figure 3. 2. Map of study area showing Churchill, Manitoba.

Up to about 8000 years ago, the region was covered by the Laurentide Ice Sheet, a massive sheet of ice that repeatedly covered most of northern North America, particularly Canada, during the Quaternary glacial epochs. After deglaciation, the region was inundated by the Tyrrell Sea and covered by marine sediments, raising water levels to as high as 150 m above the present coast and extending about 100 km inland (Dredge, 1992; Johnson, 1987). Subsequently, the continent began to recover from the huge weight of the ice sheet resulting in continued uplifting of the land surface, the so-called "isostatic rebound". The initial uplift was quite immediate and relatively rapid due to the elastic response of the earth crust to glacial unloading. The following uplift phase proceeded slowly, and continued to decrease exponentially. Today, the typical uplift rates are of the order of 1 cm per year (Johnson, 1987).

Overall, the post-glacial rebound process has contributed to the formation of a wide variety of new coastal habitats. Here, the wetland dominated landscape features fens, bogs, marshes, as well as shallow ponds and lakes which are about 0.25 to 2 m deep (Holland 1992; Roulet et al., 1994). Along the Hudson Bay coast east of the Nelson River, numerous parallel, well-drained raised beaches present a striking pattern of successive white spruce-covered ridges, alternating with fens, polygonal peat plateaus, and peat plateaus. North of the Nelson River, beaches are more subdued and the terrain is dominated by fens, polygonal peat plateaus, and peat plateaus (ESWG, 1995). Also, permafrost with low to high ice content is widespread throughout the ecoregion; a mean annual ground surface temperature of about -2 °C to -4 °C provides an idea environment for permafrost occurrence (Johnson, 1987).

Characteristic wildlife includes barren-ground caribou, polar bear, arctic fox, brown lemming, snow and Canada goose, swan, sea ducks, and shorebirds. Beluga whale and seal are found in coastal waters. Human activities include trapping and hunting, marine mammal hunting,

fishing, recreation, and tourism. With a total population of approximately 1600 in 1995, the major communities in the ecoregion include Peawanuck, Fort Severn, and Churchill (ESWG, 1995).

Churchill has a borderline subarctic–low Arctic climate (Rouse, 1991). The major influence on the climate is the freezing and thawing of the Hudson Bay. Typically, ice formation begins in late October and November, the ice cover reaches its peak thickness in April and May, and break-up is usually complete by the first week of August (Markham, 1986; Saucier and Dionne, 1998; Gagnon and Gough, 2005b). In winter, the complete ice cover nullifies the moderating effects of the Hudson Bay waters. However, the occurrence of sea ice until late July in the southern and western shores of Hudson Bay contributes to the presence of continuous permafrost in the Churchill area (Gough and Leung, 2002). This has significant effects on the climate of the area, maintaining the ground temperature below 0 °C, and inhibiting surface water penetration from rain and snow melt. Thus, the energy that would otherwise be used to warm the surface is expended on evaporation (Maxwell, 1986). The average air temperature in July, the warmest month of the year, is 12 °C, and only four months have monthly mean temperatures above the freezing point (Gagnon and Gough, 2005b). Interestingly, the local ecosystem of Hudson Bay still thrives in this harsh climate. In particular, polar bears have adapted to the seasonality of sea ice cover. In winters and springs, the bears live on the ice platforms feeding or hibernating. Seal pups are the primary source of food for the year. During summer when the sea ice begins to disappear, the polar bears migrate to the land surface where they bear and raise their young in peat dens. Food sources over land are inadequate to sustain them and, consequently, the bears lose on average 0.85 kg per day while on land (Stirling and Derocher, 1993; Stirling et al., 1999). Consequently, there are concerns about the potential influence of climate change on the cryogenic cycle of the Hudson Bay ice cover, and its associated impacts on the population ecology of the

polar bears (Stirling et al., 1999). Churchill is one of the few locations where polar bears can be observed in the wild. As a result, it has become a favorite destination for tourists interested in seeing these fascinating animals. Typically, prime viewing times are in October and November; at the onset of ice freeze-up on Hudson Bay when the polar bears commence their migration back to seal-hunt territory.

3.1.2 Fraserdale, Ontario

Fraserdale (49°52′N, 81°37′W) is located southwest of James Bay in northern Ontario and on the southern perimeter of the Hudson Bay Lowlands. The measurement site is on a large clearing (about 300-400 m across) in the boreal forest, within a region that has extensive wetland coverage. The area is characterized by a relatively smooth shallow valley covered by tall grasses and several small trees. A 2 km × 2 km region around the site is characterized mainly by forest (50%), the Abitibi River (18%) and a logged area (Higuchi et al., 2003). According to a Landsat TM image at a 30 m resolution (Schut et al., 1994), the 3600 km^2 landscape around the tower comprises of 66% black spruce (Picea mariana) and Jack pine (Pinus banksiana), 20% open land after forest fires and logging, and 11% aspen (Populus tremuloides). The closest town to the Fraserdale site is Smooth Rock Falls (population ~2500) located about 70 km south of the site. To the north, the closest town is Moosonee (population ~1500) located about 200 km away. Timmins (population ~50 000) is the closest major city, located about 150 km south of Fraserdale (Worthy et al., 1998).

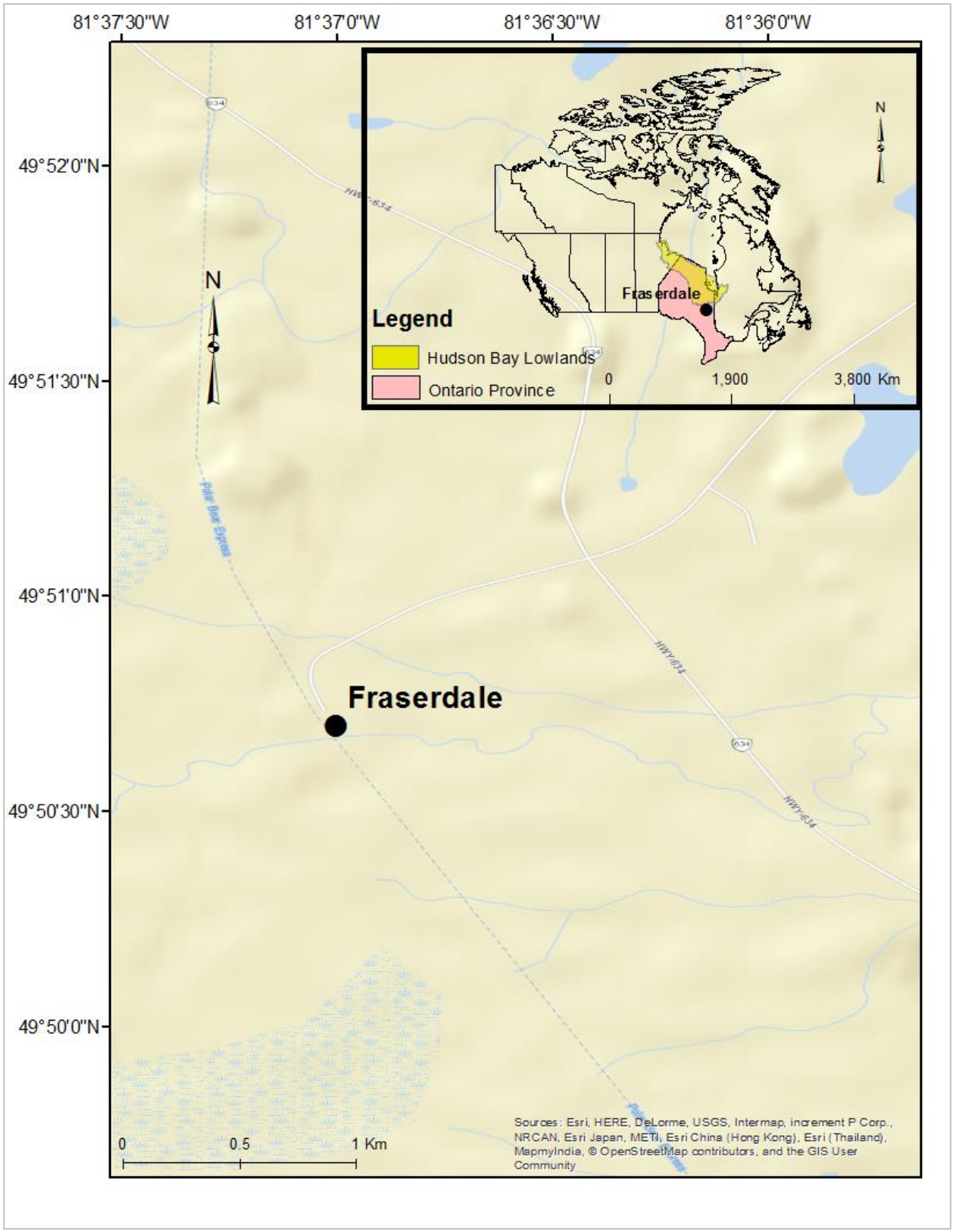

Figure 3. 3. Map of study area showing Fraserdale, Ontario.

The climate of Fraserdale has been well-described by Higuchi et al. (2003). The region is characterized by monthly mean temperatures below 0 °C for about 6 months of the year. In wintertime, mean temperatures are about −20 °C (with a range of −28 to −15 °C), and in summertime, mean temperatures are about 17 °C (with a range of 15 to 18 °C). The growing season (defined as starting after five consecutive days with temperatures above 5 °C) extends on average from 5 May to 15 September (133 d). The seasonal precipitation pattern over the Fraserdale region is controlled by the movement of the Arctic front. While annual precipitation is about 800 mm, summertime values could be as high as 100 mm per month when the Arctic front is located just north of Fraserdale. Overall, the region is climatologically influenced alternately by Arctic, maritime tropical, and modified Pacific air masses (Bryson, 1966). This results in four main different seasonal circulation patterns: (1) a winter pattern between November and February that brings air from the northwest, (2) a spring pattern between March and June that transports air from the north, (3) a summer pattern between July and September that brings air from the north as well as from the southwest, and (4) a short transitional fall pattern in October that brings air from the west. The winter and spring circulation patterns bring clean air from the north to Fraserdale, while anthropogenic influence on the sampled air is more likely associated with the summer circulation (Jobson et al., 1994).

3.2 Data Description and Measurement Procedures

3.2.1 Data Sources

This study uses a 5-year weekly CO_2 flask measurement record from 2008–2012, as well as continuous (hourly) atmospheric CO_2 mixing ratios for the year 2012. The study focuses on the Churchill and Fraserdale tower sites, and measurement data are provided by Environment Canada (http://www.ec.gc.ca/mges-ghgm/). All data were accessed from the World Data Centre for Greenhouse Gases (http://ds.data.jma.go.jp/gmd/wdcgg/).

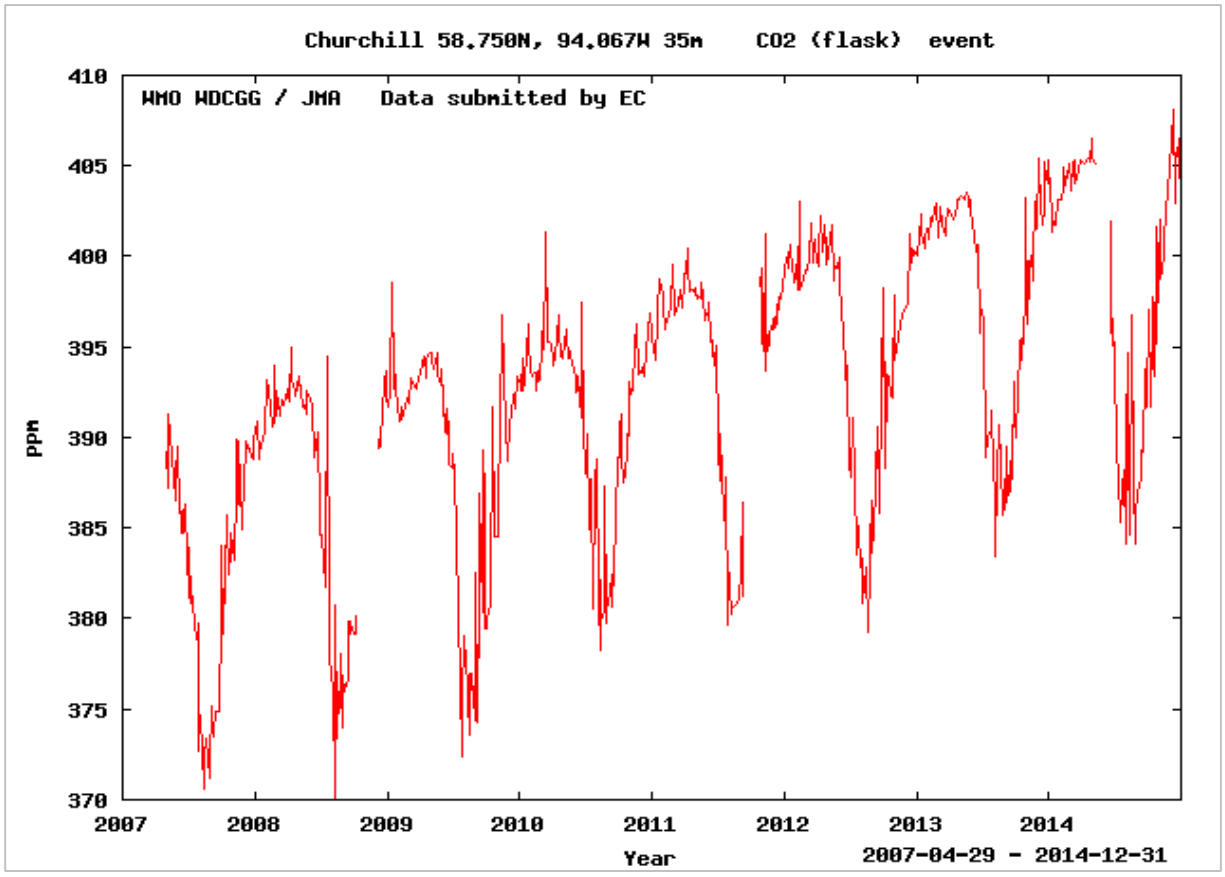

Figure 3. 4. Time series of weekly flask CO_2 measurements at Churchill, Manitoba, from 2007 to 2014.

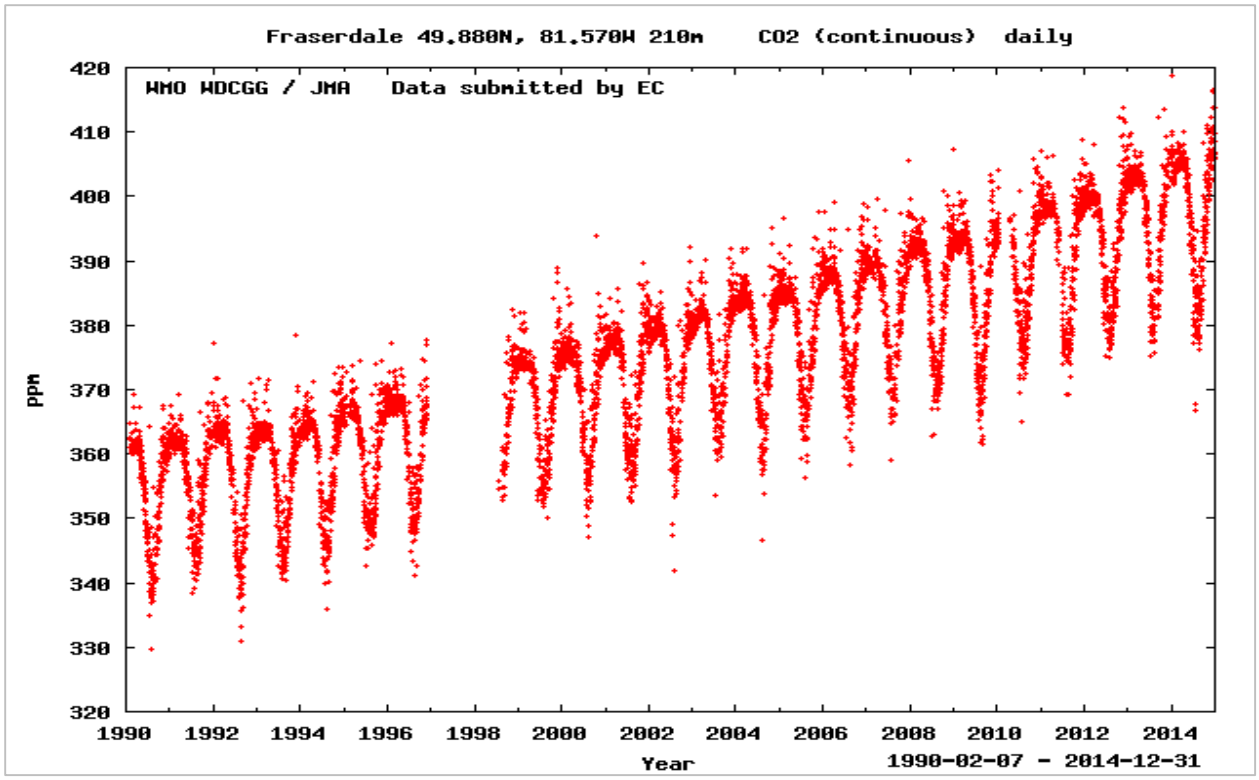

Figure 3. 5. Time series of daily CO_2 measurements at Fraserdale, Ontario, from 1990 to 2014.

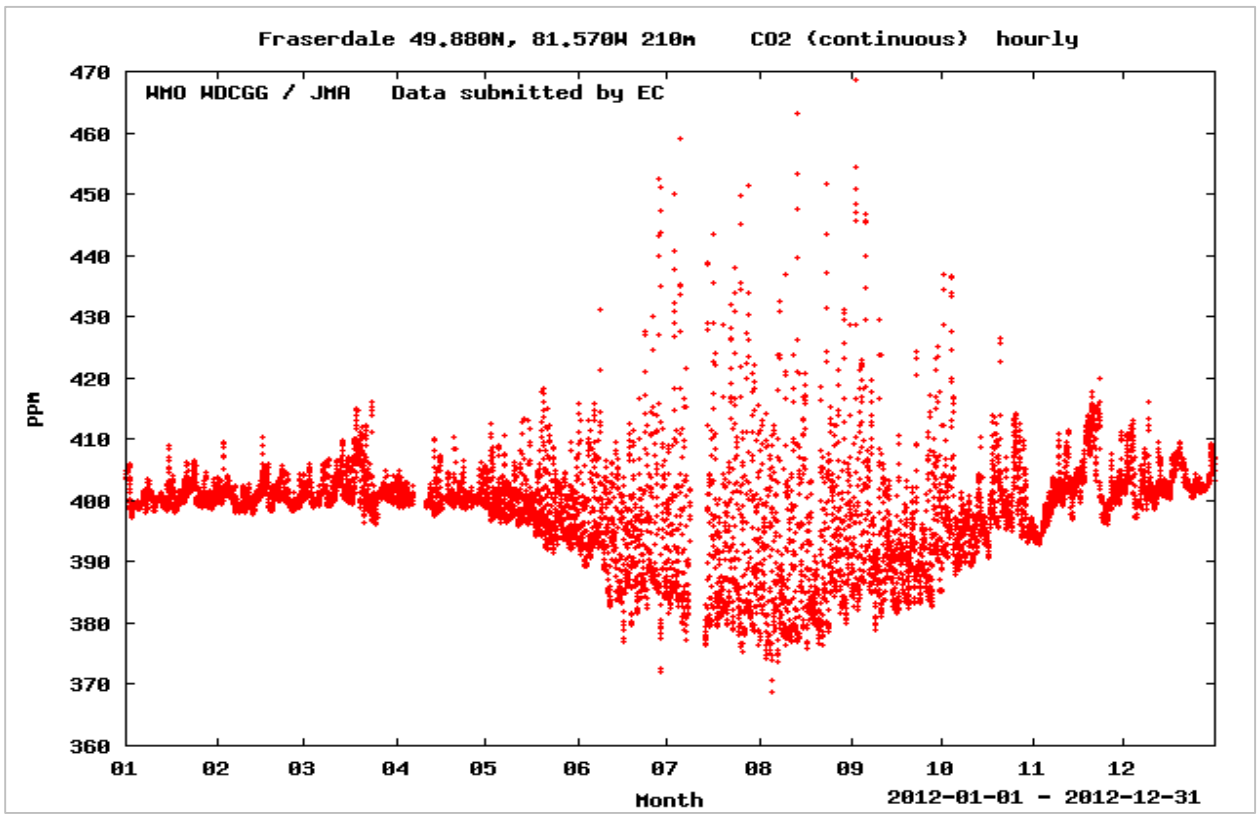

Figure 3. 6. Time series of hourly CO_2 measurements at Fraserdale, Ontario, from January to December, 2012.

3.2.2 Measurement Instrumentations

The Churchill Northern Studies Centre (located 23 km east of the town of Churchill) was founded in 1976 to foster scientific research in the region and is located at the site of the former Rocket Range established during the International Geophysical Year. Atmospheric greenhouse gas measurements began at the 60 m tower site with weekly flask sampling in 2007. Hourly measurements were initiated in October, 2011. Air samples are collected in pairs approximately weekly using flasks that have dual glass barreled valves with VitonR o-ring seals. A pumping unit is used to first flush the flasks, and then fill them in parallel to 15 psi. All samples are analyzed by Environment Canada in Toronto for carbon dioxide, methane, nitrous oxide, sulphur hexafluoride, carbon monoxide and hydrogen, by a Gas Chromatography equipped with a Flame Ionization Detector (GC-FID). The flask analysis system is fully automated via the HP Chemstation software. Ambient and standard gas samples are bracketed by two working tanks, and instrument response of the samples are compared to two standards of known CO_2 content. Measurements are reported in units of ppm of dry air relative to the WMO CO_2 standard scale (Worthy et al., 1998).

At Fraserdale, observation of CO_2 mixing ratios began at the top of the 40 m tower in 1990. Here, atmospheric CO_2 is continuously measured using non-dispersive infrared (NDIR) methodology (Trivett and Kohler, 1999). Ambient air is supplied to the NDIR using a vacuum pump that draws air through a sample line extending to the top of the 40 m tower. To permit the analysis on a dry air basis, the sample air is passed through a pressure relief valve set at 1 atm to release excess pressure (and air) and then through a large bead-filled glass trap immersed in a cryogenic bath set at −70 °C (Higuchi et al., 2003).

At each site, 11 standard tanks are used; 5 station tanks (~350, 365, 380,395 and 410 ppm), 4 working tanks (~355, 370, 385 and 400 ppm), one target tank (~365 ppm) and one zero tank (~340 ppm). At the top of every hour, a calibrated target gas and a zero gas are supplied to the NDIR analyzer for 5 minutes each. The working tanks are sequentially passed through the analyzer (for 5 minutes each) every 5 hours after the hourly target and zero tanks have been passed through the system. A Campbell Scientific data logger is used to control the automated injection sequence, and processes 5 minute averaged data records generated from the 1 second output signal voltages from the analyzer. A local server collects the data from the logger and transfers it via FTP to the server at Environment Canada in Toronto. All CO_2 measurements are directly traceable to the international absolute WMO mole fraction scale maintained by the WMO Central Calibration Laboratory at the Earth Systems Research Laboratory (ESRL) in Boulder, Colorado. There are 15 WMO primary standard gases calibrated at regular intervals, between 1 and 2 years, by the ESRL manometric system (Zhao et al., 1997). The uncertainty of the WMO CO_2 mole fraction scale is estimated to be approximately 0.07 ppm (Zhao and Tans, 2006).

Figure 3. 7. Environment Canada analytical measurement system for CO_2 using the non-dispersive infra-red (NDIR) methodology.

Figure 3. 8. A gas chromatographic analysis system used for weekly flask measurements at Environment Canada (EC).

Figure 3. 9. Analytical equipment used at EC for measuring the amount of selected trace gases in the flask air samples.

3.2.3 Data Processing

At the Churchill site, the automated control and sampling protocols for the GC Flask analysis system are programmed in methods and sequences within the ChemStation software. An injection protocol is typically comprised of a series (~15) of alternating standard tank (High and Low) injections to ensure system stability. The start of flask sample analysis includes two injections from a single flask followed by single injections from the two working tanks. This is then followed by two injections from the next flask and then repeated until all flasks have been analyzed. Overall, eight to ten flasks are attached to the system during a single run. Normally, the entire sequence is repeated, providing 4 individual sample analyses from each flask. To track potential biases and system errors, targets flasks of known concentration are also included in the sequence.

At the Fraserdale site, four separate processing modules written in MS Visual Basic are employed to calculate the final ambient concentration CO_2 mixing ratio values. The modules are run sequentially on the data collection server to perform various tasks:

First, Module 1 appends the most recently collected data with the previously collected data every 6 hours. There is one raw data file containing all raw data information collected by the logger for each year and for each site. This module also scans the entire file and extracts all the working (calibration every 11 days) and station tank calibration data.

Next, Module 2 automatically runs all the individual calibrations on the 4 working and target tanks (that take place every 11 days). This module also generates a historic calibration table that includes final valid calibration values. All the processed calibration files and the historic calibration table file are erased and regenerated after each data collection interval.

Subsequently, Module 3 isolates all the historic calibrations for each individual working and target tank (from the historic calibration table file) and fits a quadratic equation function through all the individual valid calibration values for each tank. This module also generates a new figure (one for each tank based on serial number) that includes the quadratic curve function and all the individual valid calibration values. After the calibration tank figures are generated, the module then updates (overwrites) the quadratic coefficients for the working and target tank equations, including historic tanks, in the station initialization file.

Finally, Module 4 calculates the ambient and target tank mixing ratios based on the four calibrated working tanks extracted from fitted curves. The mixing ratios are calculated in five-hour blocks between sweeps of working tanks.

3.3 Data Analysis Framework

3.3.1 Overview

This study employs an analysis framework designed to quantitatively interpret the influence of local– to regional–scale biospheric fluxes on atmospheric CO_2 concentration, by using spatially resolved "footprints" to link tower measurements to upwind regions. The modelling framework incorporates three main components: (1) An LPDM, the Stochastic Time-Inverted Lagrangian Transport (STILT) model that simulates air parcel trajectories and computes spatially/temporally resolved surface footprints; (2) Meteorological fields from the North American Regional Reanalysis (NARR), and the Global Data Assimilation System (GDAS) to drive the STILT model; (3) A carbon measurement and assimilation system (CarbonTracker) that

provides estimates of CO_2 sources and sinks over the continents and oceans. Overall, the aim of this model framework is to help address the primary objective of this study, which is to determine the biospheric flux contribution to the observed atmospheric CO_2 mixing ratios in the Churchill area of the Hudson Bay Lowlands.

3.3.2 The STILT Model

The Stochastic Time-Inverted Lagrangian Transport (STILT) model is a "near field" tool for simulating the upwind influence of atmospheric observations (Lin et al., 2003). This is particularly relevant because anthropogenic and biogenic emissions of trace gases at the surface cause large variations of atmospheric concentrations in the planetary boundary layer (PBL) from the ‘‘near field’’, where upwind sources and sinks have strong influence on observations. STILT is designed with the capability to represent near-field influences, transforming this noise to signal useful in diagnosing surface emissions. The model simulates atmospheric transport by following the time evolution of a particle ensemble, interpolating meteorological fields to the subgrid scale location of each particle. Additionally, turbulent motions are represented by a Markov chain process based statistically on observed meteorological parameters. Most importantly, the trajectories of air parcels are derived in a time-reversed manner thereby saving significant computational effort and time since the influence of upwind emissions at different times is modelled using a single particle backward simulation. This trajectory analysis is performed starting at the receptor (i.e. the measurement tower) towards the upwind regions, and sampling only the portion of the domain that influences the observations. Therein lies the advantage of the STILT model as a powerful tool within the CO_2 surface flux framework analysis.

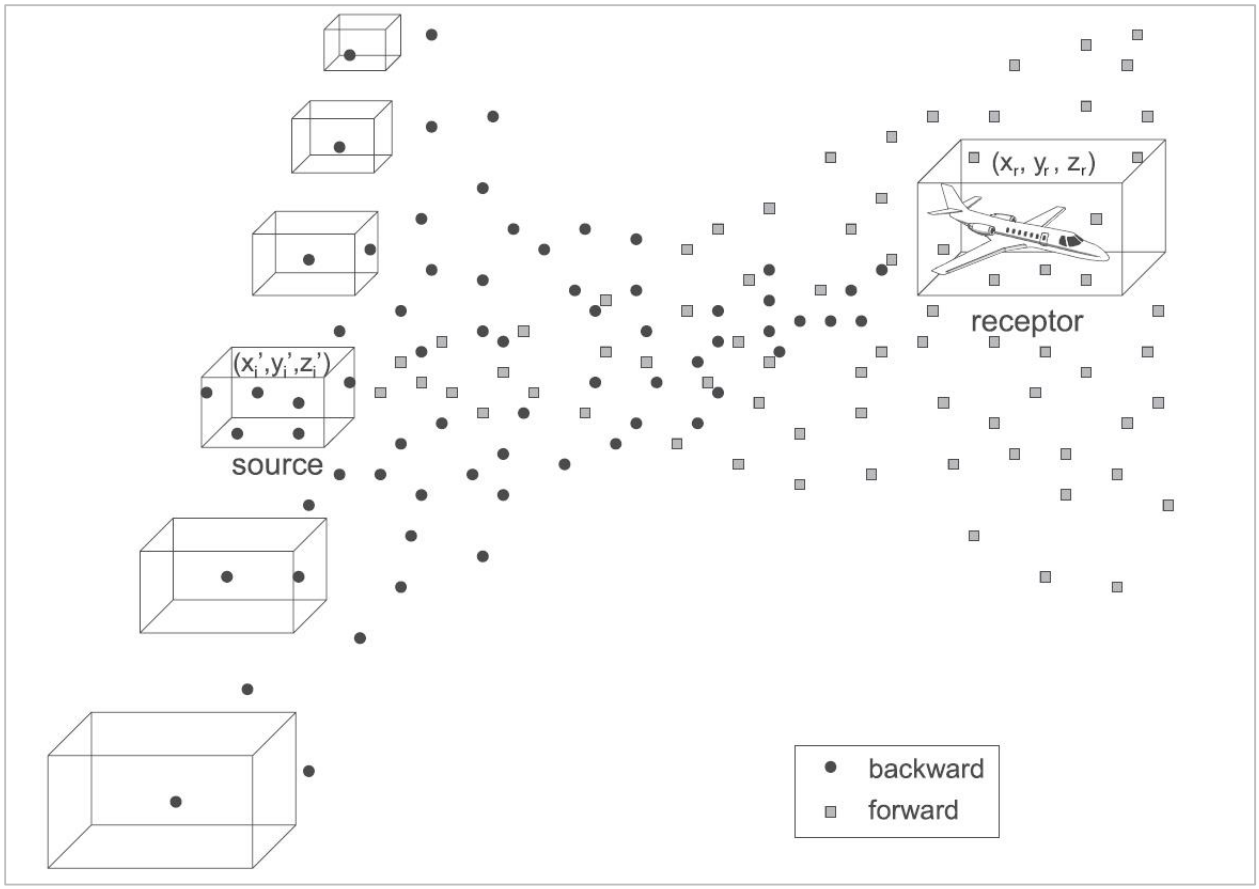

Figure 3. 10. Comparison of backward time and forward time simulations. A single backward time release of particles marks out the potential source region that influences the receptor, yielding the spatial and temporal dependence of the influence function $I(x_r,t_r \mid x,t)$, while numerous forward time runs from the entire model domain at multiple time steps are necessary. An empirical test for assessing time reversibility of the STILT model was carried out by simulating particles back in time from a box centred at the receptor location $x_r = (x_r,y_r,z_r)$. Then numerous forward time runs were conducted, starting from each potential source region (x_i',y_i',z_i'). The number of particles from the backward run which end up in the source box is compared with the number from the forward run that is found in the receptor box, after taking into account the differences in air density at the source and the receptor. STILT has been demonstrated to provide results consistent with its forward time counterpart (Lin et al., 2003).

STILT addresses two main challenges associated with atmospheric transport modelling: (1) "near-field" variability in concentration data associated with inhomogeneities of the distribution of surface fluxes, and (2) inadequate representation of PBL dynamics and transport. The term near field refers to the surface with which PBL air has come in contact ~4 days before arrival at the observation location or receptor (Cotton et al., 1995). Thus, the near-field domain affected by PBL processes may extend over 10^2–10^3 km, i.e., regional or even continental scale (Lin et al., 2003).

The STILT model is built upon the source code from Hybrid Single-Particle Lagrangian Integrated Trajectory (HYSPLIT) system (Draxler and Hess, 1998), using the mean advection scheme from HYSPLIT but employing a different turbulent module. Also, because of the common unavailability of PBL height in meteorological fields, the parameterization for PBL height has been modified from the simple "parcel method" in HYSPLIT—which specifies the PBL height as the level where the virtual potential temperature is greater than the surface value by 2° K—to a modified Richardson number method that generalizes to unstable, neutral, and stable conditions (Vogelezang and Holtslag, 1996). Furthermore, to satisfy the well-mixed criterion in the strongly inhomogeneous environment of the PBL, STILT adopts a unique way of transporting particles between vertical levels based on the reflection/transmission scheme for Gaussian turbulence (Thomson et al., 1997). In addition, particles in STILT are treated as air parcels with constant mass, and changes in air density are accounted for in order to conserve the amount of mass each vertically transported particle represents. This ensures that the simulations retain well-mixed particle distributions in an environment with Gaussian turbulence.

According to Gerbig et al. (2003), some of the prime advantages of using an LPDM such as STILT include: (1) The capability of the model to run backward in time makes it very efficient, such that only a single reversed-time model run is needed to extract the spatially and temporally resolved footprint for emissions at all previous times; (2) Due to the actual stochastic nature of air parcels transported by turbulence, modelling turbulent transport as the ensemble of stochastically transported particles is a more accurate representation than typical parameterizations such as diffusion coefficients; (3) Representation errors are avoided since influence is represented with particle distribution; (4) Interpolation of winds down to the exact location of a measurement enables footprints to be derived at much higher spatial resolution than the driving meteorological data (Gerbig et al., 2003b).

The STILT model yields realistic simulations of trajectories and associated footprints of air particles by satisfying the physical criteria of well-mixedness, resolution of the decay in autocorrelation, representation of close coupling between windshear and vertical turbulence, and consistent treatment of particles as air parcels with equal mass in both the mean and turbulent transport components (Lin et al., 2003). STILT's time-reversibility and suitability for applications to inverse analysis has been well-demonstrated by a wide variety of studies (Gerbig et al., 2003b; Kort et al., 2008; Zhao et al., 2009; Nehrkorn et al., 2010; Hegarty et al., 2013; Mallia et al., 2014).

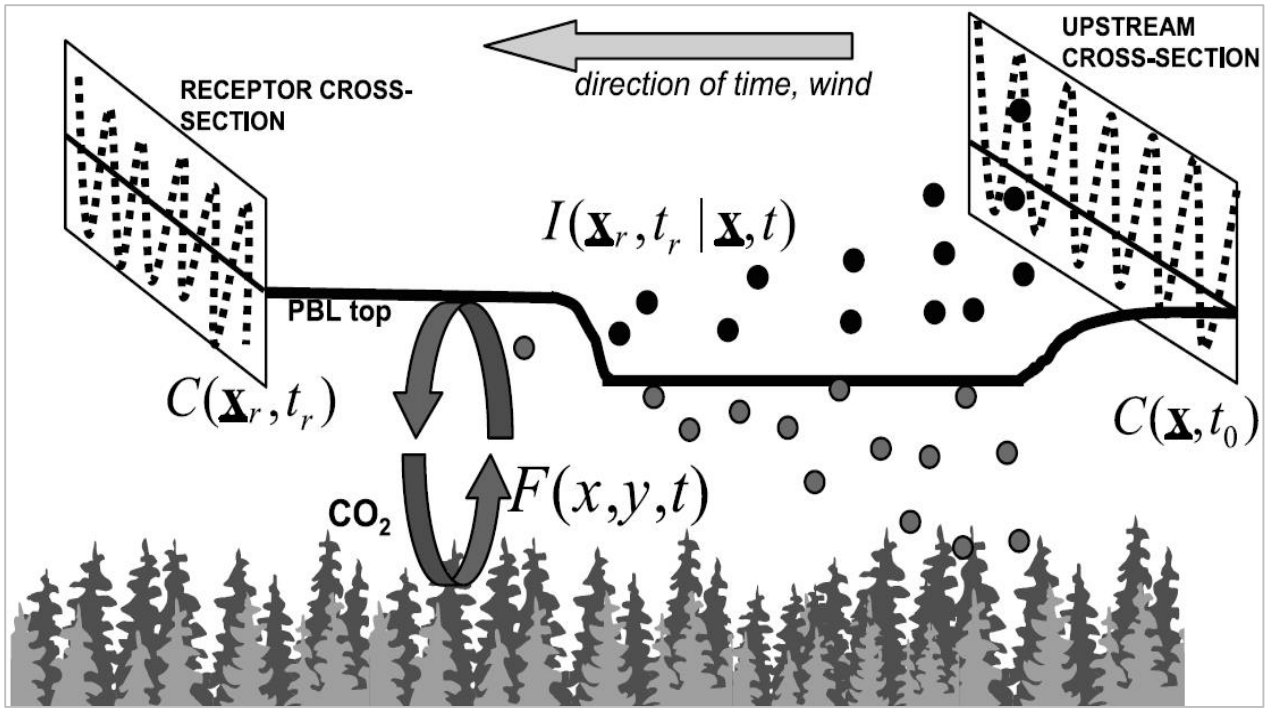

Figure 3. 11. The receptor-oriented analysis framework and the role played by the STILT model. Particle ensembles simulated by STILT provide the influence functions I(x_r, t_r|x, t) *that link receptor measurement* C(x_r, t_r) *to upstream surface fluxes* F(x, y, t) *and initial tracer field* C(x, t_0). *The particle ensembles are released at downstream receptors, and their locations prior in time mark out the upstream regions influencing the receptors (Lin et al., 2004b).*

3.3.3 Meteorological Fields

Wind fields, along with other meteorological variables are required to drive the STILT model. This study uses gridded data from the National Weather Service's National Centers for Environmental Prediction (NCEP) which are archived by NOAA's Air Resources Laboratory (ARL). The NCEP North American Regional Reanalysis (NARR) is a long-term, dynamically consistent, high-resolution, high-frequency, atmospheric and land surface hydrology dataset for the North American domain (Mesinger et al., 2006). The NARR was developed as a major improvement upon the earlier NCEP–NCAR Global Reanalysis (Kalnay et al., 1996; Kistler et al., 2001) with lateral boundary conditions provided by the NCEP–DOE GR2 (Kanamitsu et al., 2002). Other essential components of the NARR system include the NCEP regional Eta model and its Data Assimilation System, an upgraded Noah land-surface model, and other improved features such as precipitation assimilation and direct assimilation of radiances. Overall, the NARR dataset provides better analysis of land hydrology and land–atmosphere interaction, as well as improved atmospheric circulation throughout the troposphere (Mesinger et al., 2006).

The NARR meteorological data covers a period of about 35 years (1979–present), and is available on a 3 hourly, 32 km horizontal grid spacing, with 24 vertical levels. ARL downloads the NARR data in GRIB1 format from NOAA's National Operational Model Archive & Distribution System (ftp://nomads.ncdc.noaa.gov/NARR/) and converts to ARL format. The processed files are aggregated into monthly files and made available via NOAA's ARL FTP Server (ftp://arlftp.arlhq.noaa.gov/narr).

Outside the NARR domain, boundary conditions are provided by the Global Data Assimilation System (GDAS), available on a 3 hourly, 1 degree latitude-longitude horizontal grid, with 24 vertical levels. The dataset is available at ftp://arlftp.arlhq.noaa.gov/pub/archives/.

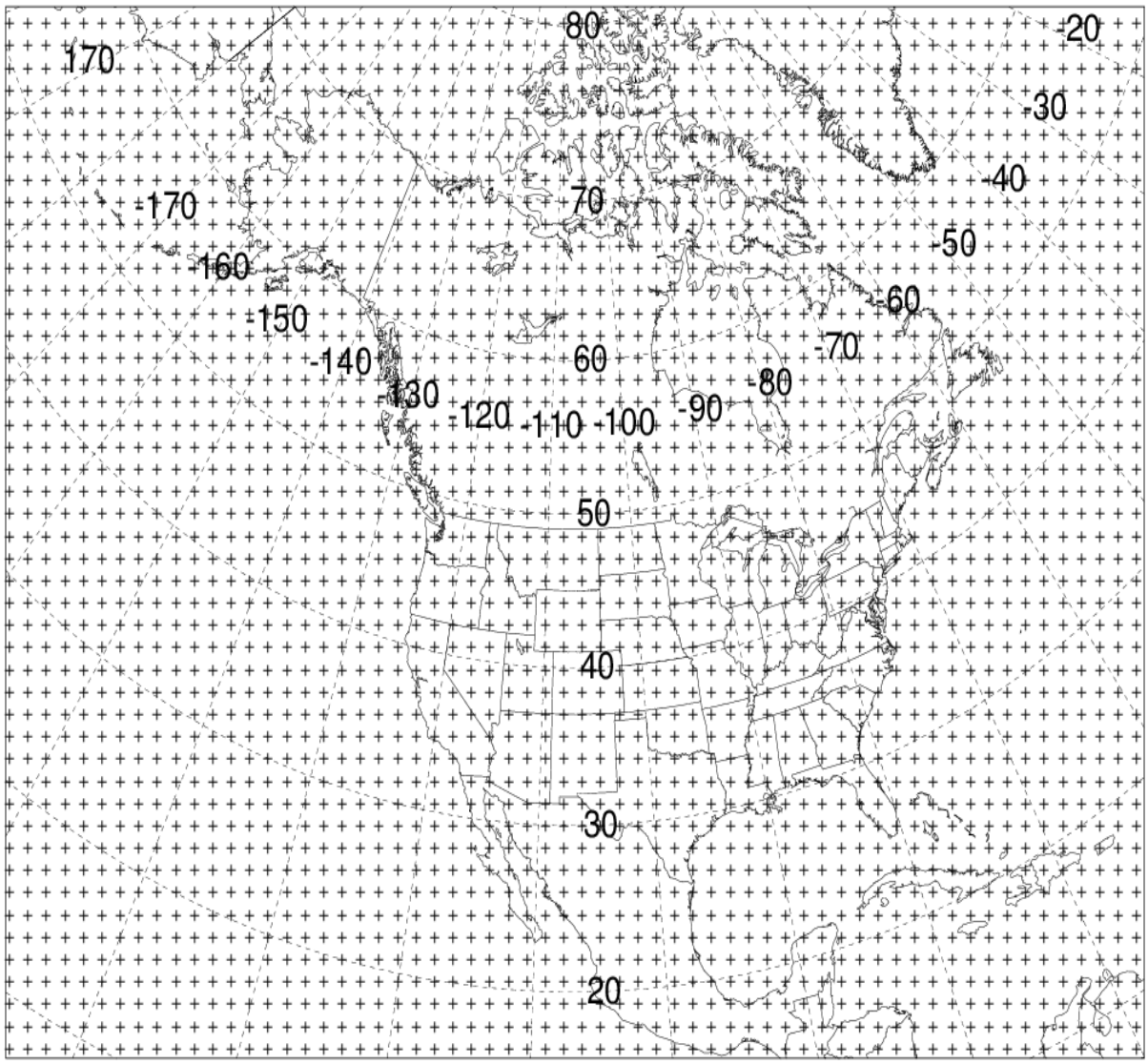

Figure 3. 12. The NCEP North American Regional Reanalysis (NARR) domain.

Coordinates	**Values**
Vert. Coordinate	2
Pole Lat.	90.00
Pole Lon.	0.00
Ref. Lat.	50.00
Ref. Lon.	-107.00
Ref. Grid	32.46
Orientation	0.00
Cone Angle	50.00
Sync X	1.00
Sync Y	1.00
Sync Lat.	6.98
Sync Lon.	-143.76
Special	0.00
Numb. Lat.	309
Numb. Lon.	237

Table 3. 1. Description of the NARR data grid.

Fields	**Units**	**Label**
Accumulated precipitation (3 h accumulation)	m	TPP3
Downward short wave radiation flux	W/m2	DSWF
PBL height	m	HPBL
Latent heat net flux at surface	W/m2	LHTF
Pressure at surface	hPa	PRSS
Pressure reduced to mean sea level	hPa	MSLP
Sensible heat net flux at surface	W/m2	SHTF
Total cloud cover	%	TCLD
Temperature at 2m AGL	K	TO2M
U-component of wind at 10 m AGL	m/s	U10M
V-component of wind at 10 m AGL	m/s	V10M
U-component of wind with respect to grid	m/s	UWND
V-component of wind with respect to grid	m/s	VWND
Geopotential height	gpm	HGTS
Temperature	K	TEMP
Pressure vertical velocity	hPa/s	WWND
Specific humidity	g/Kg	SPHU
Turbulent kinetic energy	Joul	TKEN

Table 3. 2. NARR meteorological fields.

Levels	**Height (hPa)**	**Variables**
Surface	0.0000	TPP3 DSWF HPBL LHTF PRSS MSLP SHTF TCLD T02M U10M V10M
level 1	1000.0	UWND VWND HGTS TEMP WWND SPHU TKEN
level 2	975.0	UWND VWND HGTS TEMP WWND SPHU TKEN
level 3	950.0	UWND VWND HGTS TEMP WWND SPHU TKEN
level 4	925.0	UWND VWND HGTS TEMP WWND SPHU TKEN
level 5	900.0	UWND VWND HGTS TEMP WWND SPHU TKEN
level 6	875.0	UWND VWND HGTS TEMP WWND SPHU TKEN
level 7	850.0	UWND VWND HGTS TEMP WWND SPHU TKEN
level 8	825.0	UWND VWND HGTS TEMP WWND SPHU TKEN
level 9	800.0	UWND VWND HGTS TEMP WWND SPHU TKEN
level 10	775.0	UWND VWND HGTS TEMP WWND SPHU TKEN
level 11	750.0	UWND VWND HGTS TEMP WWND SPHU TKEN
level 12	725.0	UWND VWND HGTS TEMP WWND SPHU TKEN
level 13	700.0	UWND VWND HGTS TEMP WWND SPHU TKEN
level 14	650.0	UWND VWND HGTS TEMP WWND SPHU TKEN
level 15	600.0	UWND VWND HGTS TEMP WWND SPHU TKEN
level 16	550.0	UWND VWND HGTS TEMP WWND SPHU
level 17	500.0	UWND VWND HGTS TEMP WWND SPHU
level 18	450.0	UWND VWND HGTS TEMP WWND SPHU
level 19	400.0	UWND VWND HGTS TEMP WWND SPHU
level 20	350.0	UWND VWND HGTS TEMP WWND SPHU
level 21	300.0	UWND VWND HGTS TEMP WWND SPHU
level 22	200.0	UWND VWND HGTS TEMP WWND SPHU
level 23	100.0	UWND VWND HGTS TEMP WWND SPHU

Table 3. 3. NARR vertical layers and variables.

3.3.4 CO_2 Mole Fraction and Surface Flux Fields

Carbon estimates are required to represent sources and sinks that affect atmospheric CO_2 concentration on regional spatial and temporal scales. This study employs a carbon measurement and assimilation system, CarbonTracker that provides quantitative estimates of atmospheric carbon uptake and release for North America and the rest of the world (CarbonTracker CT2013, http://carbontracker.noaa.gov). The surface fluxes produced in CarbonTracker are consistent with observed global patterns of CO_2 in the atmosphere. By design, the assimilation process begins by forecasting global atmospheric CO_2 mole fractions from a combination of CO_2 surface exchange models and an atmospheric transport model (TM5) driven by meteorological fields from the European Centre for Medium-Range Weather Forecasts (ECMWF). Subsequently, the model forecast results are optimized by minimizing the difference between the resulting three-dimensional CO_2 distribution and observations (Peters et al., 2007). All surface flux fields in CarbonTracker are available every 3 h from 2000 to 2012, at a 1° x 1° horizontal grid resolution.

The analysis framework used in this study extracts terrestrial biosphere fluxes, fossil fuel sources, and wildfire emissions from the CarbonTracker-2013 flux fields. The biospheric model used in CarbonTracker is the Carnegie-Ames Stanford Approach (CASA) biogeochemical model. This model calculates global carbon fluxes using input from weather models to drive biophysical processes, as well as satellite observed Normalized Difference Vegetation Index (NDVI) to track plant phenology (Potter et al., 1996, 1999; Potter and Klooster, 1997). For the fossil fuel module, CarbonTracker uses two different fossil fuel CO_2 emissions datasets: The Miller fossil fuel emission inventory (Boden et al., 2013), and the ODIAC emissions dataset (Oda and Maksyutov, 2011). The fire module currently used in CarbonTracker is based on the Global Fire Emissions Database (GFED), which uses the CASA biogeochemical model to estimate the carbon fuel in

various biomass pools. Background CO_2 concentrations are retrieved from CarbonTracker 3D mole fraction fields, which have a temporal resolution of 3 h, with a gridded resolution of 3° × 2° at the global scale and 1° × 1° for North America.

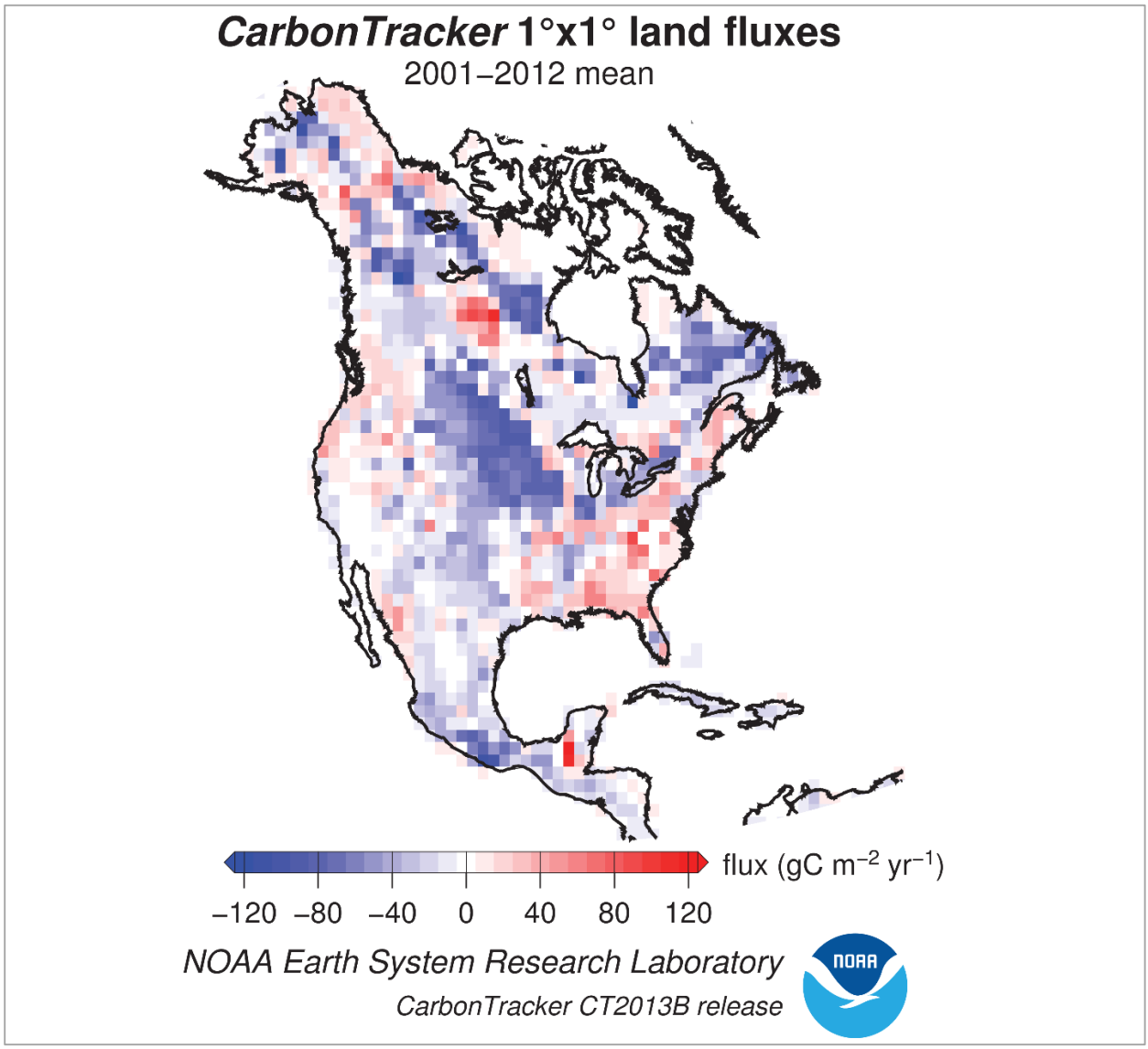

Figure 3. 13. The pattern of net ecosystem exchange (NEE) of CO_2 for the North American land biosphere. The fluxes shown above are the long-term averages over the time period 2001-2012, as estimated by CarbonTracker. This NEE represents land-to-atmosphere carbon exchange from photosynthesis and respiration in terrestrial ecosystems, as well as contribution from fires. Fossil fuel emissions are excluded. Negative fluxes (blue colors) represent CO_2 uptake by the land biosphere, while positive fluxes (red colors) indicate regions where the land biosphere is a net source of CO_2 to the atmosphere.

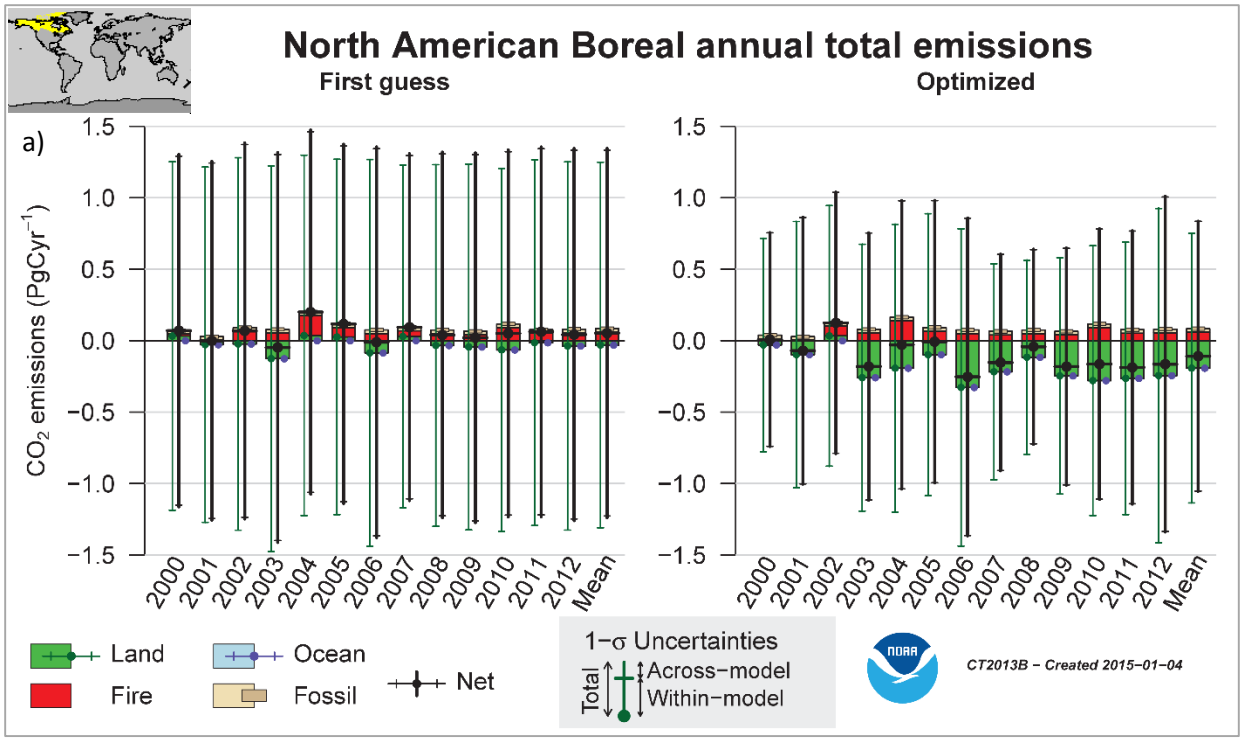

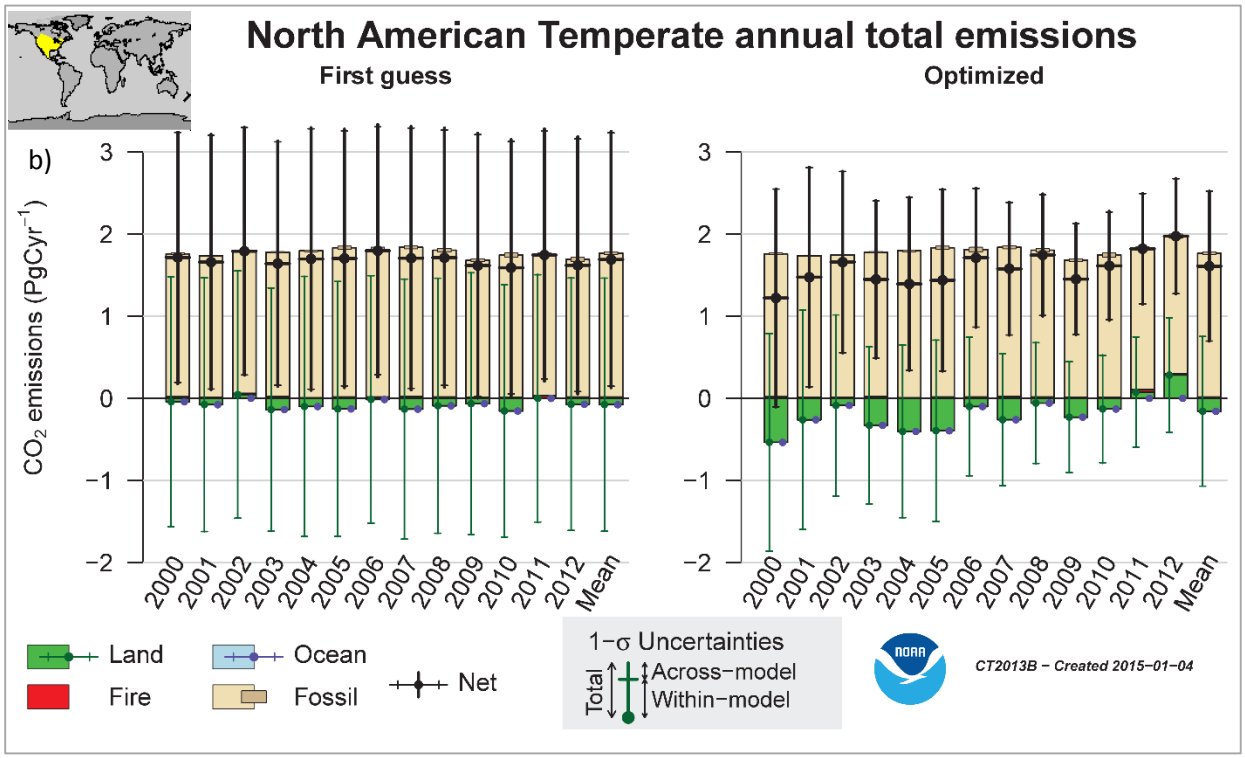

Figure 3. 14. Annual total CO_2 emissions estimated by CarbonTracker. Four types of surface-to-atmosphere exchange are shown: fossil fuel emissions, terrestrial biosphere flux excluding fires, direct emissions from fires, and air-sea gas exchange. Negative emissions indicate that the flux removes CO_2 from the atmosphere, and such sinks have bars that extend below zero. The net surface exchange is the sum of all four components. (a) North American Boreal region. (b) North American Temperate region.

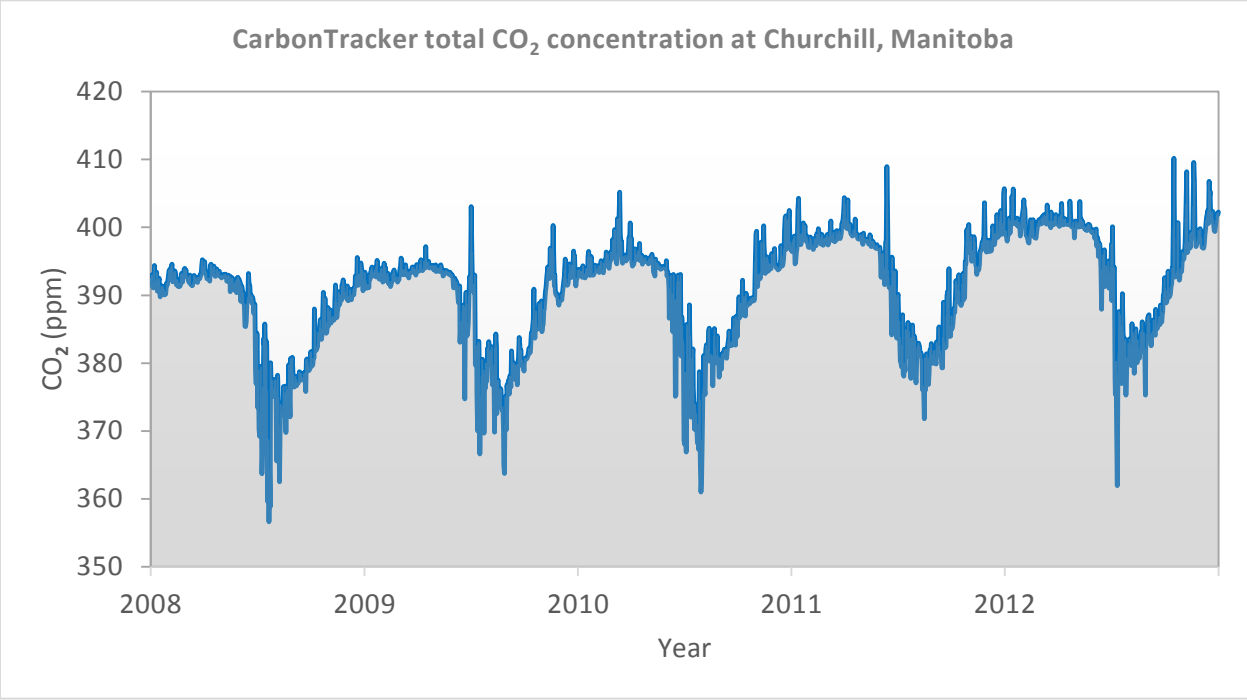

Figure 3. 15. Time series of CarbonTracker total atmospheric CO_2 concentrations at Churchill, Manitoba from 2008–2012.

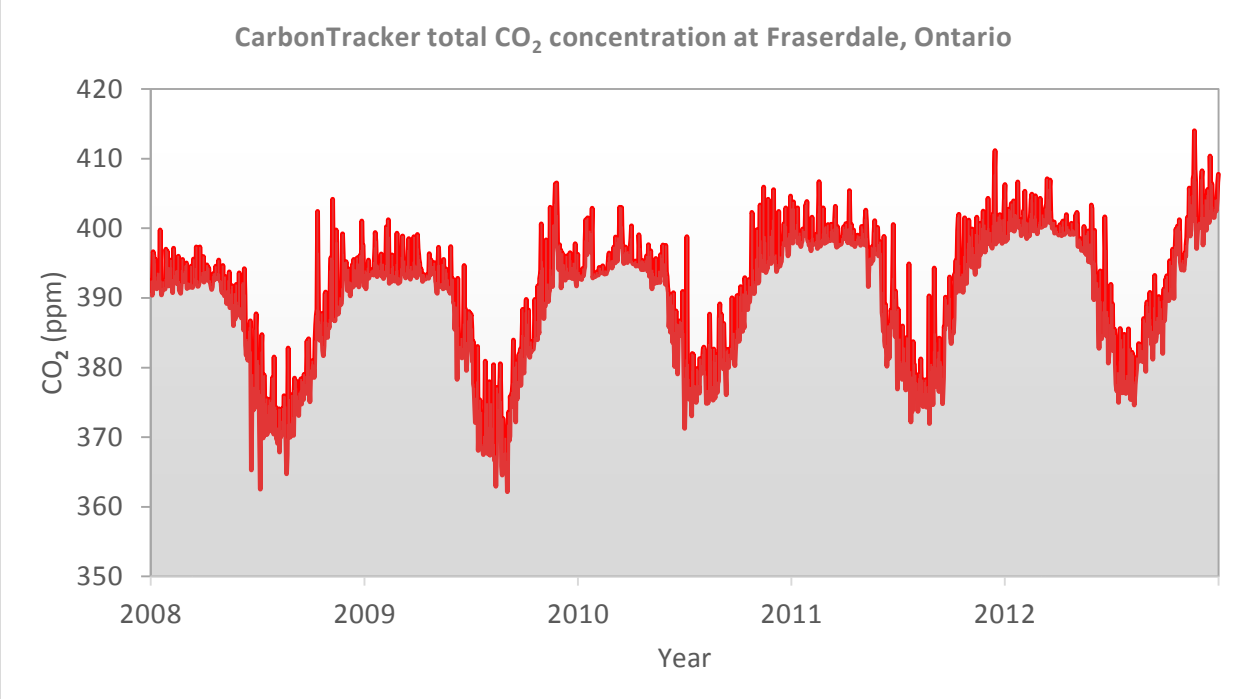

Figure 3. 16. Time series of CarbonTracker total atmospheric CO_2 concentrations at Fraserdale, Ontario from 2008–2012.

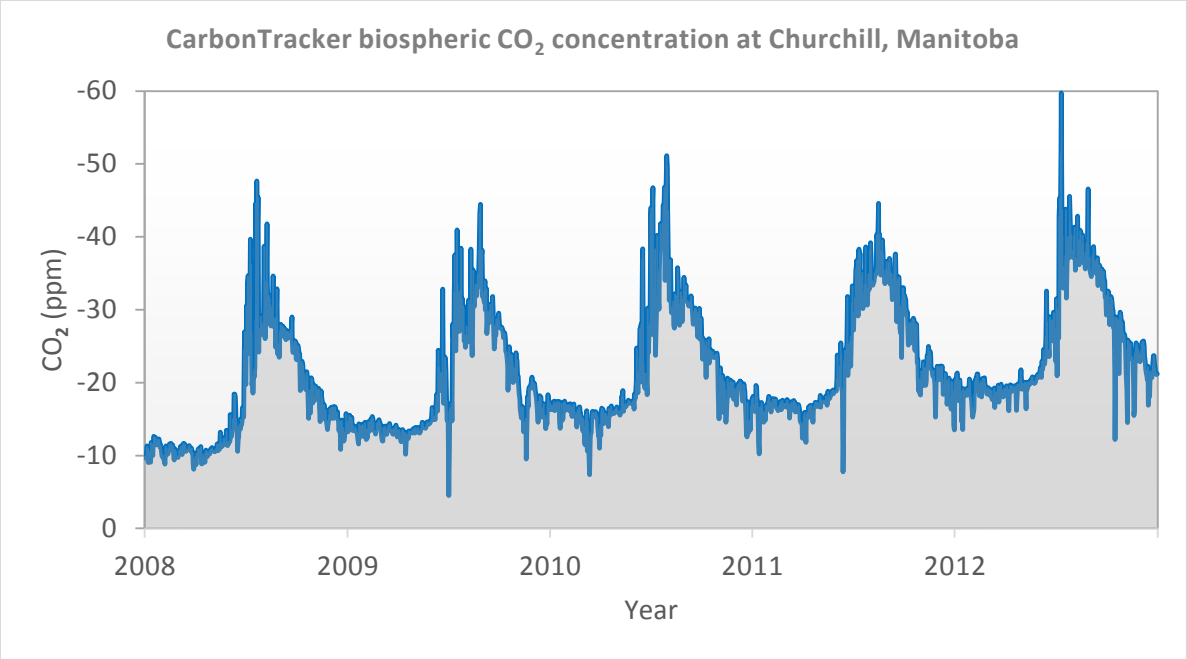

Figure 3. 17. Time series of the component of total CO_2 due to terrestrial biosphere exchange with the atmosphere (excluding wildfires), as estimated by CarbonTracker for Churchill, Manitoba (2008–2012).

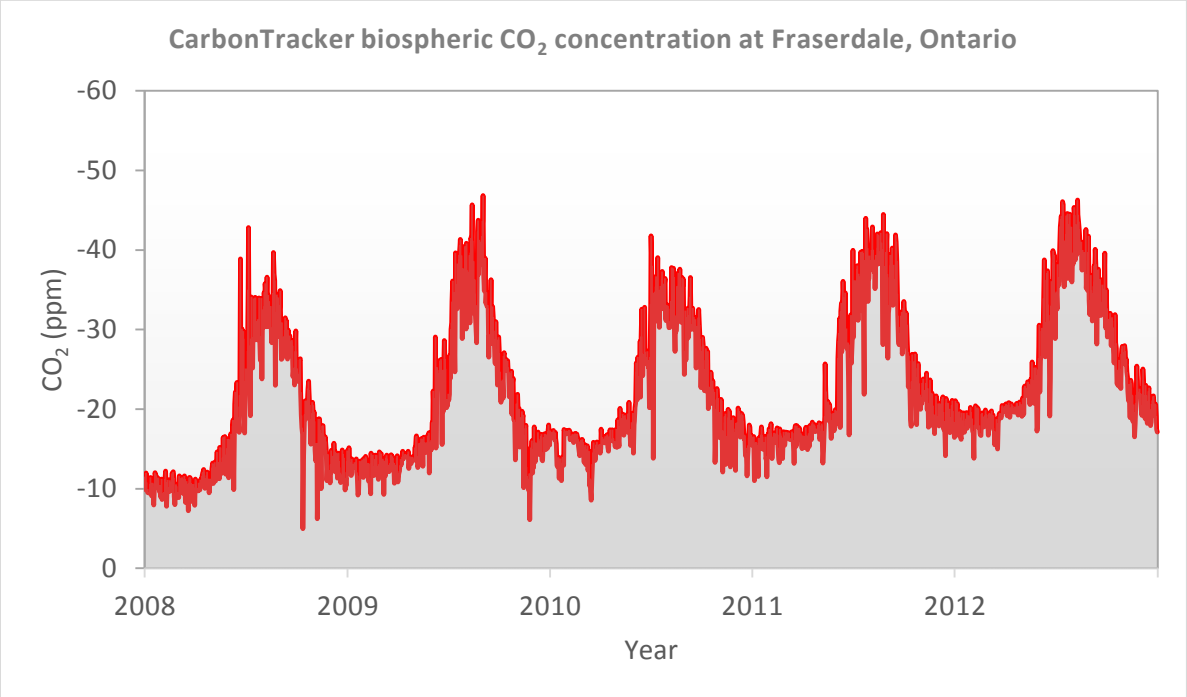

Figure 3. 18. Time series of the component of total CO_2 due to terrestrial biosphere exchange with the atmosphere (excluding wildfires), as estimated by CarbonTracker for Fraserdale, Ontario (2008–2012).

3.3.5 Analysis Procedures and Core Functions

The STILT model package is freely available on http://www.stilt-model.org/, with installation details, system requirements and additional setup procedures. A working copy of the STILT repository can be retrieved via *Subversion* (https://subversion.apache.org/). The STILT program is written in FORTRAN code; however, in order to make computation more efficient, a layer of code written in higher-level language has been designed and implemented to interact directly with the core FORTRAN model. These scripts are written in the R language (OpenSource implementation of the S-statistical analysis language). The source code, installation files, and documentation on R can be downloaded from the R Project for Statistical Computing: http://www.r-project.org/.

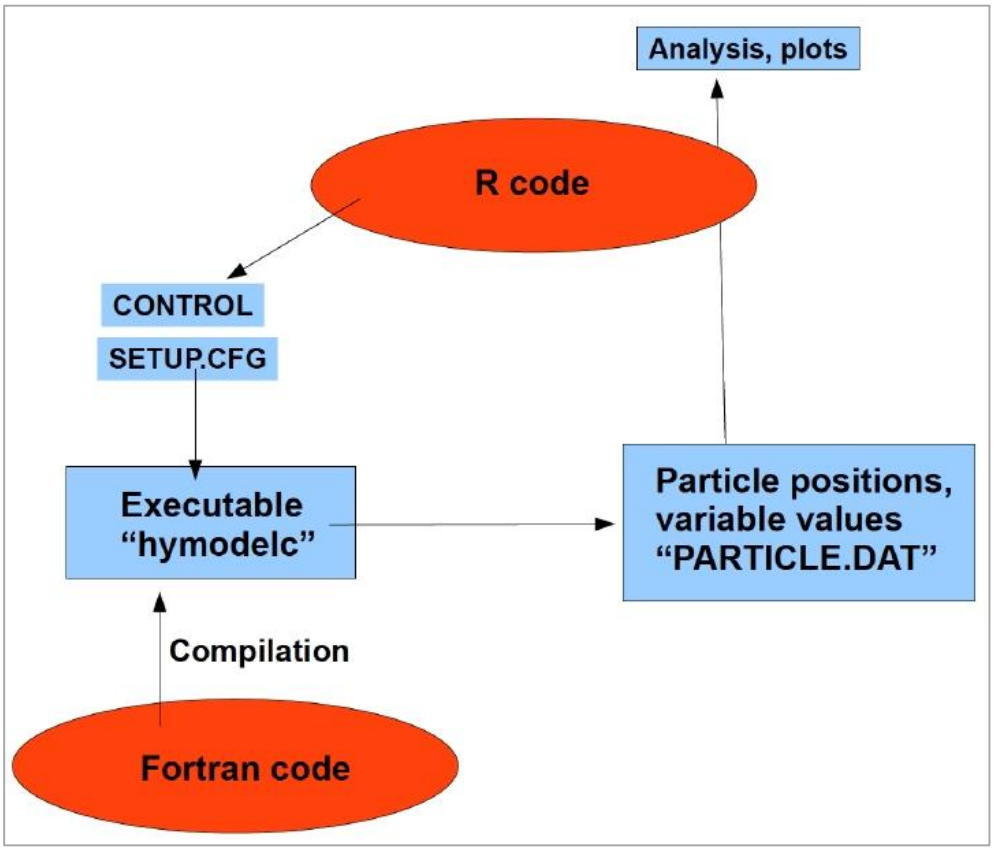

Figure 3. 19. Schematic of how the FORTRAN and the R code interact with one another in STILT (Source: Lin and Gerbig, 2010).

A typical STILT simulation begins by configuring the *CONTROL* and *SETUP.CFG* files. Some key parameters include; starting times and location, measurement height (agl), number of particles, number of hours to run the model (backwards), specified fraction of PBL height, integration timestep, and the total number of output variables. The main model inputs are the meteorological fields, 3D mole fraction fields, and surface flux fields.

Given input meteorological data from NARR and boundary conditions by GDAS, the STILT model transports an ensemble of 3000 particles (air parcels) 3 days backward in time. The trajectories are computed using the *Trajec* core function. This workhorse function runs the STILT model by calling the FORTRAN executable *hymodelc*, and uses the *CONTROL* and *SETUP* configuration files to generate an output file called *PARTICLE.DAT*. Then, *Trajec* reads in the *PARTICLE.DAT* file, matching it with the other specified output variables. The final output from the run is written to an external file in *.RData* format. The details of this *Trajec* output can be retrieved from the .Rdata file to create map of particle trajectories, or exported as ASCII/CSV data for further analysis.

```
#CONTROL
12 6 30 21              #yr ('0'=>2000), mon, day, hr [UTC]
1                       #number of starting locations
49.88 -81.57 40         #starting location: lat, lon, height [m AGL]
-72                     #number of hours to run model (-ve sign denotes backward run)
0                       #vertical motion option (0:data 1:isob 2:isen 3:dens 4:sigma)
25000.0                 #top of model domain [m AGL]
10                      #number of input meteorological data
/olalekan/model_input/  #meteorological data directory
NARR201206A             #meteorological filename
/olalekan/model_input/
NARR201206B
/olalekan/model_input/
NARR201206C
/olalekan/model_input/
NARR201206D
/olalekan/model_input/
NARR201206E
/olalekan/model_input/
gdas1.jun12.w1
/olalekan/model_input/
gdas1.jun12.w2
/olalekan/model_input/
gdas1.jun12.w3
/olalekan/model_input/
gdas1.jun12.w4
/olalekan/model_input/
gdas1.jun12.w5
1
test
1
0.01
00 00 00 00 00
1
0.0 0.0
0.5 0.5
30.0 30.0
./
cdump
1
100
00 00 00 00 00
00 00 00 00 00
00 2 00
1
0.0 0.0 0.0
0.0 0.0 0.0 0.0 0.0
0.0 0.0 0.0
0.0
0.0
```

Table 3. 4. Structure of the CONTROL file for STILT. Various parameters can be changed to modify the STILT run.

```
#SETUP
TRATIO=0.75,
INITD=0,
KHMAX=9999,
NUMPAR=3000,
QCYCLE=0,
KRND=6,
FRMR=0.0,
DELT=30,
ISOT=0,
OUTFRAC=0.9,
NDUMP=0,
RANDOM=1,
OUTDT=0,
VEGHT=0.5,
NTURB=0,
ICONVECT=1,
ZICONTROLTF=0,
WINDERRTF=0,
IVMAX=11,
VARSIWANT='time','indx','lati','long','zagl','zsfc','foot','samt','dmas','mlht','pres',
/
```

Table 3. 5. Structure of SETUP file for STILT. SETUP.CFG is a 'namelist' file, which can alter the behavior of the model without having to recompile it. Explanation of each parameter is given below.

NUMPAR—number of particles to be run (default: 100)
DELT—integration timestep [min]; if set to 0.0, then timestep is dynamically determined
TRATIO—maximum fraction of gridcell to be traveled by a particle in a single integration timestep. This determines the timestep is DELT is set to be dynamic (default: 0.75)
ISOT—flag used to set the isotropic turbulence option. The default value of 0 results in the computation of horizontal turbulence from wind field deformation. Setting this flag to 1 results in the horizontal turbulence to be the same in both the U- and V- directions. (default: 0)
TLFRAC—the fraction of T_L (Lagrangian timescale) to set as timestep in dispersion subroutine. The smaller this fraction is, the more finely the turbulence is resolved. (default: 0.1)
NDUMP—is a flag that can be set to dump out all the particle/puff points at the end of a simulation to a file called PARDUMP. This file can be read at the start of a new simulation to continue the previous calculation. Valid NDUMP settings: 0 - no I/O, 1- read and write, 2 - read only, 3 - write only (default: 0)
RANDOM—flag that tells random number generator whether to have a different random sequence each time model is run (0-FALSE; 1-TRUE); if set FALSE, then generates same random sequence each time, which is useful for debugging purposes (default: 1)
OUTDT—interval to output data to PARTICLE.DAT [min]; 0.0 means output is written every timestep (default: 0.0)
NTURB—No Turbulence flag; 1 sets run to simulate mean trajectories, 0 sets run to include turbulence (default: 0)
VEGHT—height [fraction of PBL ht or m] below which a particle's time spent is tallied; useful if want to specify a certain ht as 'seeing' ground vegetation. If <=1.0, then specifies fraction of PBL ht (default: 0.5)
OUTFRAC—the fraction of particles that are allowed to leave model domain (given by met. data); if exceeded, model stops (default: 0.9)

ICONVECT—flag for convection. If set to 1, then runs excessive convection as described in Gerbig et al., *J. Geophys. Res.*, *108* (D24), 4757, doi:10.1029/2003JD003770, 2003. For specialized RAMS output, the particles will be vertically redistributed according to the outputted convective mass fluxes (default: 0)
WINDERRTF—flag that specifies whether to have particle motions be affected by horizontal wind errors. (default: 0) If set to 1, then STILT looks for file called "WINDERR" that has four lines, with one number on each line: 1. Standard deviation of errors [m/s] 2. Correlation timescale of errors [min] 3. Vertical correlation lengthscale of errors [m] 4. Horizontal correlation lengthscale of errors [km]. All the statistical properties specified in 1.~4. are applied equally to the U- and V- wind components.
ZICONTROLTF—flag that species whether to scale the PBL heights in STILT uniformly in the entire model domain. (default: 0) If set to 1, then STILT looks for file called 'ZICONTROL' that species the scaling for the PBL height. The first line of ZICONTROL indicates the number of hours that the PBL height will be changed, and each subsequent line indicates the scaling factor for that hour. A sample ZICONTROL file could contain:

```
2
1.5
0.4
```

This file would alter the PBL heights for the first two hours of the model runtime, increasing the PBL height by 50% during the first hour and decreasing it to only 40% of the original value.
IVMAX—the total number of variables to be outputted (see VARSIWANT) (default: 5)
VARSIWANT—a list of 4-letter codes specifying variables to be outputted. See next section for complete list of variables that can be outputted (default: 'time', 'indx', 'long', 'lati', 'zagl')

Table 3. 6. Explanation of parameters in SETUP.CFG (Source: Lin and Gerbig, 2010).

List of Variables that can be Outputted from STILT	
time	time since start of simulation; negative if going backward in time [min]
indx	particle index
long	longitude position of particle [degrees]
lati	latitude position of particle [degrees]
zagl	vertical position of particle [m above ground level]
sigw	standard deviation of vertical velocity; measure of strength of vertical turbulence [m/s]
tlgr	Lagrangian decorrelation timescale [s]
zsfc	terrain height [m above sea level]
icdx	cloud index when using RAMS (Grell scheme) [1=updraft, 2=environment, 3=downdraft]
temp	air temperature at lowest model layer [K]
samt	amount of time particle spends below VEGHT (see section on SETUP.CFG) [min]
foot	'footprint', or sensitivity of mixing ratio to surface fluxes [ppm/(μmole/m^2/s)]
shtf	sensible heat flux [W/m^2]
lhtf	latent heat flux [W/m^2]
tcld	total cloud cover [%]
dmas	particle weight changes due to mass violation in wind fields [initial value = 1.0]
dens	air density [kg/m^3]
rhfr	relative humidity fraction [0~1.0]
sphu	specific humidity [g/g]
solw	soil moisture
lcld	low cloud cover [%]
zloc	limit of convection heights [m]
dswf	downward shortwave radiation [W/m^2]
wout	vertical mean wind [m/s]
mlht	mixed-layer height [m]
rain	total rainfall rate [m/min]
crai	convective rainfall rate [m/min]

Table 3. 7. The 4-letter codes of variables that could be specified for VARSIWANT in SETUP.CFG to produce the corresponding outputs. These data will be written to a text file called PARTICLE.DAT (Source: Lin and Gerbig, 2010).

time	index	lat	lon	agl	grdht	foot	sampt	dmass	zi	pres
-30	1	58.828	-94.0715	133.3932	27.9799	0.062311	6.1011	1.03	250	994.1
-30	2	58.8387	-94.0922	195.9706	27.9799	0.084767	8.2998	1.006	250	985.87
-30	3	58.8026	-94.0192	17.7542	27.9799	0.306495	29.9999	1.19	250	1009.42
-30	4	58.8281	-94.0734	221.7818	27.9799	0.153197	15	1.041	250	982.52
-30	5	58.8232	-94.062	69.2069	27.9799	0.167509	16.3944	1.091	250	1002.56
-30	6	58.8151	-94.0431	124.0398	27.9799	0.276812	27.0956	1.056	250	995.33
-30	7	58.8337	-94.0822	170.1579	27.9799	0.090871	8.8975	1.037	250	989.26
-30	8	58.8059	-94.0254	38.5508	27.9799	0.306495	29.9999	1.188	250	1006.65
-30	9	58.8164	-94.0456	83.4246	27.9799	0.282285	27.6295	1.083	250	1000.68
-30	10	58.8074	-94.0278	90.8192	27.9799	0.306494	29.9999	1.176	250	999.7
-30	11	58.8186	-94.0517	136.9626	27.9799	0.257084	25.1652	1.036	250	993.63
-30	12	58.8173	-94.048	104.437	27.9799	0.217449	21.2869	1.046	250	997.91
-30	13	58.8081	-94.0346	76.1401	27.9799	0.306494	29.9999	1.165	250	1001.64
-30	14	58.8806	-94.1357	351.7918	27.9799	0.037627	3.6842	0.99	250	965.72
-30	15	58.8205	-94.0508	167.2242	27.9799	0.19772	19.3565	1.048	250	989.65
-30	16	58.8184	-94.0514	183.0464	27.9799	0.212561	20.8087	1.056	250	987.57
-30	17	58.8178	-94.0501	164.798	27.9799	0.242243	23.7131	1.039	250	989.97
-30	18	58.8048	-94.023	52.2207	27.9799	0.306495	29.9999	1.188	250	1004.82
-30	19	58.8563	-94.1153	245.8038	27.9799	0.026962	2.64	0.99	250	979.42
-30	20	58.8283	-94.069	156.8661	27.9799	0.102846	10.0699	1.037	250	991.01
-30	21	58.8161	-94.0459	177.5183	27.9799	0.242243	23.7131	1.059	250	988.29
-30	22	58.8045	-94.0239	58.2385	27.9799	0.306495	29.9999	1.188	250	1004.02
-30	23	58.8045	-94.0273	38.9646	27.9799	0.306495	29.9999	1.188	250	1006.59
-30	24	58.8186	-94.0587	43.6607	27.9799	0.202462	19.8139	1.102	250	1005.96
-30	25	58.8026	-94.0181	16.2613	27.9799	0.306495	29.9999	1.189	250	1009.62
-30	26	58.8053	-94.0349	56.3125	27.9799	0.306495	29.9999	1.188	250	1004.28
-30	27	58.8056	-94.0245	15.9264	27.9799	0.306495	29.9999	1.188	250	1009.66
-30	28	58.834	-94.0876	197.7939	27.9799	0.060858	5.9588	1.027	250	985.63
-30	29	58.861	-94.1031	342.9727	27.9799	0.061778	6.0488	0.996	250	966.86
-30	30	58.8552	-94.099	296.4706	27.9799	0.099135	9.7066	1.008	250	972.87
-30	31	58.8073	-94.0316	60.1035	27.9799	0.306495	29.9999	1.188	250	1003.77
-30	32	58.8566	-94.112	308.4452	27.9799	0.060933	5.9661	0.993	250	971.32
-30	33	58.8392	-94.0932	151.2814	27.9799	0.044523	4.3594	1.018	250	991.75
-30	34	58.8184	-94.05	101.9825	27.9799	0.306495	30	1.03	250	998.23
-30	35	58.8174	-94.0523	113.1072	27.9799	0.306495	30	1.041	250	996.77
-30	36	58.8057	-94.0286	47.2061	27.9799	0.306495	29.9999	1.188	250	1005.49
-30	37	58.8192	-94.0546	56.1353	27.9799	0.216224	21.1614	1.123	250	1004.3
-30	38	58.8172	-94.0529	168.8228	27.9799	0.247632	24.2404	1.063	250	989.44
-30	39	58.8091	-94.0362	63.9958	27.9799	0.306495	29.9999	1.188	250	1003.25
-30	40	58.8041	-94.022	28.7479	27.9799	0.306495	29.9999	1.189	250	1007.95
-30	41	58.791	-93.9816	50.3259	27.9799	0.306495	29.9999	1.195	250	1005.08
-30	42	58.7976	-94.007	24.0905	27.9799	0.306495	29.9999	1.192	250	1008.57
-30	43	58.9017	-94.1179	396.4691	27.9799	0.019178	1.8778	0.986	250	960
-30	44	58.8209	-94.0562	145.6566	27.9799	0.153197	15	1.045	250	992.49
-30	45	58.8357	-94.0882	172.5677	27.9799	0.062674	6.1366	1.027	250	988.95
-30	46	58.8069	-94.0277	61.0487	27.9799	0.306495	29.9999	1.188	250	1003.65

Table 3. 8. STILT particle trajectory result. Each column of PARTICLE.DAT output has been matched to the VARSIWANT specified in SETUP.CFG. The figure shown here is only a sample of the first 30 mins (of 72 h) trajectory of 46 particles (of 3000), where: time=time, indx=index, lati=lat, long=lon, zagl=agl, zsfc=grdht, foot=foot, samt=sampt, dmas=dmass, mlht=zi, pres=pres.

The next step is to calculate the footprint, which represents the sensitivity of the receptor (tower) to surface fluxes. Put differently, the footprint of an atmospheric concentration measurement is its responsiveness to a unit emission in upwind source regions. The footprint is calculated using the STILT core function *Trajecfoot*. This is done by counting the number of particles in a surface-influenced region (defined as ½ of the estimated PBL height) and the time spent in the region. Therefore, the footprint provides an estimate of the fraction of observed short-term variability in mixing ratio at the tower that can be explained by localized fluxes. The unit of the calculated footprint is in ppm/μmol m^{-2} s^{-1}.

Subsequently, the footprint is multiplied by *a priori* fields of CO_2 surface fluxes from CarbonTracker-2013 to compute the associated contribution to the mixing ratio at the receptor. As previously explained, the CarbonTracker (CT) surface flux fields used in this study include biospheric fluxes, fossil fuel emissions, and wildfire sources. The extracted surface flux fields are converted to units of μmol m^{-2} s^{-1} prior to being multiplied by the footprint (ppm/μmol m^{-2} s^{-1}). Thus, the resulting model flux estimates are in ppm. To compare with observations, the mixing ratio enhancements due to surface fluxes must be added to a background concentration advected from the domain boundary. CarbonTracker-2013 3D fields of CO_2 were applied as background concentrations by taking the endpoints of the 3000 particle ensemble members and interpolating them to the corresponding grid cells (72 h backward in time) and their associated initial CO_2 concentrations. Particles that end over North American CT domains use the 1° x 1° dataset while particles falling outside use the global CT 3° x 2° grids. These concentration values at the trajectory endpoints are then simply advected to the receptor location, and an average CO_2 background concentration is calculated. Finally, the STILT simulation is completed by summing all the

different components (Biosphere, Fossil fuels, Wildfires, and Background CO_2 values) to derive the final CO_2 concentration at the measurement tower (i.e. receptor).

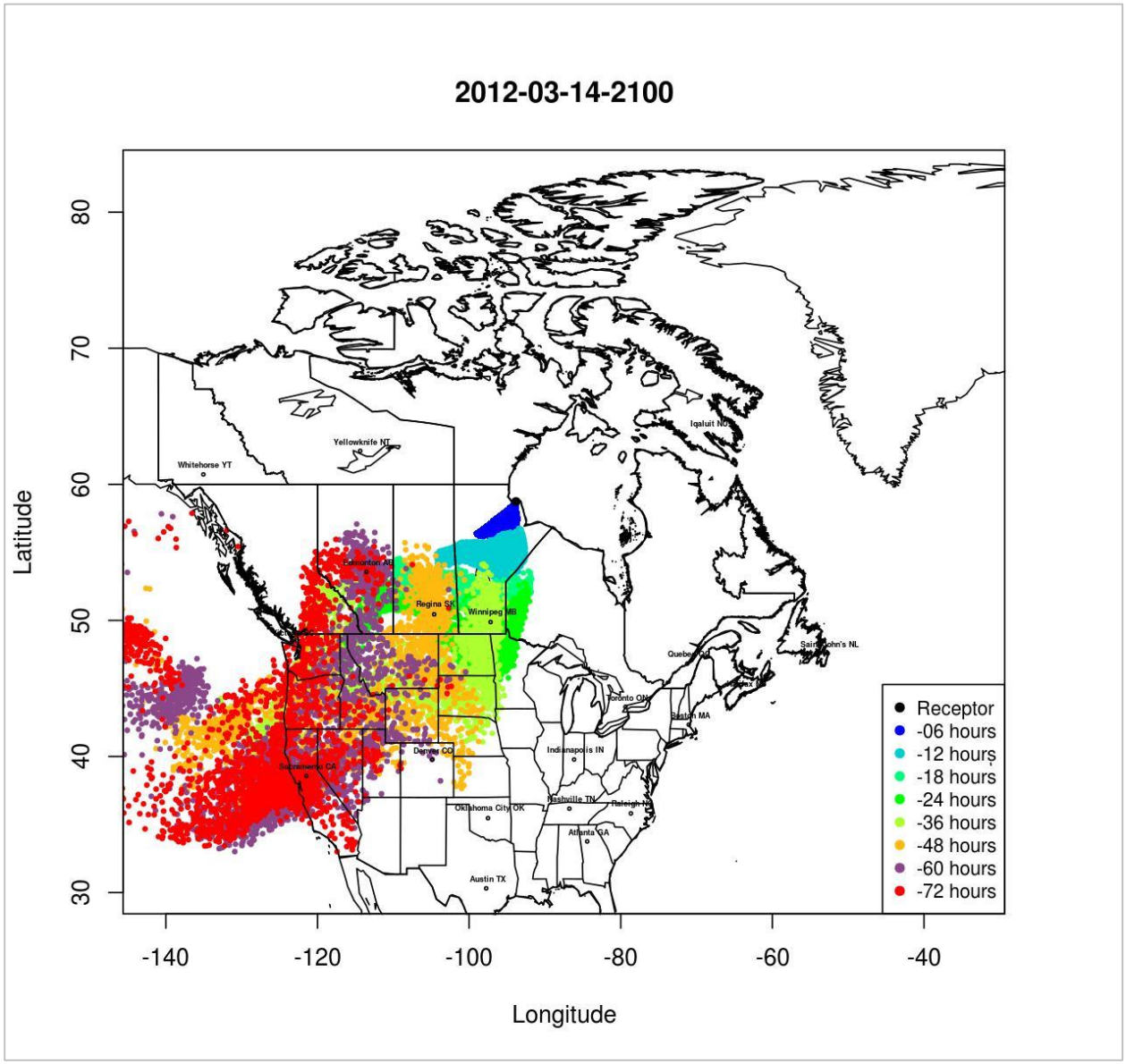

Figure 3. 20. STILT air particle trajectories map. The figure shown is for the Churchill 60 m tower site, on March 14, 2012, 21:00 UTC. Here, the STILT model transported 3000 particles backward in time over a 72 h period. The corresponding footprint map is shown in Figure 3. 22.

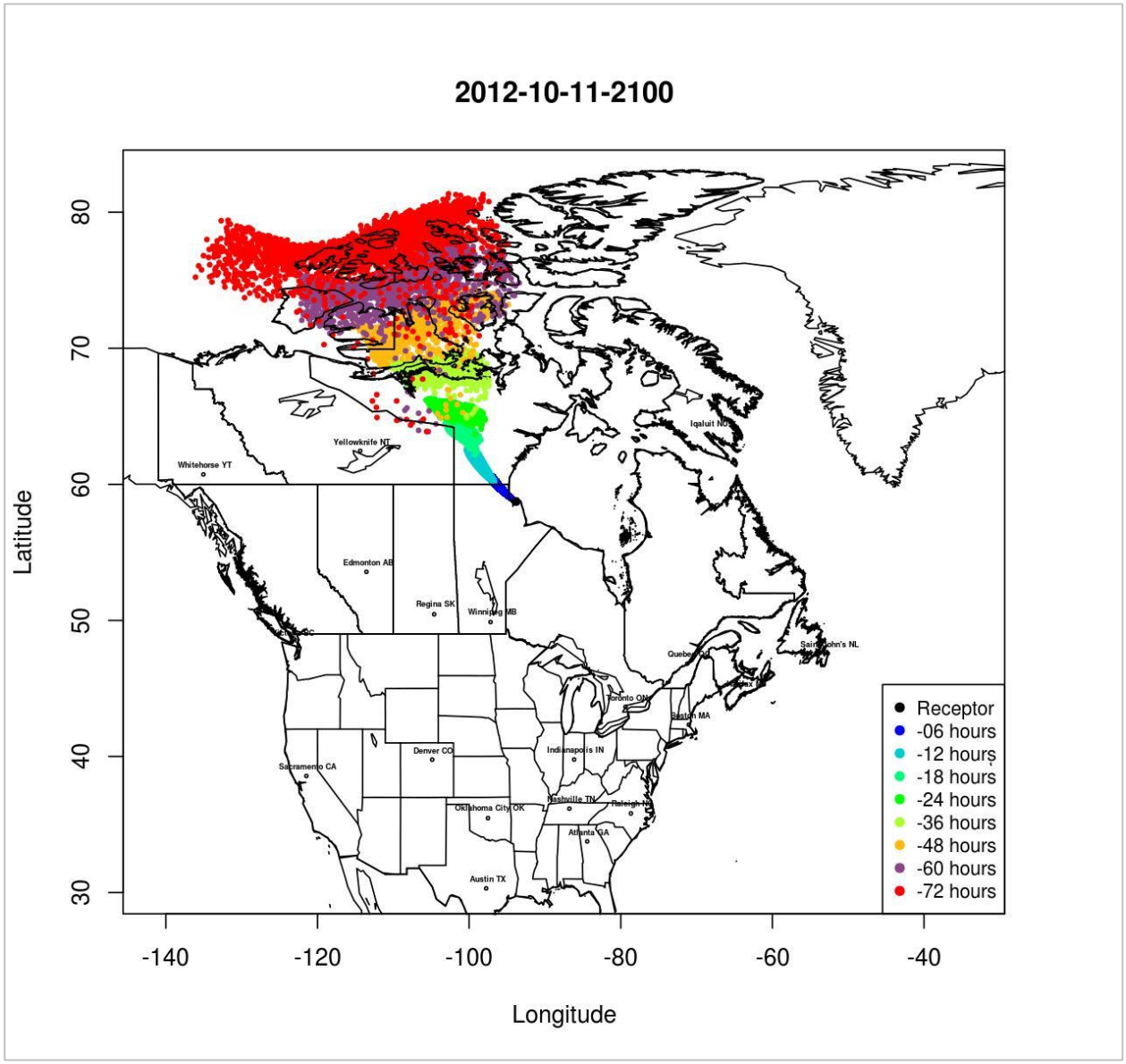

Figure 3. 21. STILT air particle trajectories map. The figure shown is for the Churchill 60 m tower site, on October 11, 2012, 21:00 UTC. Here, the STILT model transported 3000 particles backward in time over a 72 h period. The corresponding footprint map is shown in Figure 3. 23.

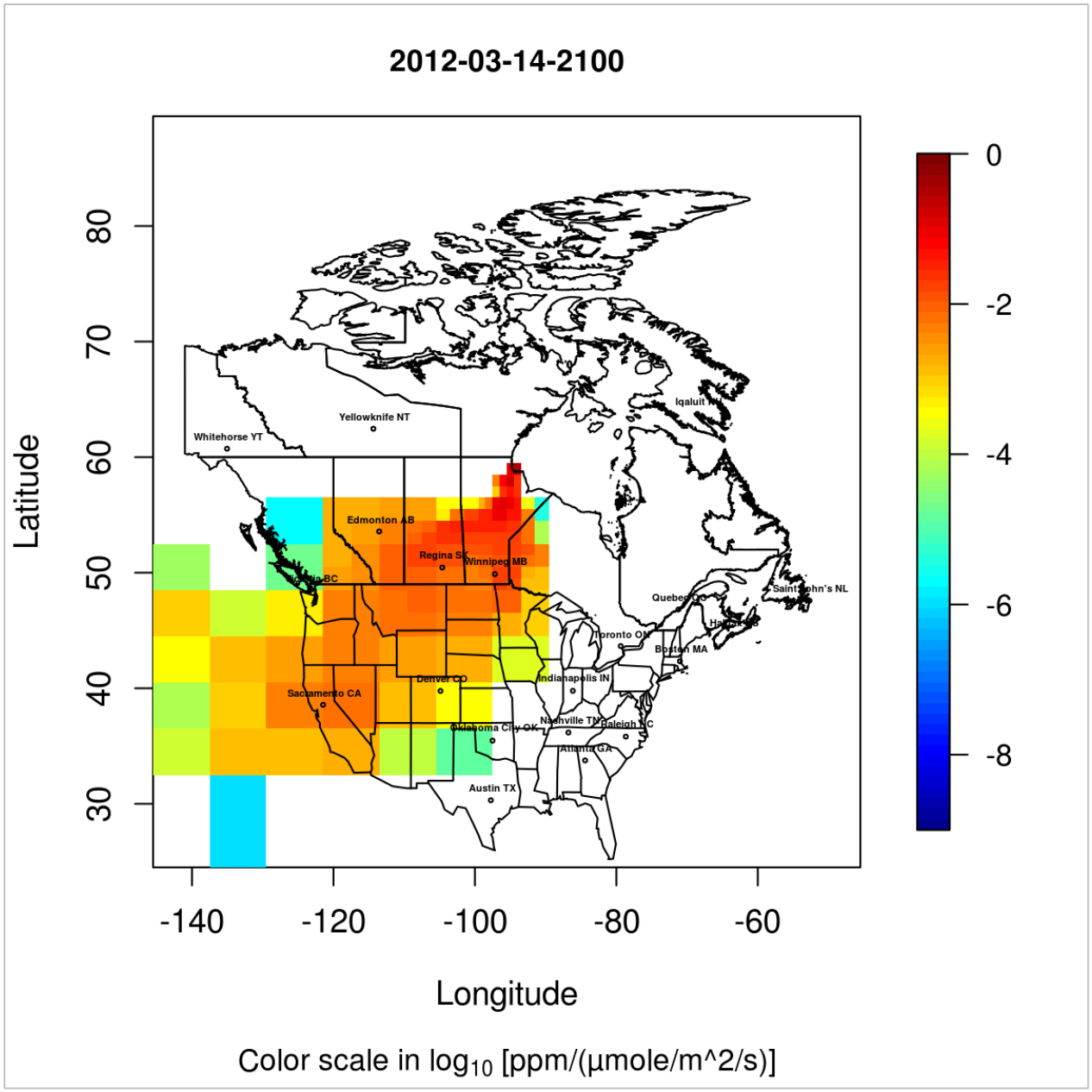

Figure 3. 22. STILT footprint map. The figure shown is for the Churchill 60 m tower site, on March 14, 2012, 21:00 UTC. The footprint represents the sensitivity of the mixing ratio at the measurement location to any given surface flux in upwind regions. It is derived from the locations and times of particles found close to the ground. This footprint links atmospheric observations to upwind fluxes, yielding the concentration change (ppm) for a unit surface flux (µmole/m^2/s).

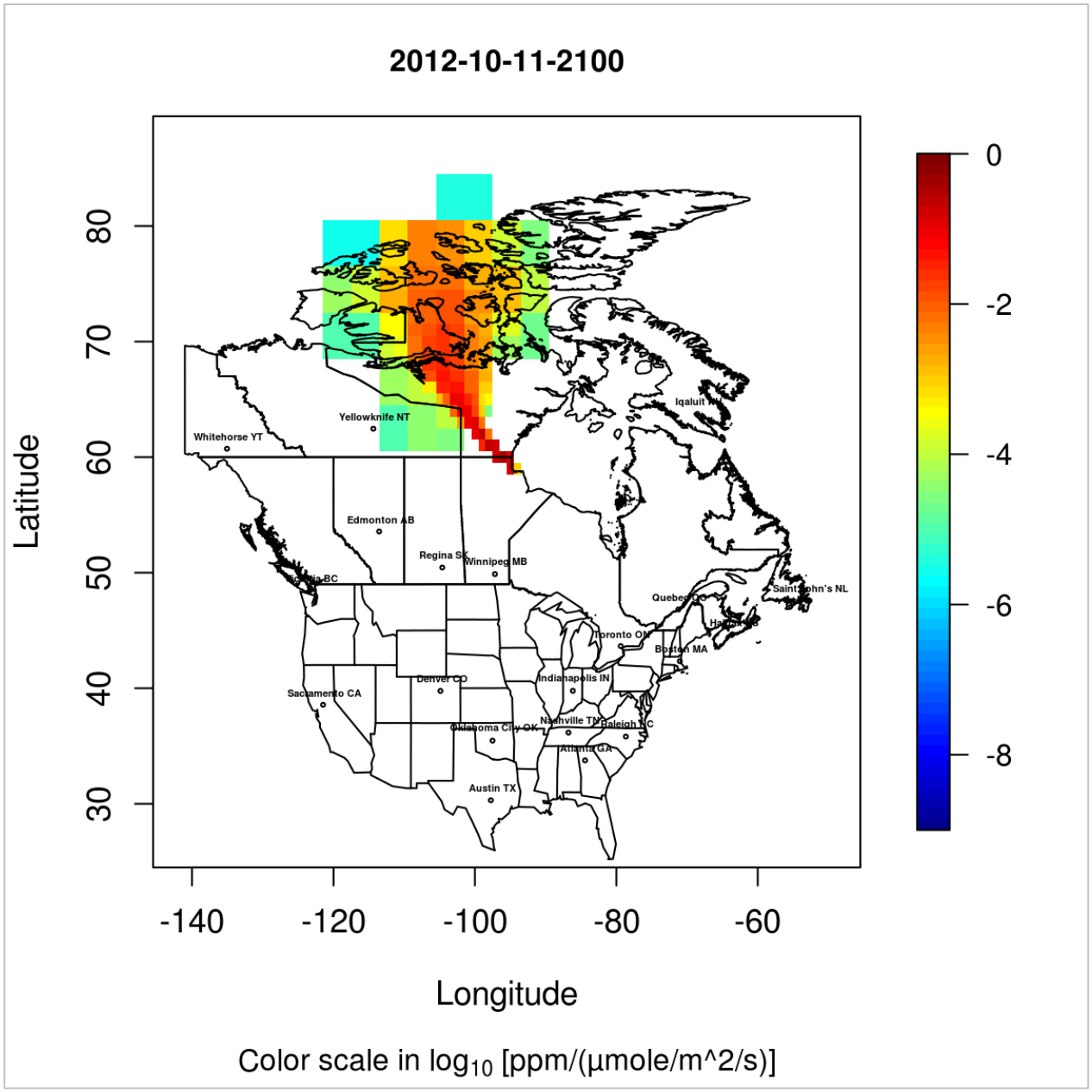

Figure 3. 23. STILT footprint map. The figure shown is for the Churchill 60 m tower site, on October 11, 2012, 21:00 UTC. The footprint represents the sensitivity of the mixing ratio at the measurement location to any given surface flux in upwind regions. It is derived from the locations and times of particles found close to the ground. This footprint links atmospheric observations to upwind fluxes, yielding the concentration change (ppm) for a unit surface flux (µmole/m^2/s).

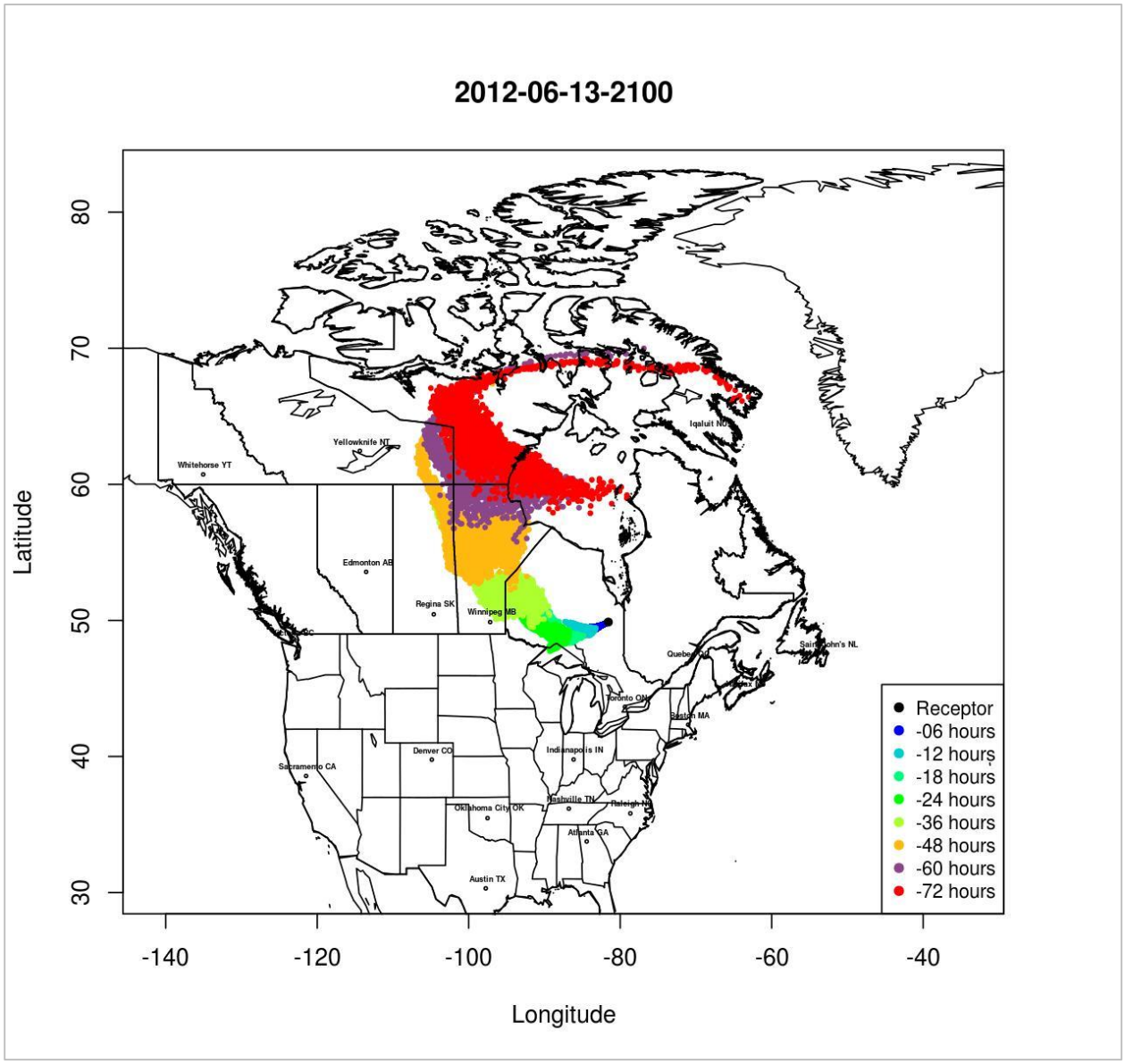

Figure 3. 24. STILT air particle trajectories map. The figure shown is for the Fraserdale 40 m tower site, on June 13, 2012, 21:00 UTC. Here, the STILT model transported 3000 particles backward in time over a 72 h period. The corresponding footprint map is shown in Figure 3. 26.

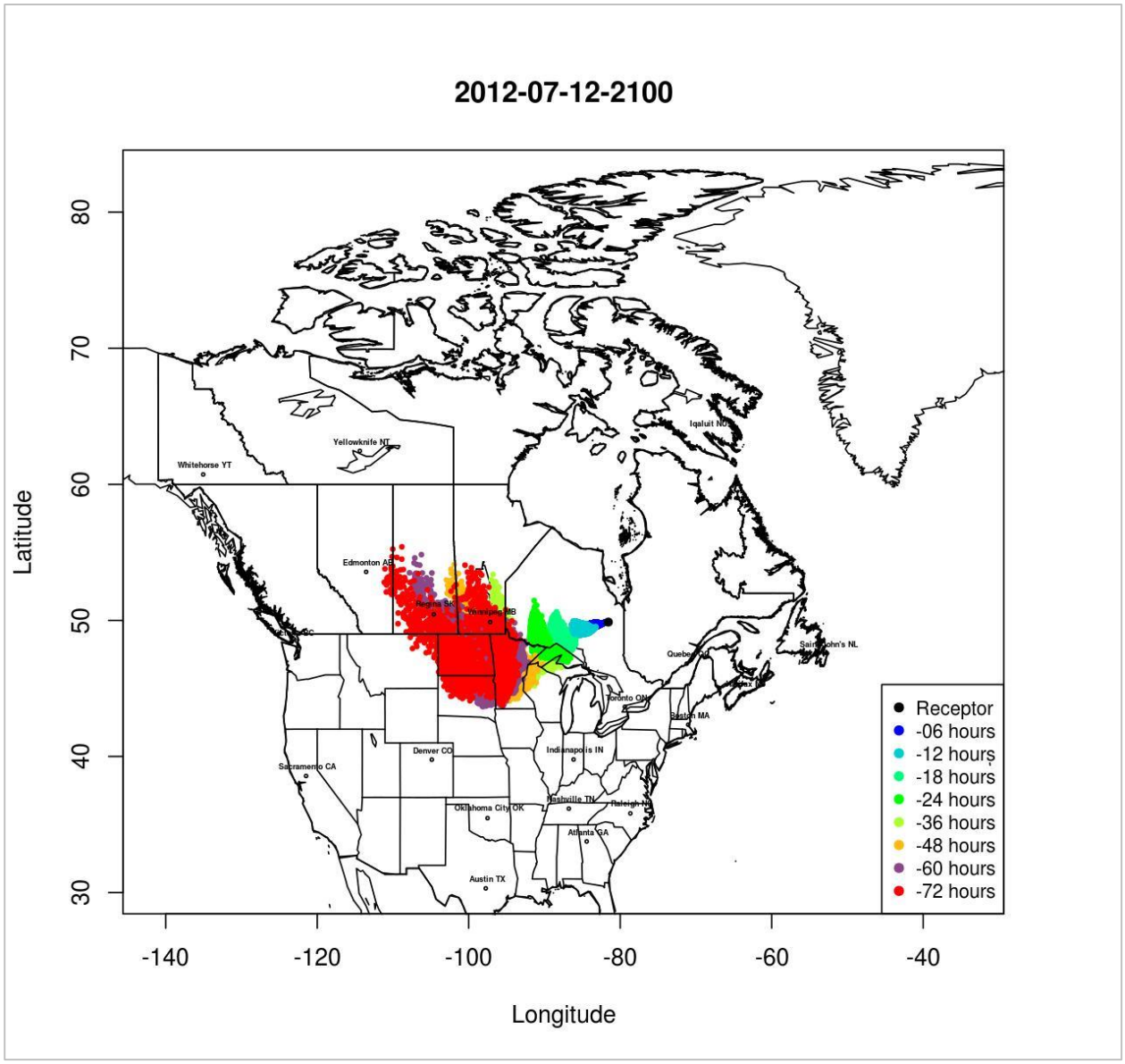

Figure 3. 25. STILT air particle trajectories map. The figure shown is for the Fraserdale 40 m tower site, on July 12, 2012, 21:00 UTC. Here, the STILT model transported 3000 particles backward in time over a 72 h period. The corresponding footprint map is shown in Figure 3. 27.

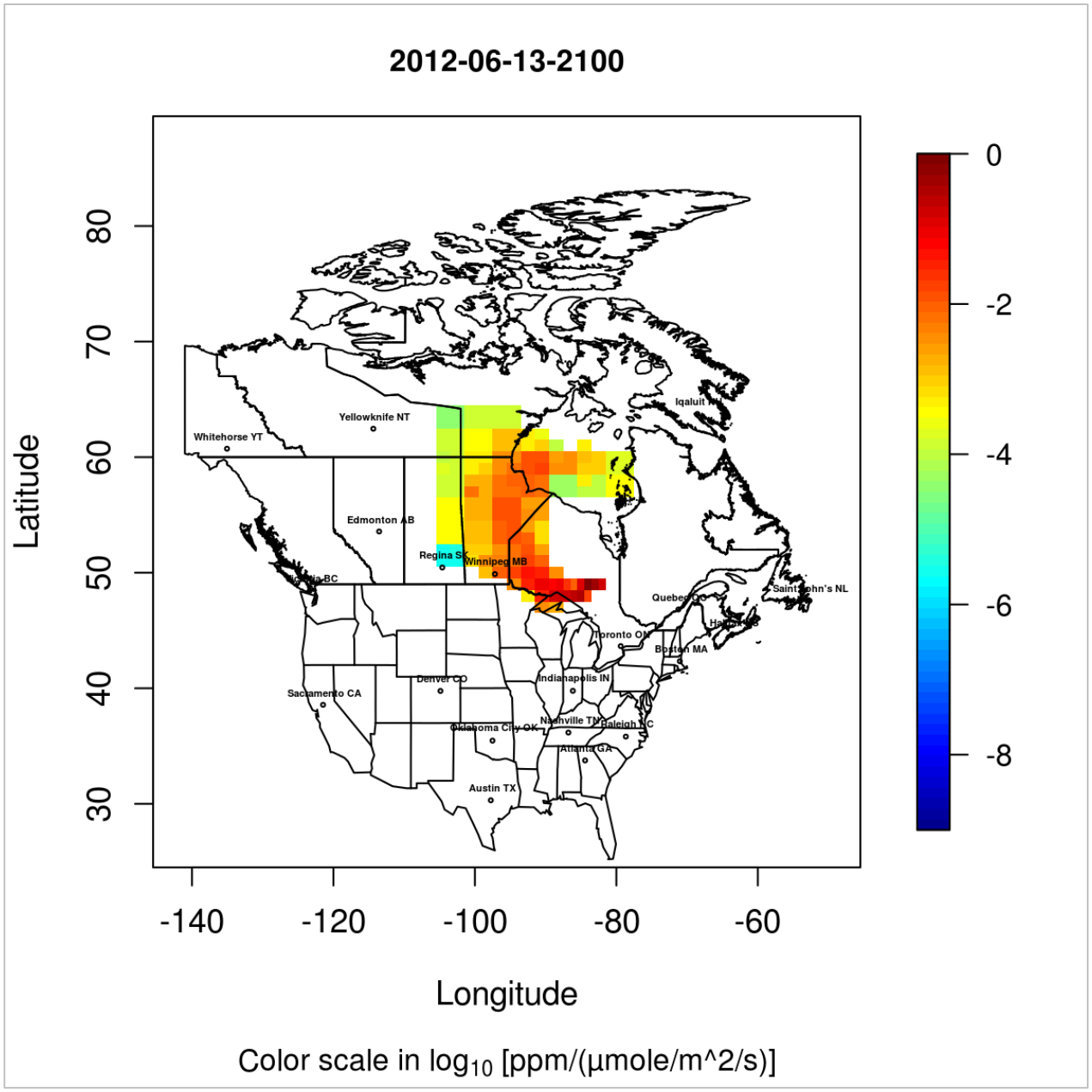

Figure 3. 26. STILT footprint map. The figure shown is for the Fraserdale 40 m tower site, on June 13, 2012, 21:00 UTC. The footprint represents the sensitivity of the mixing ratio at the measurement location to any given surface flux in upwind regions. It is derived from the locations and times of particles found close to the ground. This footprint links atmospheric observations to upwind fluxes, yielding the concentration change (ppm) for a unit surface flux (µmole/m²/s).

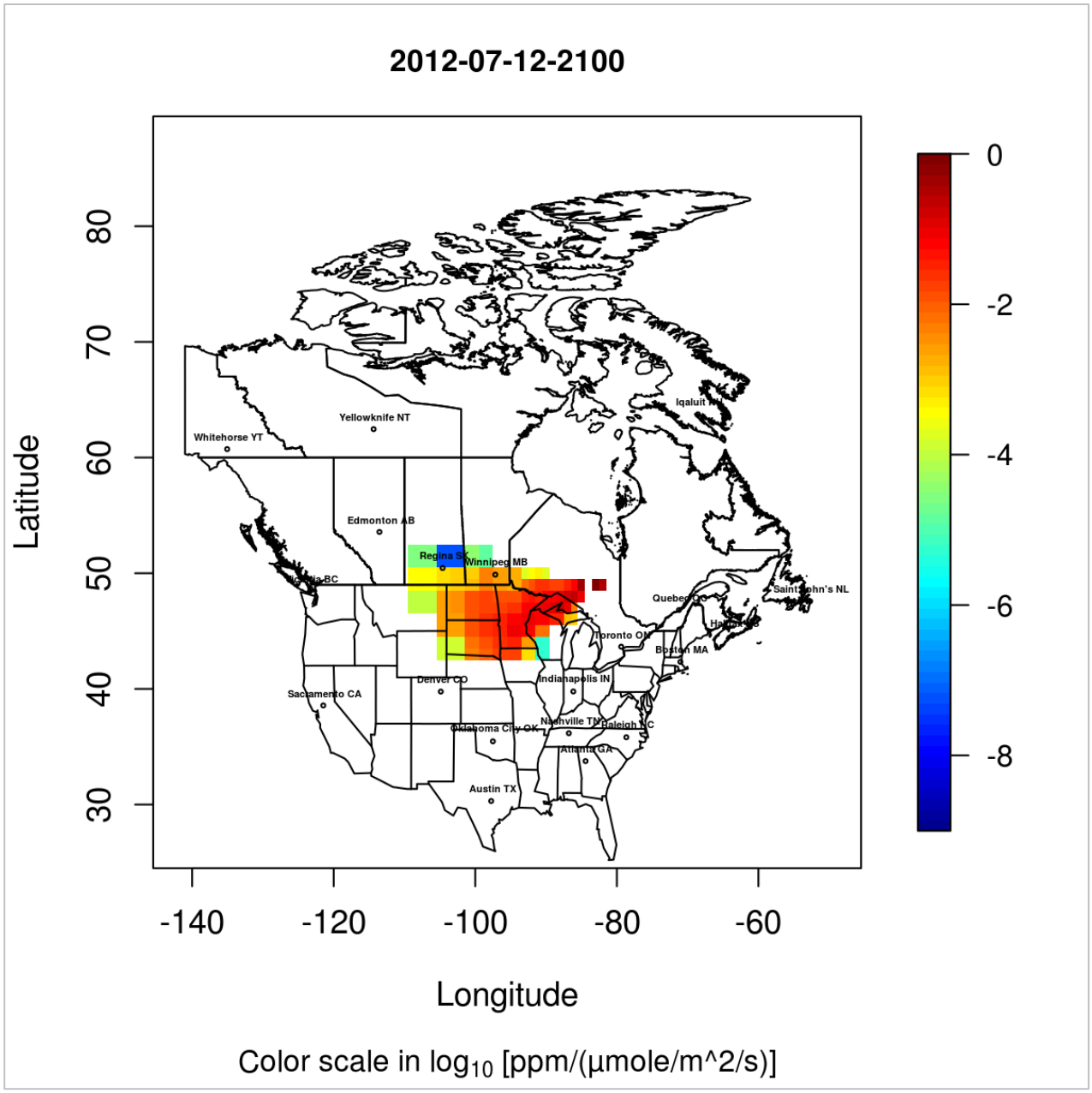

Figure 3. 27. STILT footprint map. The figure shown is for the Fraserdale 40 m tower site, on July 12, 2012, 21:00 UTC. The footprint represents the sensitivity of the mixing ratio at the measurement location to any given surface flux in upwind regions. It is derived from the locations and times of particles found close to the ground. This footprint links atmospheric observations to upwind fluxes, yielding the concentration change (ppm) for a unit surface flux (µmole/m^2/s).

3.4 Model Sensitivity Analysis

3.4.1 Sensitivity of STILT Simulations to Particle Number

The STILT model simulates backward trajectories as an ensemble to account for random air turbulence. Ideally, an extremely large number of air particles are required to represent the ensemble properties of model transport. This is because an insufficient number of particles could lead to incomplete sampling of air parcel trajectories and surface fluxes. Consequently, modelled atmospheric concentrations tend to fluctuate depending on the size of the particle ensemble, and typically, the fluctuation is inversely proportional to the particle number. This is the so-called "sampling error" or the "statistical variance", which is defined as the error due to the stochastic nature of the transport model (Gerbig et al., 2003; Mallia et al., 2014). However, model run time increases proportionally to the number of simulated air particles thereby requiring additional computational resources. Thus, in order to simultaneously minimize the model run time and the sampling error, a sensitivity analysis was performed.

Keeping all other model parameters constant (e.g. duration of backward simulation = -72 hours), particle number was varied between 100 and 5000, and the model was run 100 times for each ensemble size on July 15, 2012 at 2100UTC. This particular day was chosen due to the substantial biospheric contributions (about -14 ppm) toward CO_2 mixing ratios at that time. To quantify the sensitivity of the STILT model, and assess the magnitude of CO_2 fluctuations, the standard deviation of the simulated concentrations was calculated for each ensemble size (Figure 3.28). The result shows that model fluctuations decreased as the particle number increased, with the standard deviation varying from 1.05 ppm to 0.20 ppm for 100 particles and 5000 particles

respectively ($p < 0.05$, Table 3.9). Also, the result demonstrates that the model is most sensitive to biospheric flux contributions, and that the variations in modelled total CO_2 are mainly due to fluctuations in the sampled upwind (vegetative) influence regions. This is expected because CO_2 emission/sink from the biosphere is the most important surface flux contribution to the observed mixing ratios in the Churchill area. On the other hand, simulated contributions from fossil fuel and wildfire sources were largely unresponsive to ensemble size. In addition, very limited sensitivity was observed in the background concentrations, probably due to its smaller spatial variability and the well-dispersed STILT particles at the end of the 72 h simulation (Mallia et al., 2014). Following the sensitivity analysis described above, an ensemble size of 3000 was chosen since it appears to be the most reasonable particle number to both minimize sampling error and model run time.

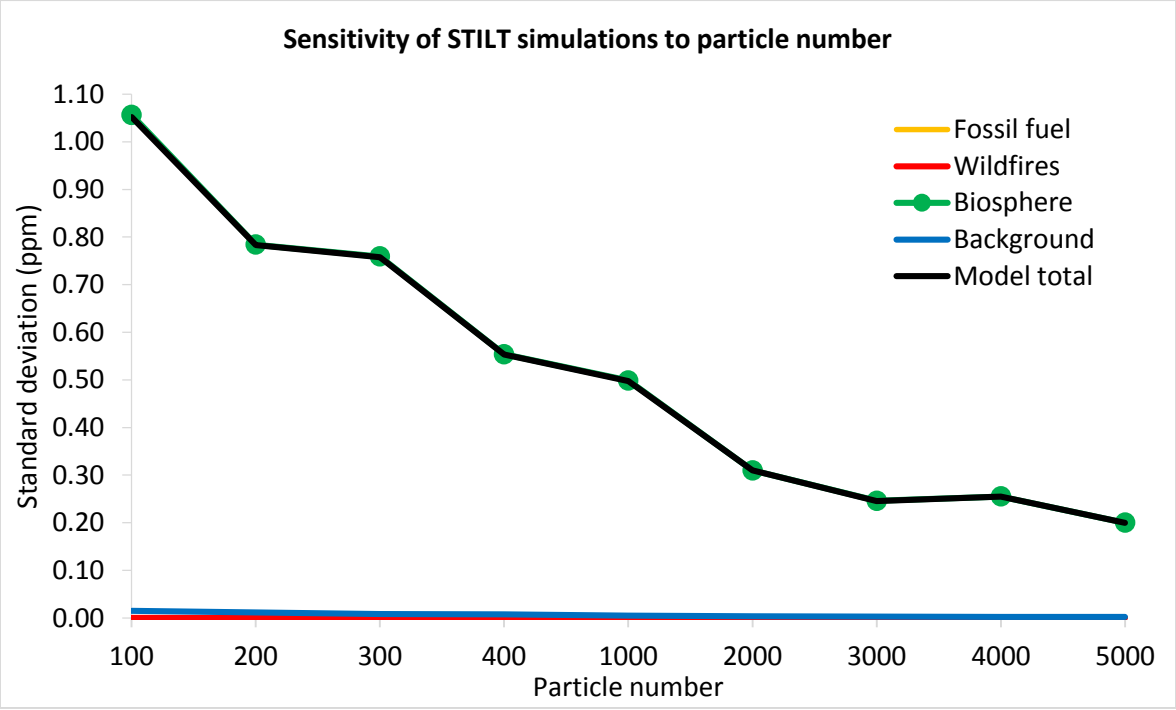

Figure 3. 28. Fluctuations in STILT-modelled CO_2 concentrations as a function of particle number. For each particle ensemble size, the standard deviation of 100 different STILT runs is calculated. Results for the different components of the simulated atmospheric CO_2 concentrations are shown as fossil fuel, wildfires, biosphere, background, and model total. This run is for July 15, 2012, 2100UTC, at Churchill.

F-Test Two-Sample for Variances		
	100 Particles	*5000 Particles*
Mean	376.5746611	376.7953644
Variance	1.106747707	0.039972706
Observations	100	100
df	99	99
F	27.68758535	
P(F<=f) one-tail	3.28163E-45	
F Critical one-tail	1.394061257	

Table 3. 9. Statistical test to determine whether the variability in STILT-modelled CO_2 concentrations as a function of particle number is statistically significant. The null hypothesis is that there is no significant difference between the variances of the two samples. The alternative hypothesis is that fluctuations in STILT-modelled CO_2 concentrations were stronger when using smaller particle ensemble sizes than larger sizes. Since the p-value of the test is < 0.05, the null hypothesis is rejected.

3.4.2 Sensitivity of STILT Simulations to Duration of Backward Trajectory

A second test was conducted to determine how STILT simulations would respond to changes in the duration of the backward runs. It was anticipated that model fluctuations would decrease as the number of hours increased, since air parcel trajectories would be more adequately represented in longer backward simulations, and the particles would have been highly dispersed over a larger surface influence region in upwind locations. This should be particularly important in a continental tower measurement site such as Churchill where the integrated signal of CO_2 exchange represents footprint areas of up to 10^4 km^2 (Lin et al., 2003). Therefore, in an attempt to assess the magnitude of CO_2 fluctuations with trajectory duration, a sensitivity analysis was carried out. Here, all other model parameters are held constant (e.g. number of particles = 2000), while number of hours for the backward simulation was varied between 24 h and 120 h. Again, 100 STILT simulations for CO_2 concentration at Churchill were run for each given duration on July 15, 2012 at 2100UTC, and the standard deviation was calculated. Figure 3.29 shows the result of

this sensitivity test. It is important to note that unlike particle ensemble size, model simulations show very limited sensitivity to the duration of backward trajectory, even for biospheric contributions; the model fluctuation was merely 0.03 ppm ($p > 0.05$, Table 3.10). For the purpose of this study, the 72 h time period was chosen for all backward trajectories, since it had the lowest standard deviation (though marginally). Also, using 72 h instead of 120 h helps to maximize computation resources and time.

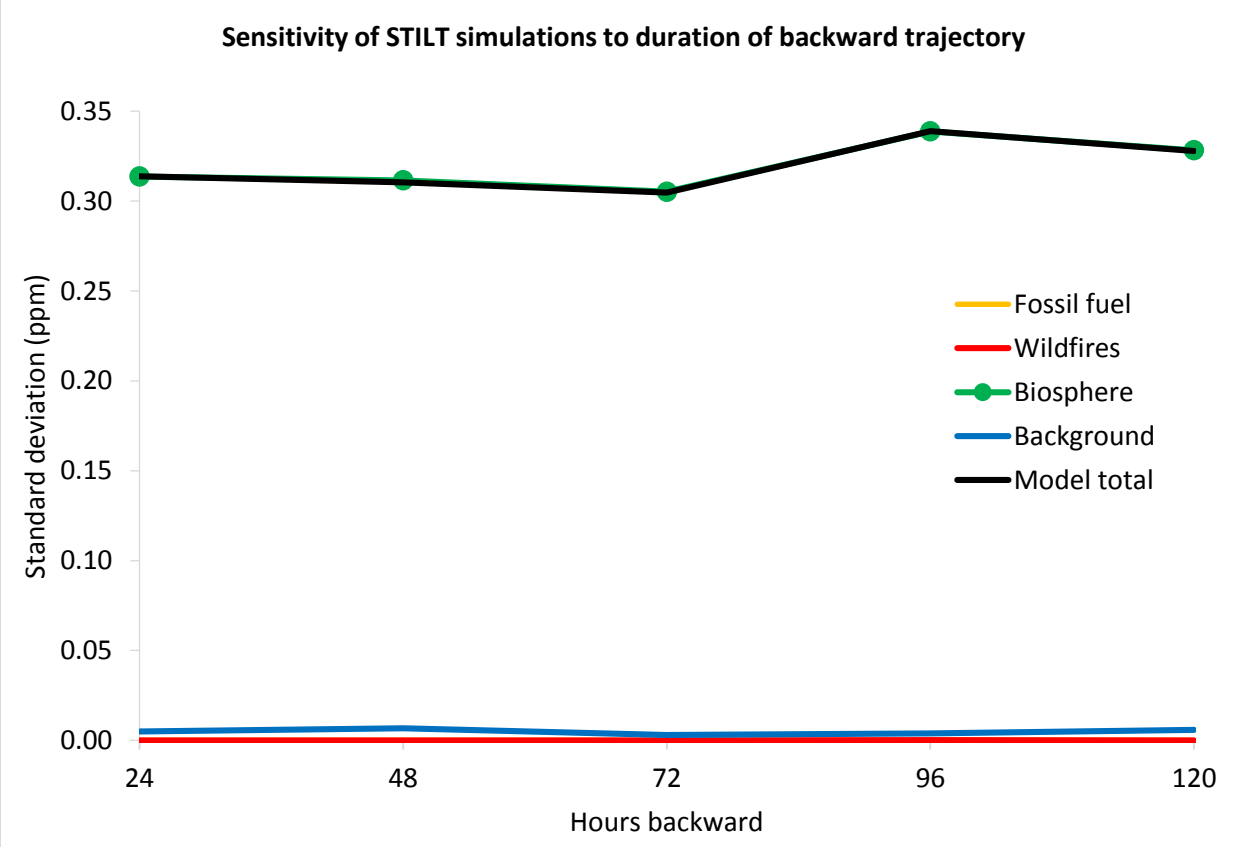

Figure 3. 29. Fluctuations in STILT-modelled CO_2 concentrations as a function of trajectory duration. For each length of time, the standard deviation of 100 different STILT runs is calculated. Results for the different components of the simulated atmospheric CO_2 concentrations are shown as fossil fuel, wildfires, biosphere, background, and model total. This run is for July 15, 2012, 2100UTC, at Churchill.

F-Test Two-Sample for Variances		
	120 Hours	*24 Hours*
Mean	376.7184912	376.6883033
Variance	0.107501119	0.098458476
Observations	100	100
df	99	99
F	1.091842204	
P(F<=f) one-tail	0.331433865	
F Critical one-tail	1.394061257	

Table 3. 10. Statistical test to determine whether the variability in STILT-modelled CO_2 concentrations as a function of trajectory duration is statistically significant. The null hypothesis is that there is no significant difference between the variances of the two samples. The alternative hypothesis is that fluctuations in STILT-modelled CO_2 concentrations were stronger over shorter time periods. Since the p-value of the test is > 0.05, the null hypothesis is accepted.

4.0 MEASUREMENT OF ATMOSPHERIC CONCENTRATION OF CO_2 IN THE HUDSON BAY LOWLANDS: AN APPLICATION OF A LAGRANGIAN PARTICLE DISPERSION MODEL

4.1 Preliminary Analysis

4.1.1 Seasonal and Interannual Variations

Figure 4.1 and 4.2 show weekly flask CO_2 concentration values (2008–2012) for Churchill and Fraserdale. The seasonal cycle is an indication of biospheric flux contributions to the observed CO_2 mixing ratios in the region. Carbon uptake by vegetation during the growing season is responsible for the summer minimum CO_2 values, while wintertime is characterized by higher atmospheric CO_2 concentrations due to little/no terrestrial carbon sink. A comparison between concentration values at the two towers reflects a stronger vegetative influence at Fraserdale. (Figure 4.3). This is evident in the relatively lower summertime CO_2 values at Fraserdale. Additionally, in Figure 4.4 and 4.5 morning (09:00 UTC) and afternoon (21:00 UTC) CO_2 concentrations are differentiated to reveal the relative influence of biological activities on atmospheric CO_2 concentrations in the two regions. In an environment where anthropogenic and wildfire carbon sources are negligible, vegetative respiration and photosynthesis play an important role in atmospheric CO_2 changes. Characteristically, there is a net CO_2 uptake during the day, and net release at night. The drawdown in CO_2 by plant photosynthesis results in a decrease in atmospheric CO_2 content during the daytime, while autotrophic respiration at night increases CO_2 in the atmosphere. Also, at any given time, the magnitude of this terrestrial influence is controlled

by the rate of biological activities, which varies spatially. It is expected that regions with more vegetation will have higher rates of photosynthesis and respiration, and therefore, produce stronger CO_2 fluxes. The Fraserdale data (Figure 4.4) show a stronger variability ($p < 0.05$) in morning and afternoon CO_2 values with a mean concentration of 392.86 ± 8.97 ppm compared to 390.76 ± 7.20 ppm at Churchill (Table 4.1). To eliminate the contribution of diurnal bias on seasonal and interannual timescales, afternoon data for Fraserdale and Churchill are compared in Figure 4.6. The maximum regional representation of biological activities around the two sites can be distinguished using this approach. Atmospheric CO_2 concentration reaches a minimum value of 367 ppm and 370 ppm at Fraserdale and Churchill respectively. Furthermore, the mean afternoon CO_2 concentration in summer (June – September) is 380 ppm at Fraserdale compared to 384 ppm at Churchill ($p < 0.05$, Table 4. 2). This difference in atmospheric CO_2 concentration over the two sites can be explained in terms of their vegetation characteristics, which are also constrained by the climate. Lower atmospheric CO_2 values at Fraserdale, particularly during summer afternoons, reflect the presence of more plant growth around the area. The measurement site at Fraserdale is located in a boreal forest region consisting predominantly of black spruce (Picea mariana), Jack pine (Pinus banksiana), and aspen (Populus tremuloides). Conversely, Churchill is in a region of tundra and boreal forest transition. The main features of the vegetation are dwarf birch, sedges, grasses, mosses, and lichens, with patches of stunted black spruce and tamarack. The higher atmospheric CO_2 concentrations at the Churchill site are due to lower carbon uptake over the region.

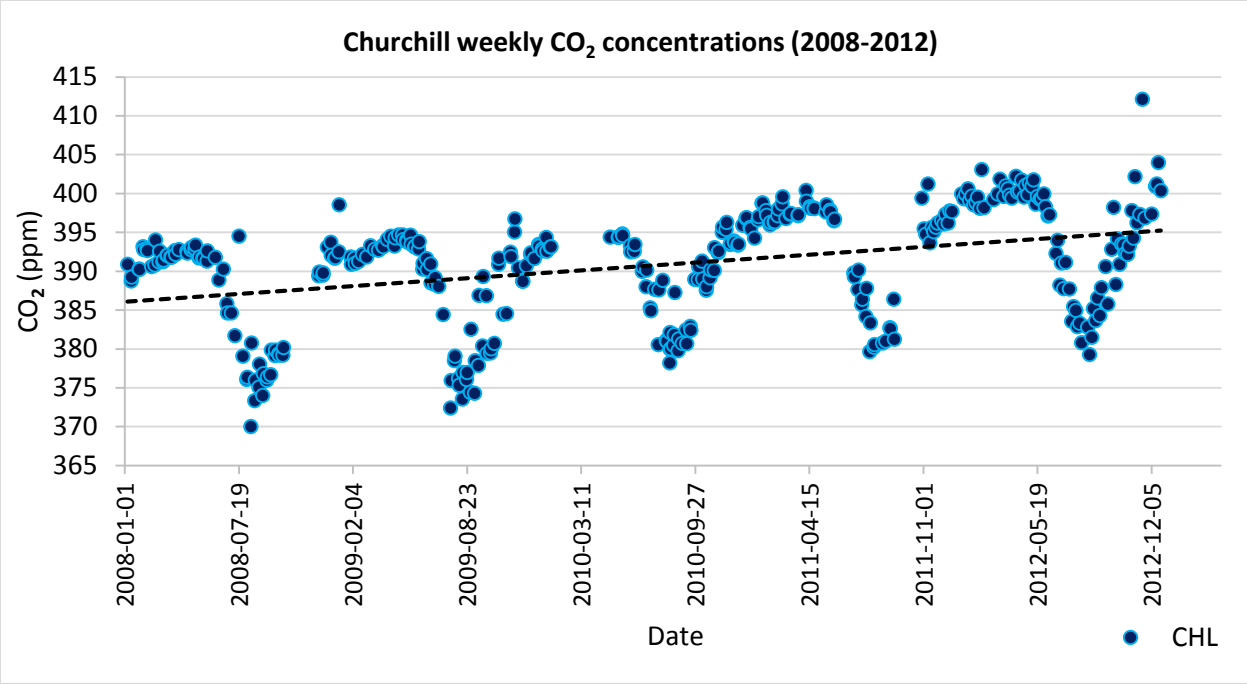

Figure 4. 1. Weekly CO_2 concentrations from 2008 – 2012, measured at the top of a 60 m tower in Churchill Manitoba.

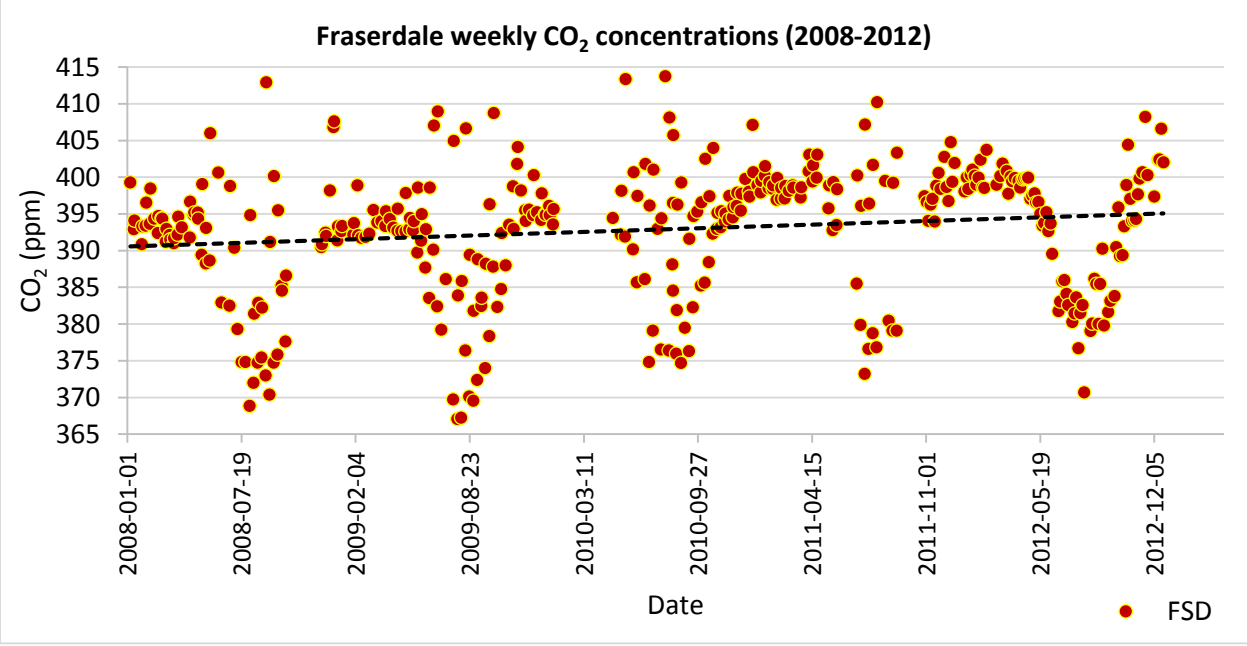

Figure 4. 2. Weekly CO_2 concentrations from 2008 – 2012, measured at the top of a 40 m tower in Fraserdale Ontario.

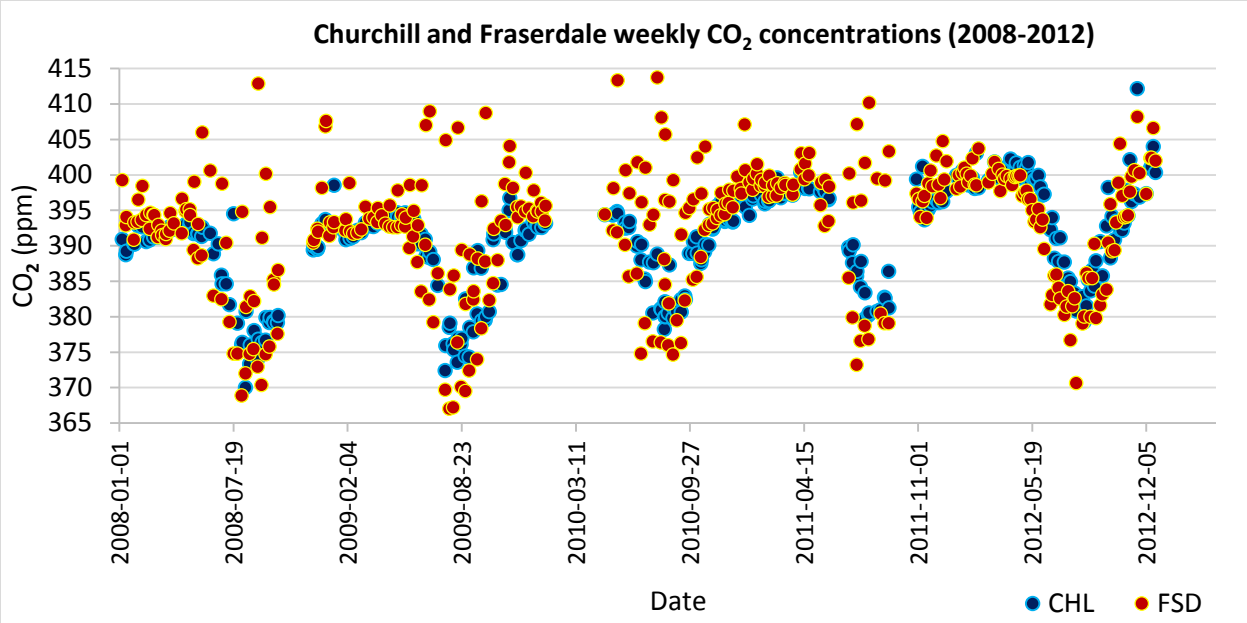

Figure 4. 3. Churchill vs Fraserdale weekly CO_2 concentrations from 2008 – 2012.

F-Test Two-Sample for Variances		
	FSD CO_2	*CHL CO_2*
Mean	392.860542	390.762439
Variance	80.45274807	51.79365219
Observations	369	369
df	368	368
F	1.553332207	
P(F<=f) one-tail	**1.30853E-05**	
F Critical one-tail	1.187332995	

Table 4. 1. Variability in morning and afternoon CO_2 values for Churchill and Fraserdale. The null hypothesis is that there is no statistically significant difference in the variability in diurnal CO_2 concentrations between Churchill and Fraserdale; while the alternative hypothesis is that at Fraserdale, atmospheric CO_2 values vary significantly between morning and afternoon periods, and this variability is statistically stronger than that at Churchill. Since the p-value is <0.05, the null hypothesis is rejected.

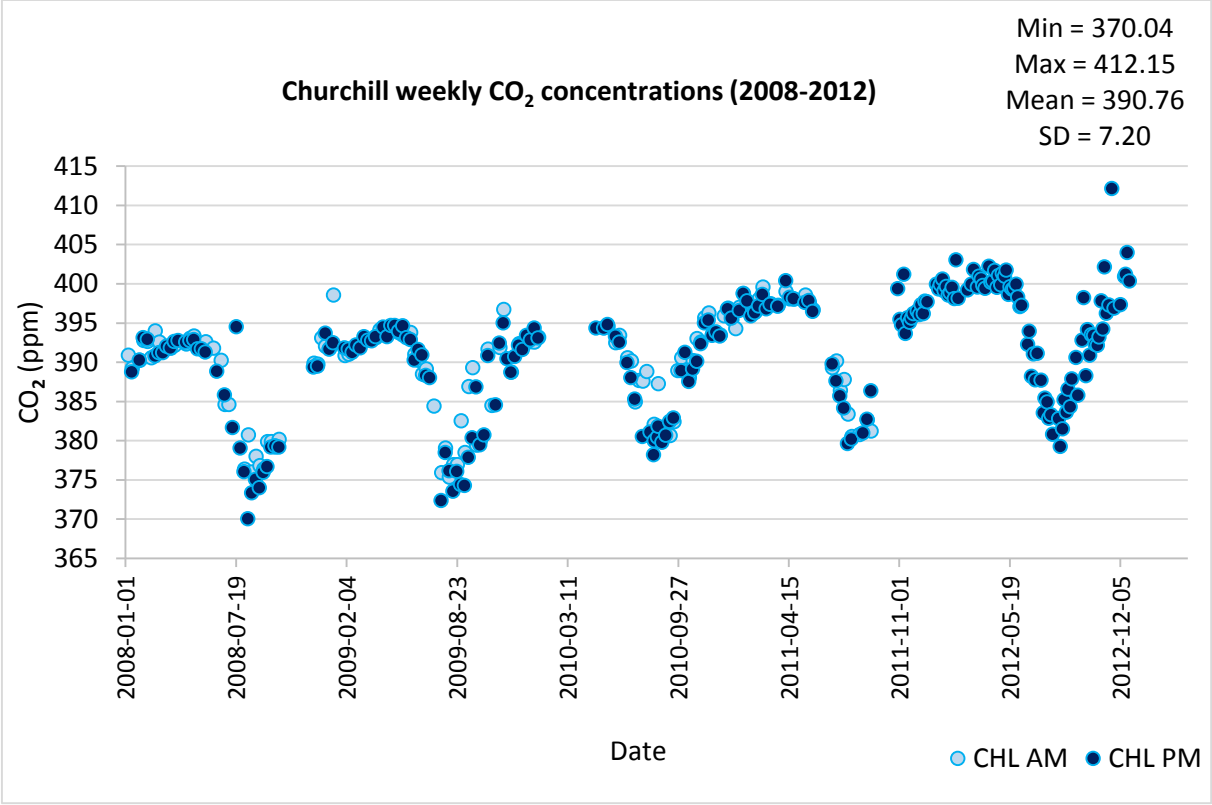

Figure 4. 4. Comparison between morning (9:00 UTC) and afternoon (21:00 UTC) CO_2 concentrations at Churchill Manitoba.

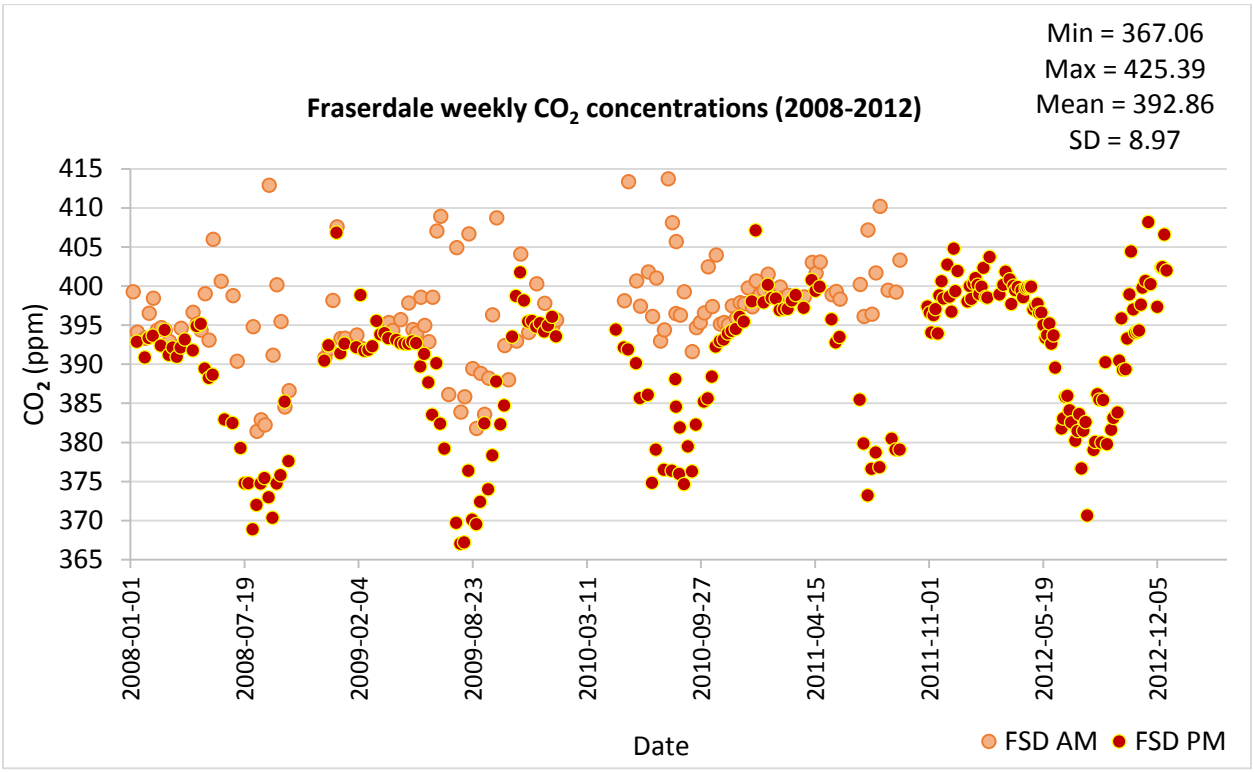

Figure 4. 5. Comparison between morning (9:00 UTC) and afternoon (21:00 UTC) CO_2 concentrations at Fraserdale Ontario.

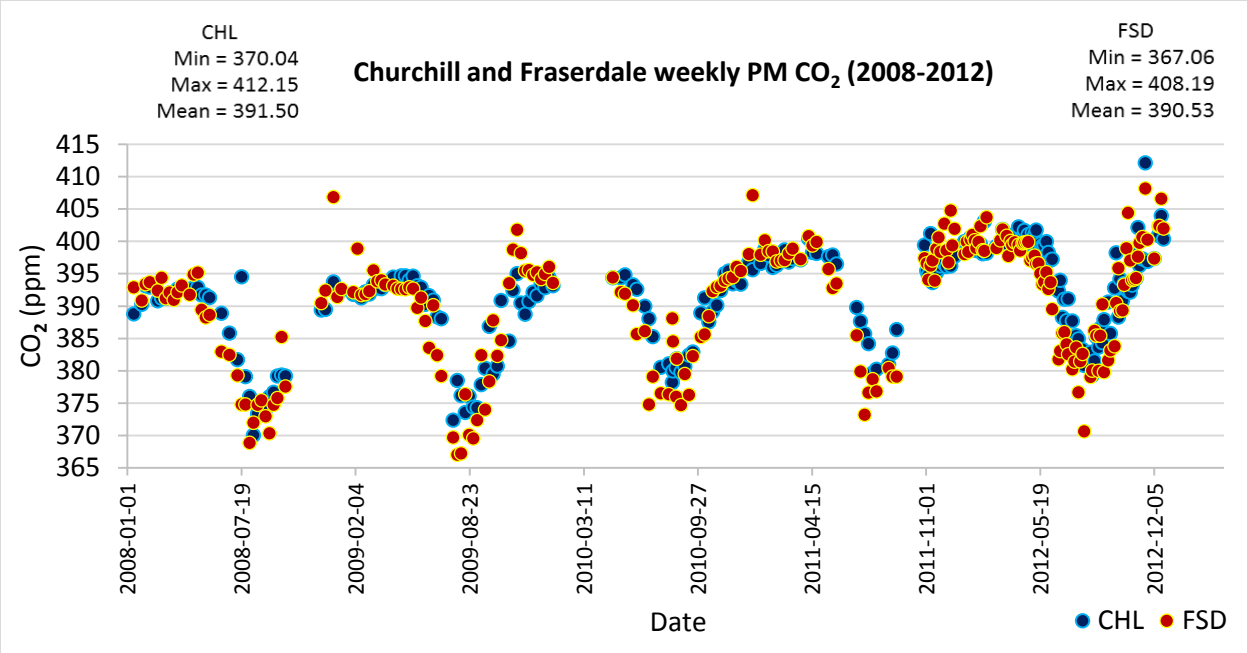

Figure 4. 6. Churchill vs Fraserdale weekly CO_2 concentrations from 2008 – 2012, afternoon values only. This eliminates the contribution of diurnal bias on seasonal and interannual timescales.

t-Test: Two-Sample Assuming Unequal Variances		
	CHL CO_2	*FSD CO_2*
Mean	384.0590123	379.9675309
Variance	42.48160651	36.83737883
Observations	81	81
Hypothesized Mean Difference	0	
df	159	
t Stat	4.134609749	
P(T<=t) one-tail	2.87018E-05	
t Critical one-tail	1.654493503	
P(T<=t) two-tail	**0.00005740**	
t Critical two-tail	1.974996213	

Table 4. 2. Statistical test of mean afternoon CO_2 concentration in summer (June – September) between Churchill and Fraserdale. The null hypothesis is that there is no statistically significant difference in the means of the two sites. The alternative hypothesis is that the mean afternoon CO_2 concentration in summer is higher at Churchill compared to Fraserdale, and that this difference is statistically significant. Since the p-value is <0.05, the null hypothesis is rejected.

Figure 4.7 shows the 2008–2012 mean seasonal cycle obtained for Fraserdale and Churchill. The amplitude of the seasonal cycle is about 22 ppm and 19 ppm at Fraserdale and Churchill respectively, indicating a stronger influence of vegetative activities at Fraserdale. Between January and March when respiration exceeds photosynthesis, CO_2 concentrations are higher at Fraserdale (about 2 ppm greater than Churchill). Also, an earlier CO_2 uptake in mid-April is evident at Fraserdale compared to mid-May at Churchill. In July, CO_2 uptake by vegetation is on the order of 5 ppm more at Fraserdale than Churchill. Atmospheric CO_2 concentration remains relatively lower at Fraserdale throughout the summer months with a seasonal minimum in early August, compared to mid-August at Churchill. Moreover, the faster rate of increase of CO_2 at Fraserdale after the seasonal minimum, and subsequently, higher atmospheric CO_2 values beginning in early October demonstrate a rapid response to the growing dominance of autotrophic respiration over photosynthetic activity around the Fraserdale site. Throughout the non-growing season, CO_2 concentrations remain relatively higher at Fraserdale reaching a seasonal maximum of about 8 ppm in December compared to 4 ppm at Churchill (Table 4.3).

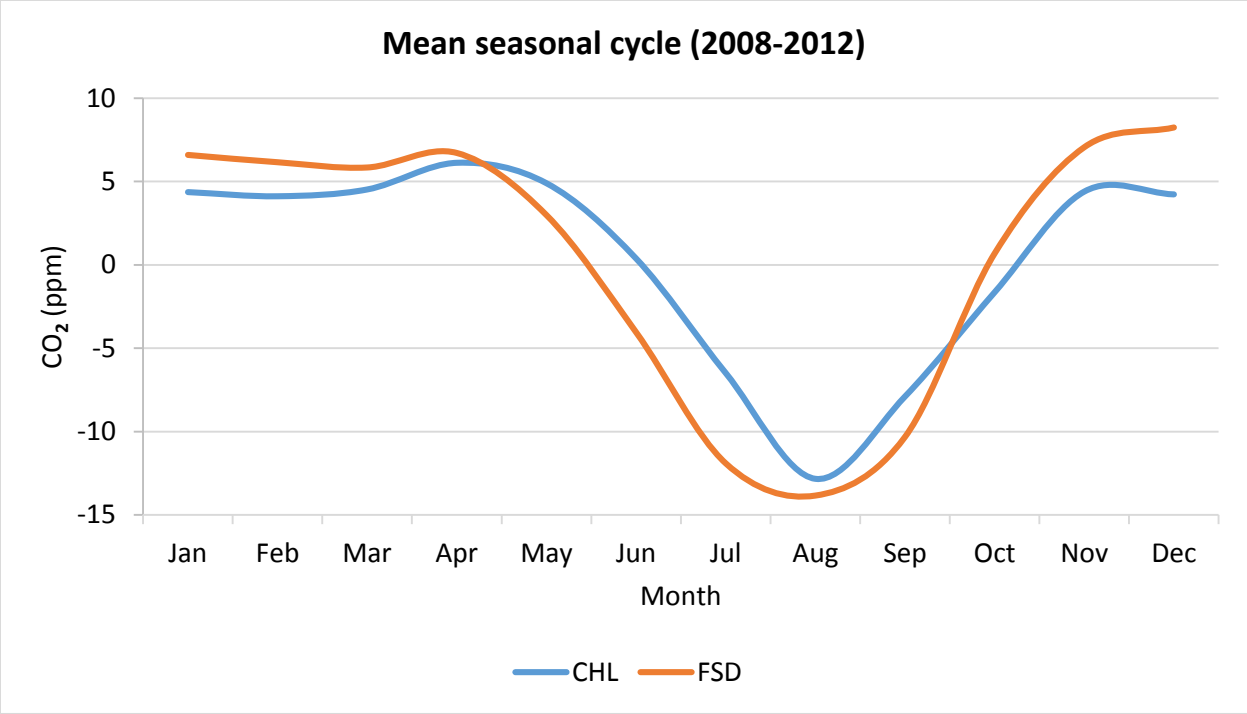

Figure 4. 7. Mean seasonal cycle calculated for Churchill and Fraserdale from 2008–2012. The vital statistics of the graph are highlighted in the table below.

Month	CHL Mean Seasonal Cycle	FSD Mean Seasonal Cycle	Diff
Jan	4.36	6.59	2.23
Feb	4.11	6.15	2.04
Mar	4.52	5.84	1.31
Apr	6.12	6.71	0.59
May	4.89	2.98	-1.91
Jun	0.38	-4.05	-4.42
Jul	-6.49	-11.91	-5.41
Aug	-12.83	-13.84	-1.00
Sep	-7.90	-10.32	-2.42
Oct	-1.64	0.68	2.33
Nov	4.39	7.05	2.66
Dec	4.23	8.24	4.01

Table 4. 3. Mean seasonal cycle values of atmospheric CO_2 concentrations at Churchill and Fraserdale (2008–2012). "Diff" represents the mean difference in CO_2 values between the two sites. All values are in ppm.

4.1.2 Diurnal and day-to-day Variations

Figure 4.8 shows 2012 hourly CO_2 concentration values for Churchill and Fraserdale. Stronger diurnal and day-to-day variations in atmospheric CO_2 are clearly evident at the Fraserdale site, particularly during the growing season. This higher variability is indicative of the substantial regional biospheric influence around Fraserdale. The diurnal cycle of CO_2 is produced by the daily cycle of the atmosphere-vegetation CO_2 exchange, as well as the daily evolution of the planetary boundary layer. Atmospheric CO_2 accumulation begins at nighttime in the absence of photosynthesis when soil and plant respiration promotes a net transfer of CO_2 to the atmosphere. This accumulation is further enhanced by the development of a stable nocturnal boundary layer (NBL) created by rapid surface radiative cooling and its associated temperature inversion conditions. Vertical air motion is inhibited as the inversion acts like a lid causing a rapid buildup of atmospheric CO_2 within the shallow NBL. After sunrise, surface heating and thermal turbulence gradually erodes the stable atmosphere resulting in vertical mixing of surface air. This instability promotes the development of a high mixing depth, and CO_2 concentrations decreases in the so-called convectional boundary layer (CBL). Indeed, the decrease in CO_2 mixing ratios during the daytime is also due to the net uptake by vegetation during photosynthesis, particularly in the growing season. A typical summer day in Fraserdale and Churchill is illustrated in Figure 4.9 on July 20, 2012. Diurnal increase in atmospheric CO_2 (~382 ppm) begins at about 10pm local time. The accumulation continues through the night and early morning reaching a maximum (~402 ppm) at about 8am. Subsequently, a rapid decline in CO_2 can be observed, persisting throughout the day. It is important to note the stronger influence of the vegetative cycle on the diurnal variations at Fraserdale compared to Churchill. Nighttime CO_2 mixing ratios are higher at Fraserdale (higher autotrophic and heterotrophic respiration), while daytime CO_2 values are much lower during the

daytime (higher rate of photosynthesis). Also, Fraserdale exhibits a more distinct day-to-day variability in the diurnal CO_2 cycle (Figure 4.10). Overall, much of the daily variations in CO_2 concentrations at the two sites are likely due to synoptic weather events, as well as changes in air masses and carbon sources/sinks in upwind influence regions.

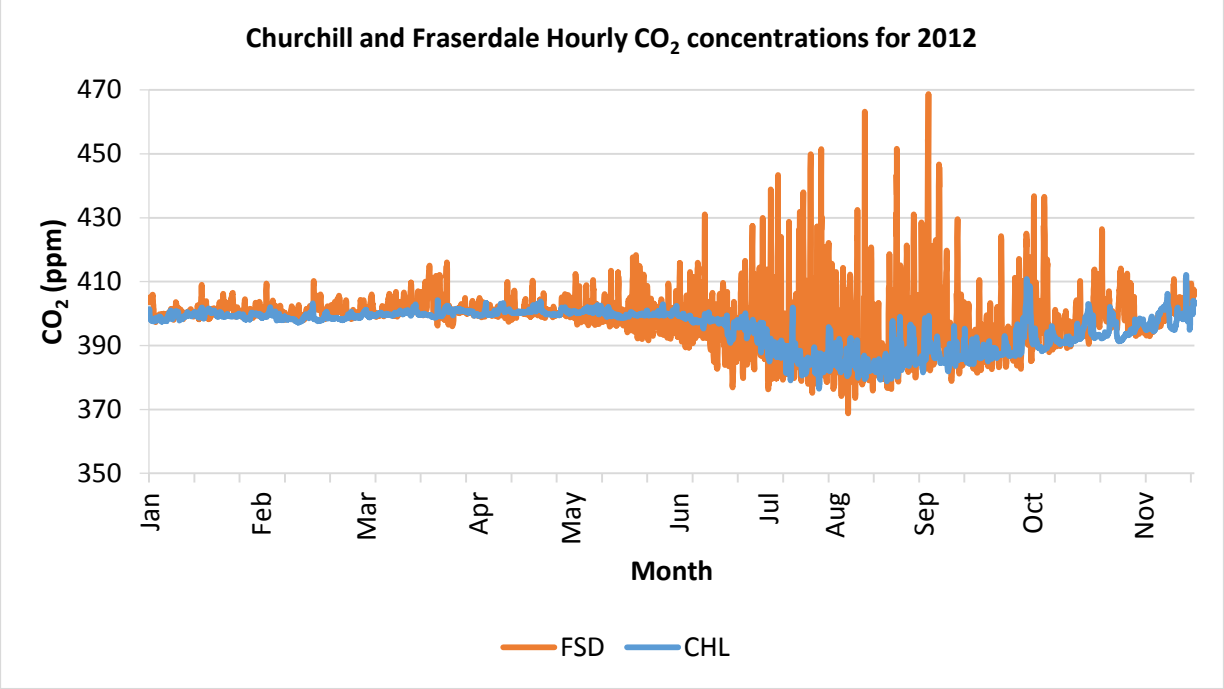

Figure 4. 8. Hourly CO_2 concentration at Churchill and Fraserdale for 2012. Hourly data provide information on diurnal and day-to-day variations in atmospheric CO_2 mixing ratios.

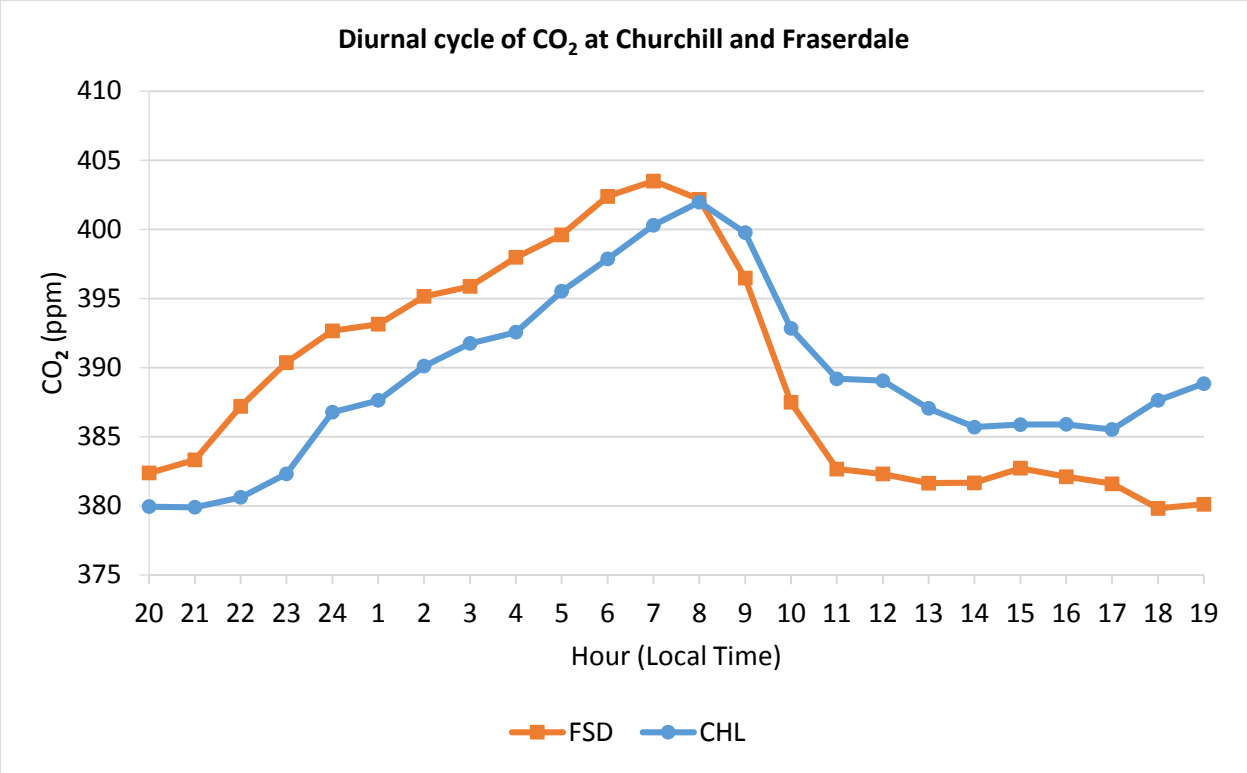

Figure 4. 9. Diurnal cycle of atmospheric CO_2 at Churchill and Fraserdale. The example shown is for July 20, 2012, and time is local time at Churchill.

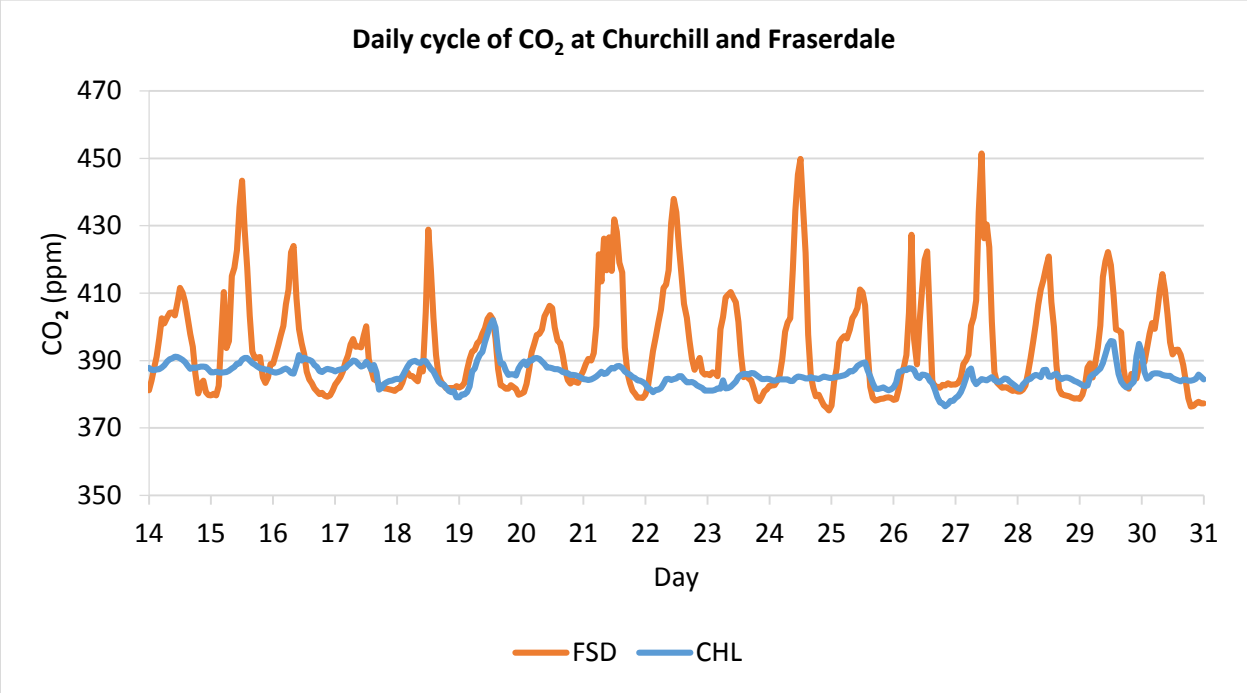

Figure 4. 10. Daily cycle of atmospheric CO_2 at Churchill and Fraserdale. The example shown is for July, 2012.

4.2 Results

4.2.1 STILT-Modelled CO_2 Concentrations (2008–2011)

The STILT model was used to simulate atmospheric CO_2 concentrations at Churchill and Fraserdale sites. Modelled concentrations were compared with observed weekly mixing ratios from 2008–2011. The results for Churchill show good agreement between simulated and observed CO_2 concentrations, with the regression model accounting for about 87% of the variability (Figure 4.11). The coefficients of determination (R^2) are 0.87, 0.89, 0.76, and 0.87 from 2008–2011. (Figure 4.12a–d). At Fraserdale, the simulated CO_2 concentration values compare reasonably against observations, though the R-squared values are much lower. The results show that about 56% of the variation of the modelled CO_2 values around the mean are explained by the observed values (Figure 4.13). R-squared values range from 0.43 in 2010 to 0.66 in 2011 ((Figure 4.14a–d).

To examine the effect of uncertainties in mixing heights and the growth/decay of the PBL on model performance, morning (9:00 UTC) and afternoon (21:00 UTC) data were analyzed separately. The results show that modelled CO_2 concentrations in the afternoon were closer to the observed concentrations. For the study period 2008–2011, afternoon results at Churchill have a higher R-squared value of about 0.90 compared to 0.85 in the morning (Figure 4.15a and b). At Fraserdale, the difference in the R-squared values is even much higher; 0.82 in the afternoon and 0.08 in the morning (Figure 4.16a and b). This indicates that the STILT model performed better during daytime, but could not adequately resolve the diurnal evolution of the PBL.

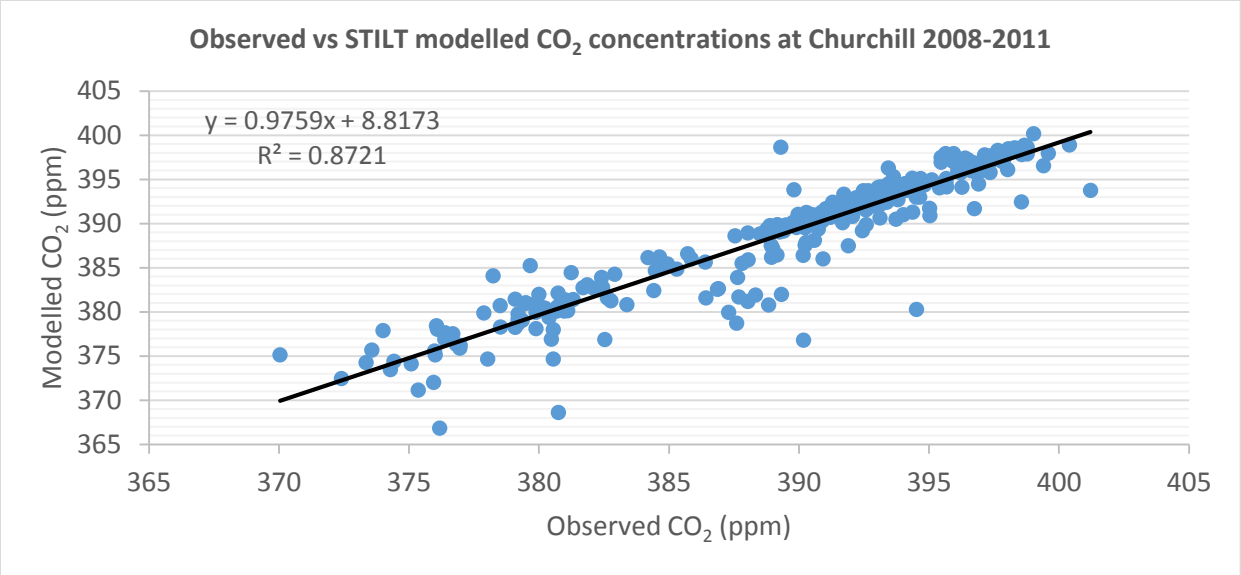

Figure 4. 11. Observed vs STILT modelled CO_2 concentrations at Churchill from 2008 - 2011.

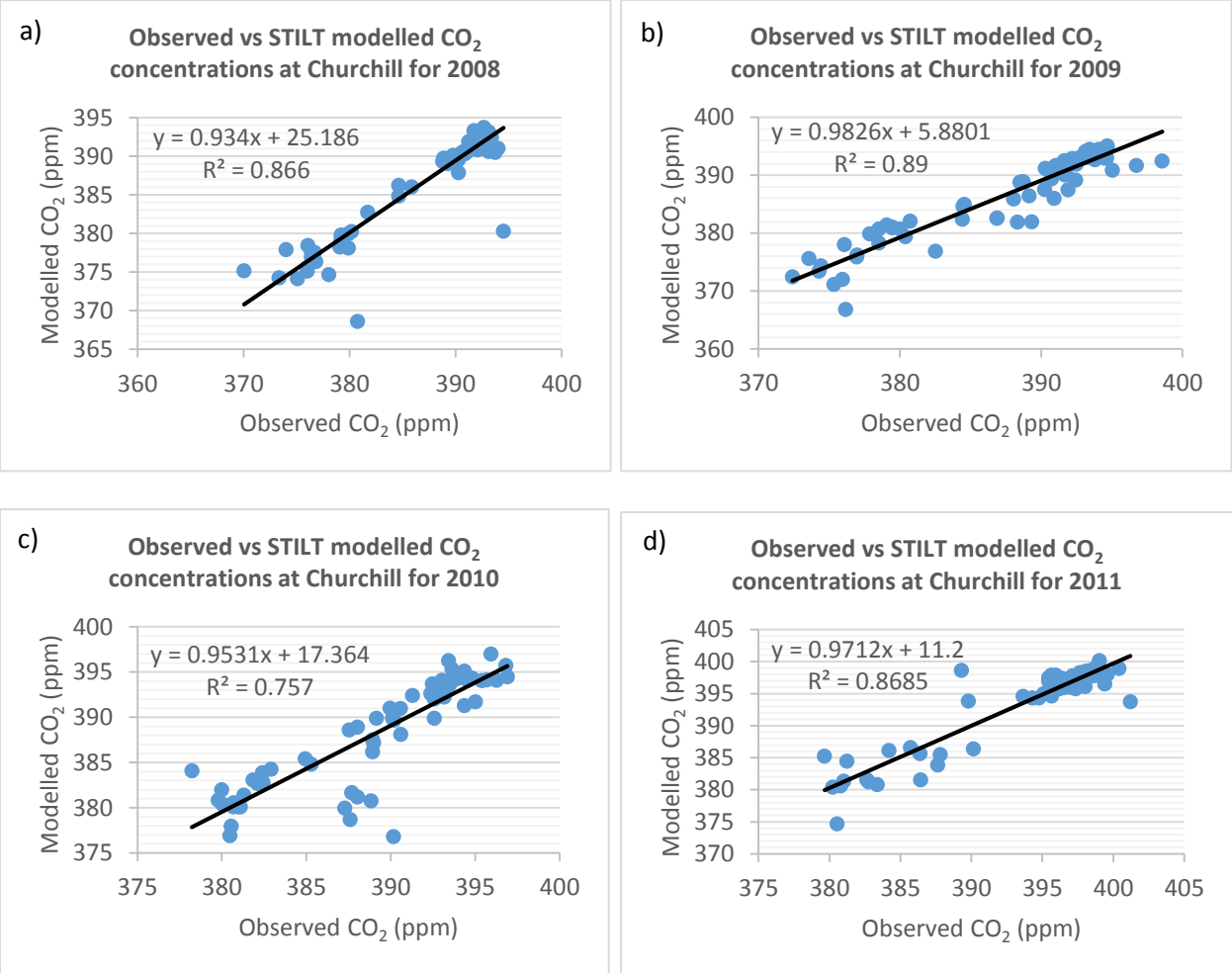

Figure 4. 12. Observed vs STILT modelled CO_2 concentrations at Churchill; (a) 2008 (b) 2009 (c) 2010 (d) 2011.

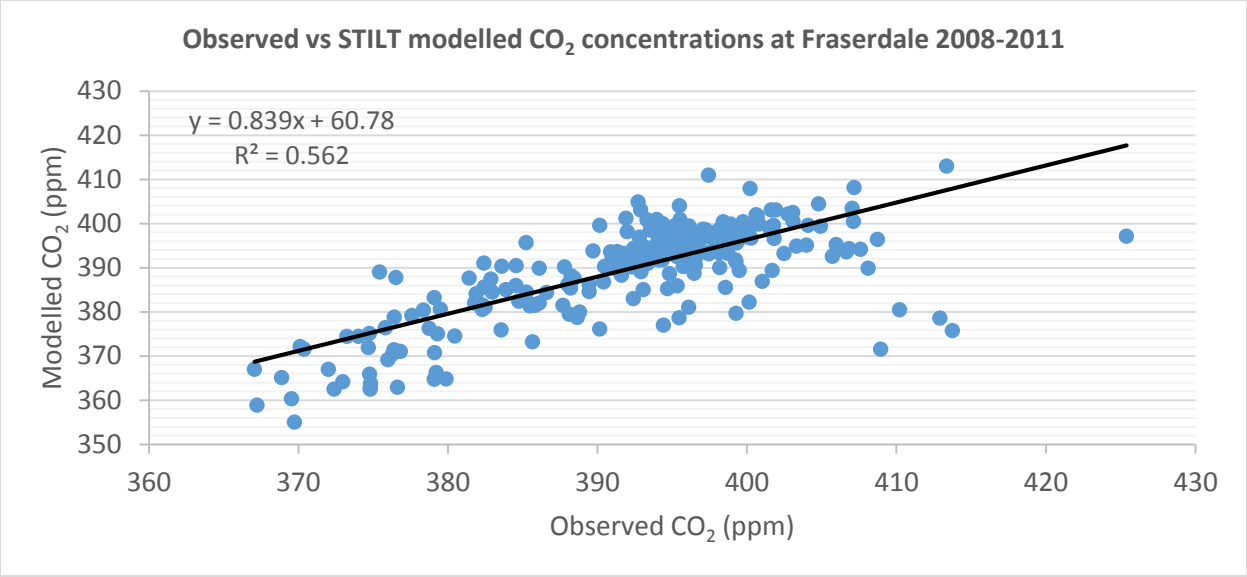

Figure 4. 13. Observed vs STILT modelled CO_2 concentrations at Fraserdale from 2008 - 2011.

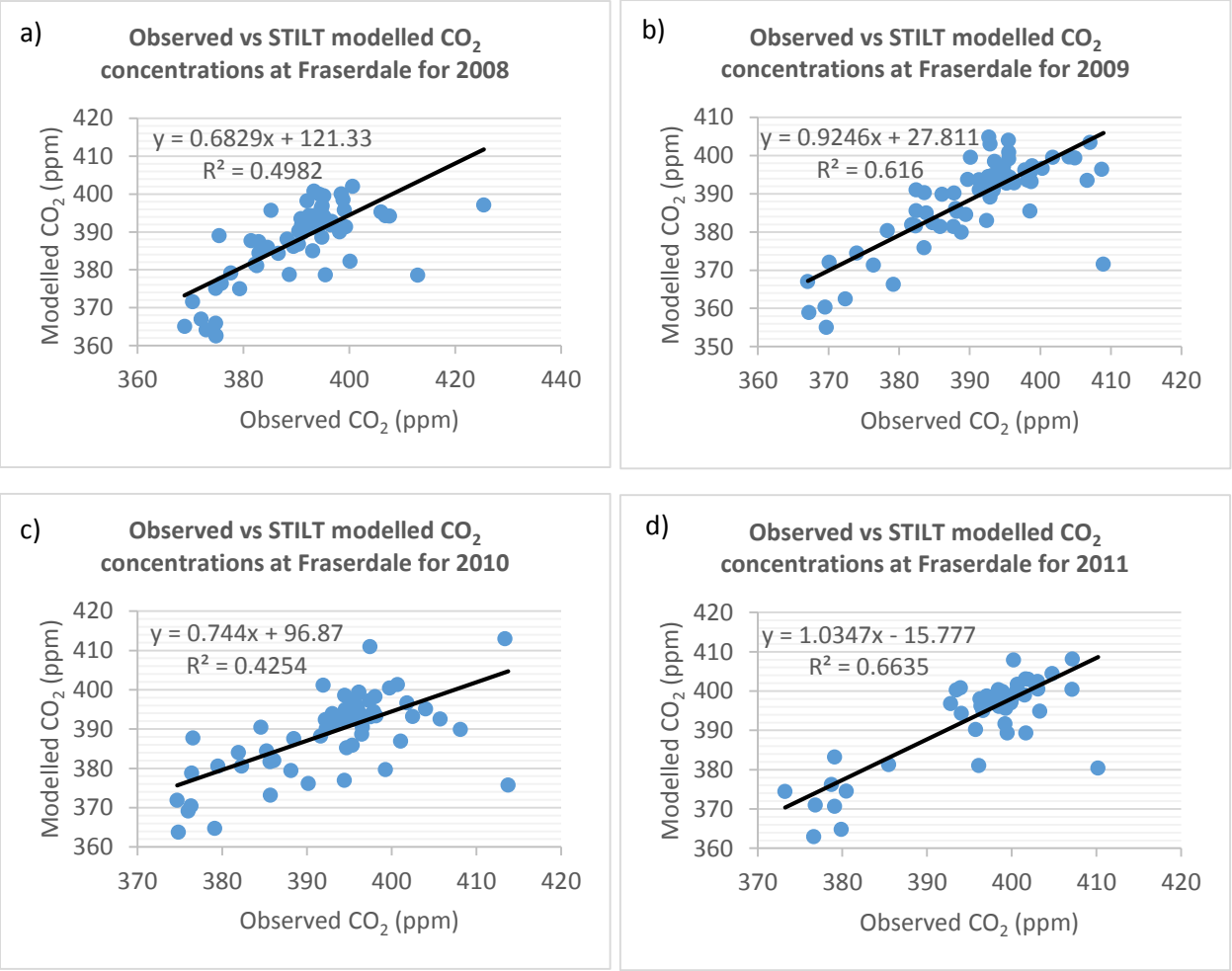

Figure 4. 14. Observed vs STILT modelled CO_2 concentrations at Fraserdale; (a) 2008 (b) 2009 (c) 2010 (d) 2011.

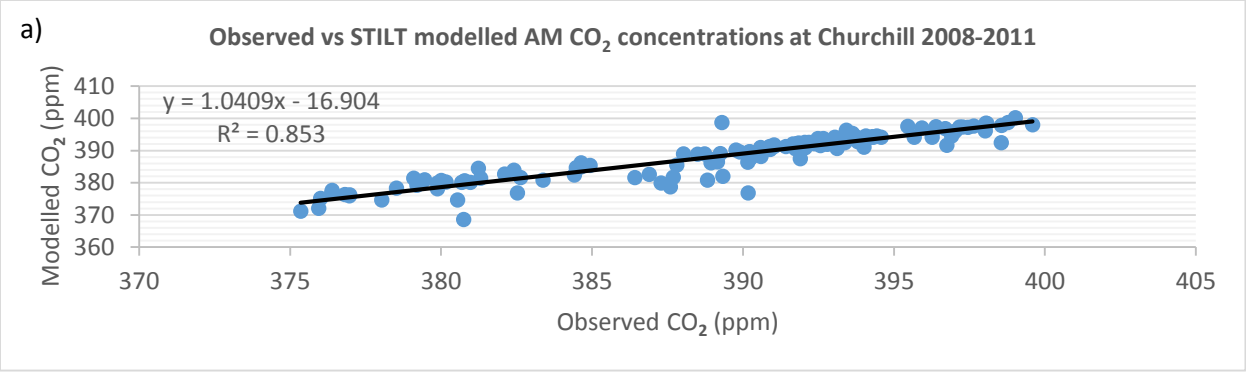

Figure 4. 15. Observed vs STILT modelled CO_2 concentrations at Churchill 2008-2011; (a) Morning, 9:00 UTC (b) Afternoon, 21:00 UTC

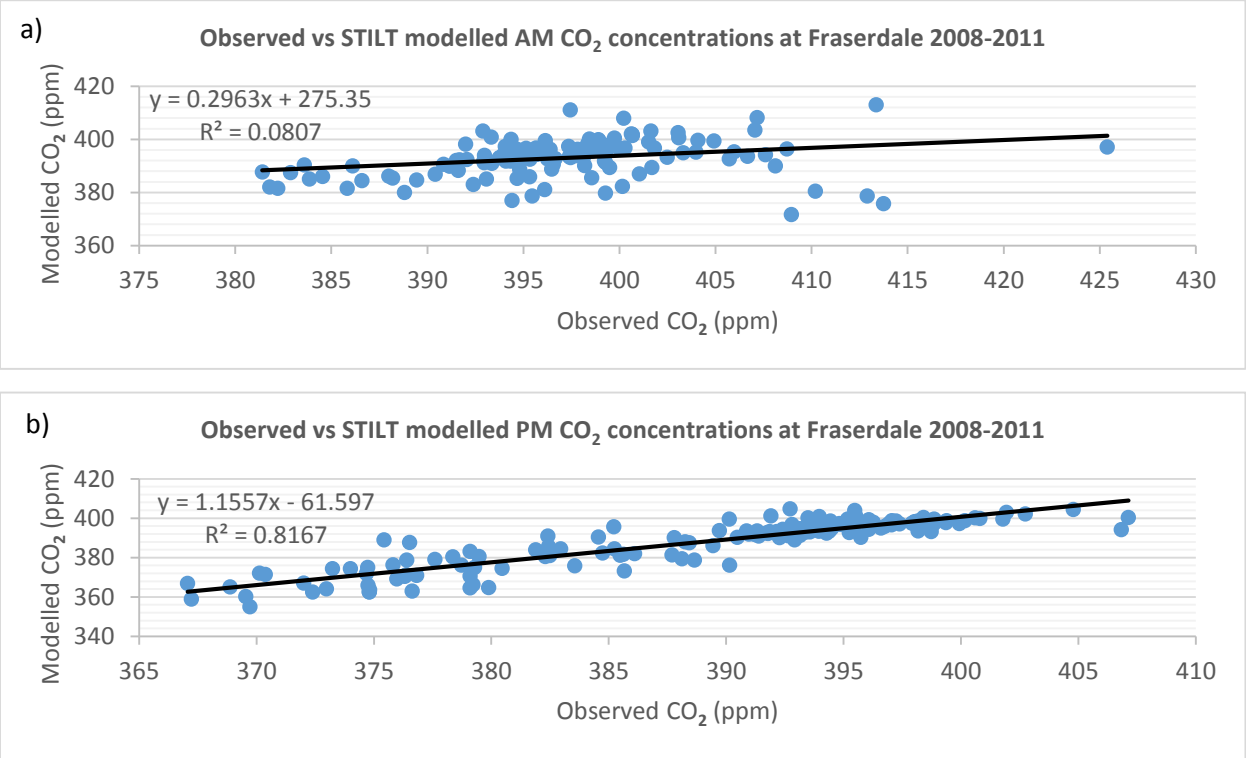

Figure 4. 16. Observed vs STILT modelled CO_2 concentrations at Fraserdale 2008-2011; (a) Morning, 9:00 UTC (b) Afternoon, 21:00 UTC

Further analyses were carried out to examine the bias in the model results and how much the simulated CO_2 concentration values deviated from the actual observations. Observed CO_2 values for each measurement time were subtracted from the modelled values to derive the bias (or error) in the model results. Table 4.4 shows the mean difference between modelled and observed CO_2 values for Churchill and Fraserdale from 2008–2011. The mean model bias for 2008 was -0.36 ± 2.56 ppm and -2.55 ± 7.59 ppm, for Churchill and Fraserdale, respectively. The results reveal that the STILT model underestimated atmospheric CO_2 concentrations at both sites throughout the study period. Moreover, the model bias was significantly higher at Fraserdale compared to Churchill (Table 4.5). The box plot in Figure 4.17 provides a more detailed analysis of the model bias. For the study period at Churchill, the values of the 25^{th} percentile (lower quartile), the 50^{th} percentile (median), and the 75^{th} percentile (upper quartile) are -1.00, -0.02, and 0.58 ppm, respectively. Thus, 50% of the data points fall within a small interquartile range. Similarly, the whiskers extend over a small range with the value of the bottom and top whisker of -3.31 and 2.84, respectively. This denotes that overall, modelled and observed CO_2 concentrations have a high level of agreement with each other. At Fraserdale, the distribution of the data is more widespread, with a lower quartile, median and upper quartile of -4.40, -0.78, and 1.00 ppm, respectively, for the study period. Also, the bottom and top whiskers indicate a larger range of about -12.43 and 8.63 ppm, respectively. It is evident, therefore, that the model bias is significantly higher at Fraserdale. In addition, model bias was examined for morning and afternoon data. At Churchill, the biases in the modelled morning and afternoon CO_2 values are small, and the afternoon data show good agreement with observed values for all years in the study period (Figure 4.18). In contrast, model biases are higher at Fraserdale, particularly in the morning, with a median of 0.37 and -1.18 ppm for afternoon and morning, respectively, in 2008 (Figure 4.19).

Mean Model Bias		
Year	CHL	FSD
2008	-0.36 ± 2.56	-2.55 ± 7.59
2009	-0.88 ± 2.34	-1.64 ± 6.70
2010	-0.89 ± 2.96	-3.75 ± 7.78
2011	-0.14 ± 2.32	-2.03 ± 5.69

Table 4. 4. Mean model bias; calculated by finding the average of the difference between modelled CO_2 concentrations and observed concentrations.

t-Test: Two-Sample Assuming Unequal Variances		
	FSD 2008	*CHL 2008*
Mean	-2.550348254	-0.357899007
Variance	57.64984752	6.579129761
Observations	71	71
Hypothesized Mean	0	
df	86	
t Stat	-2.305118305	
P(T<=t) one-tail	0.01178402	
t Critical one-tail	1.662765449	
P(T<=t) two-tail	**0.02356804**	
t Critical two-tail	1.987934206	

Table 4. 5. Statistical test to determine the difference in the mean model bias between Churchill and Fraserdale. The null hypothesis is that there is no statistically significant difference in the model bias between the two sites. The alternative hypothesis is that the mean model bias is higher at Fraserdale, and that this difference is statistically significant. Since the p-value for the t-test is <0.05, the null hypothesis is rejected.

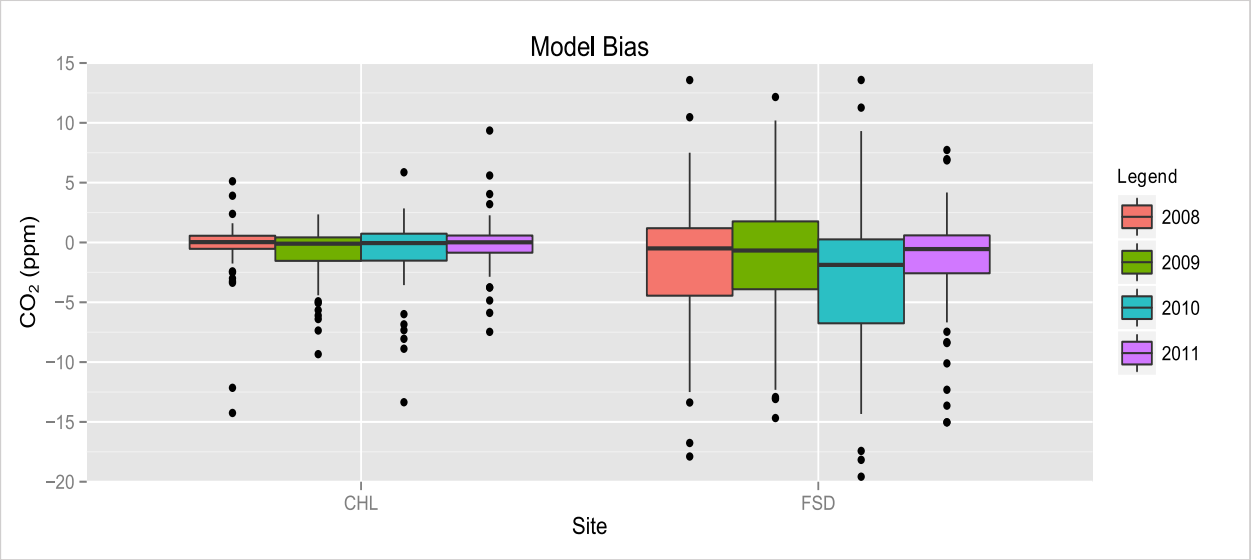

Figure 4. 17. Box plots showing model bias for Churchill and Fraserdale (2008-2011). The box extends from the 25th percentile (lower quartile) to the 75th percentile (upper quartile), with a line at the 50th percentile (median). The range of values from the lower to upper quartile is referred to as the interquartile range, which represents the middle 50% of the data. The whiskers extend from the box to the bottom and top bars, and represent the lowest and highest data values respectively, excluding the extreme values. The outliers are those values that are far away from most of the other values, and they are represented as black dots.

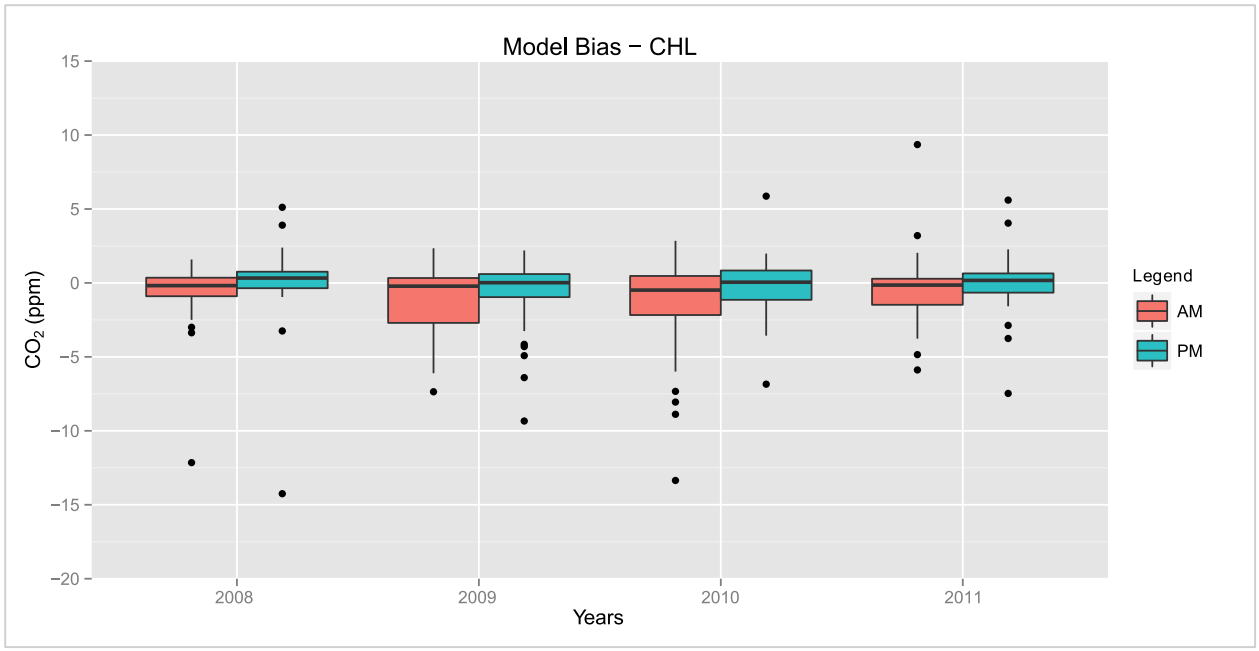

Figure 4. 18. Box plots showing morning (9:00 UTC) and afternoon (21:00 UTC) model bias for Churchill (2008-2011).

Figure 4. 19. Box plots showing morning (9:00 UTC) and afternoon (21:00 UTC) model bias for Fraserdale (2008-2011).

4.2.2 STILT Model Assessment

Another approach to assess the results of this study is to compare the STILT modelled CO_2 concentrations against measurements from CarbonTracker (CT). Daily afternoon (21:00 UTC) atmospheric CO_2 concentrations at Churchill and Fraserdale were obtained from CT2013, with a 1° x 1° horizontal grid resolution. At Churchill, statistical evaluations reveal that there is good agreement (87%) between STILT and CarbonTracker total CO_2 concentrations (Figure 4.20a). In addition, STILT was able to adequately represent contributions from the biosphere (Figure 4.20b), with 88% of the variation in the modelled values around the mean being explained by the CT measurements. Figure 4.20c shows a time series for both STILT and CT total atmospheric CO_2 concentration at Churchill, from January to December 2012. STILT-simulated CO_2 values compare reasonably against CT concentrations, capturing both the timing and magnitude of the day-to-day variations in atmospheric CO_2. The mean value of the CT measurement is 395.28 ppm with a standard deviation of 7.64 ppm, while those of STILT are 394.67 ppm and 6.87 ppm, respectively. Further analysis continues to show a close match between STILT and CT measurements. From January to April, maximum and minimum CO_2 concentrations for CT are 405.67 ppm and 397.67 ppm, respectively, with a standard deviation of 1.38 ppm. For STILT, the maximum and minimum CO_2 values are 402.55 and 395.87, respectively, with a standard deviation of 1.29 ppm (Figure 4.21a). Between May and August, CT maximum and minimum concentrations are 403.80 ppm and 361.97 ppm, respectively, with a standard deviation of 8.78 ppm. Similarly, STILT captures a maximum concentration of 401.63 ppm, however, with a relatively higher minimum value of 370.02 ppm, and a standard deviation of 8.04 ppm (Figure 4.21b). In the September – December period, maximum and minimum CO_2 concentrations for CT are 410.19 ppm and 382.55 ppm respectively, with a standard deviation of 6.56 ppm; while STILT obtains

maximum and minimum CO_2 values of 406.49 ppm and 383.17 ppm, respectively, with a standard deviation of 5.75 ppm (Figure 4.21c).

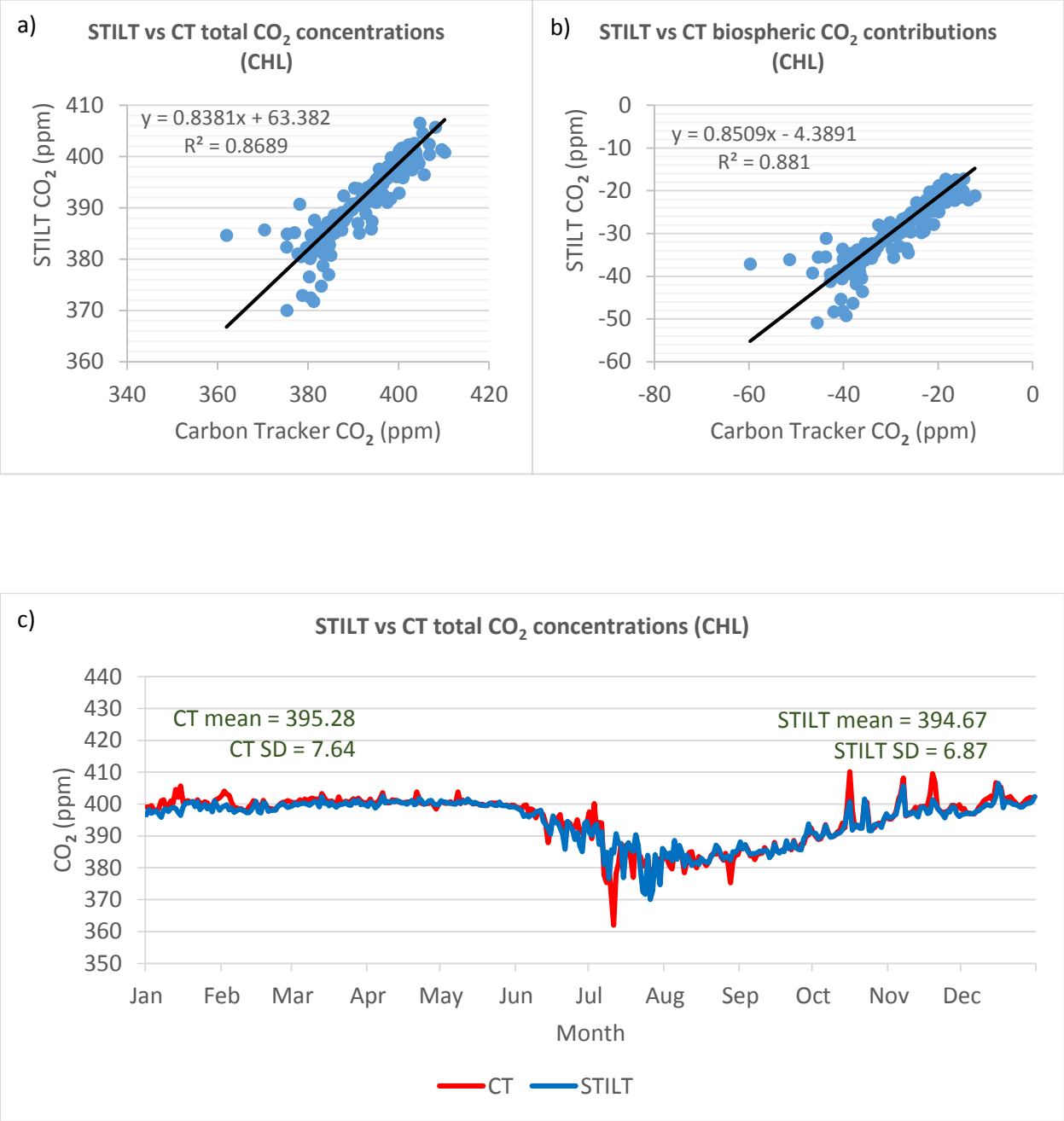

Figure 4. 20. STILT modelled CO_2 concentrations compared against CarbonTracker measurements obtained from a 1° X 1° horizontal grid. The results shown here are daily afternoon (21:00 UTC) data for 2012. (a) STILT vs CT total CO_2 concentration at Churchill (b) STILT vs CT biosphere contributions towards CO_2 concentrations at Churchill. (c) Time series from January to December 2012, showing comparison between STILT and CT total CO_2 concentrations at Churchill.

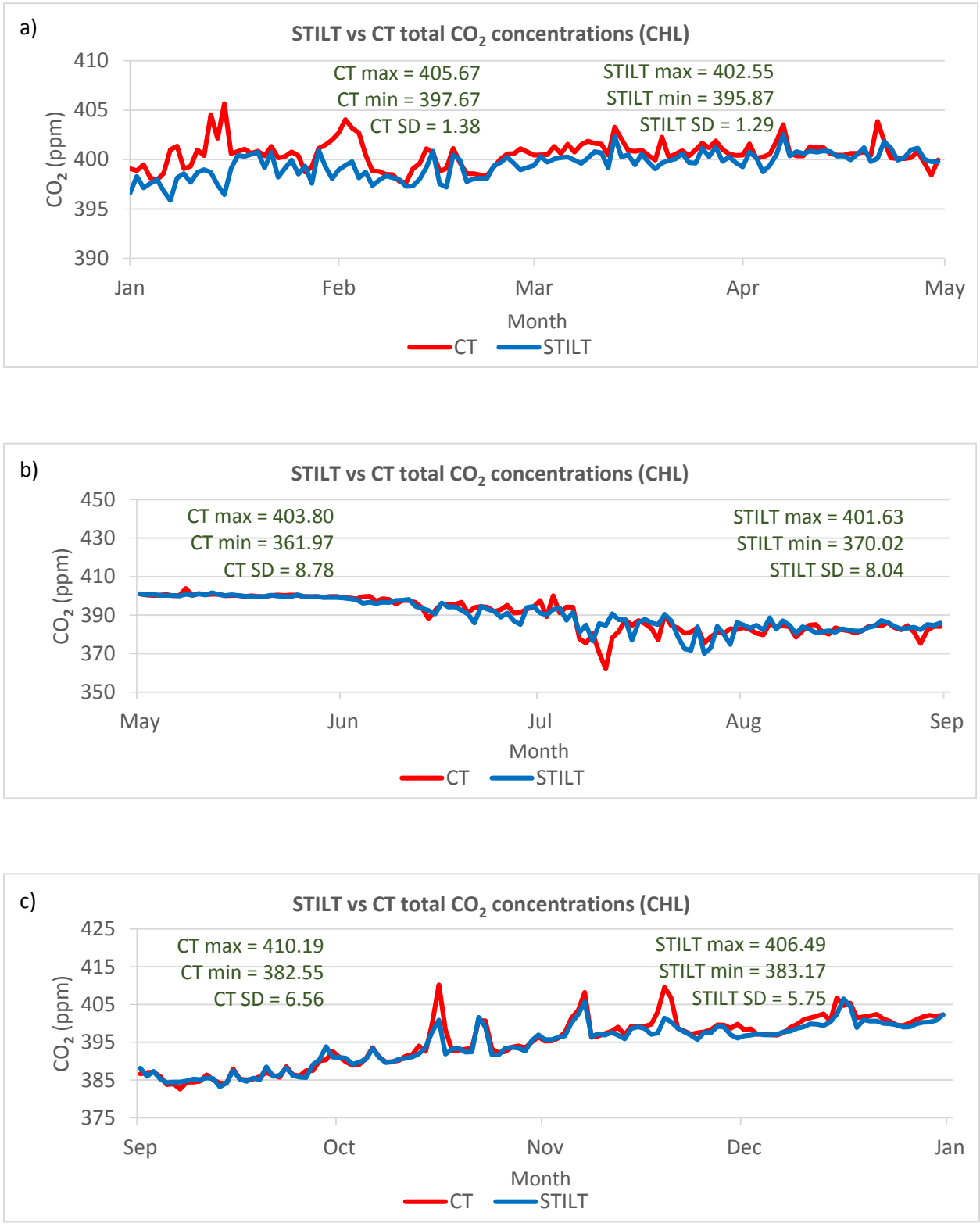

Figure 4. 21. Time series of STILT modelled CO_2 concentrations compared against CarbonTracker measurements, using 2012 afternoon (21:00 UTC) data at Churchill. (a) January to April. (b) May to August (c) September to December.

At Fraserdale, STILT CO_2 simulations were also in reasonable agreement with CT measurements, with an R-squared value of 0.86 for both total concentration and biospheric CO_2 contributions (Figure 4.22a and b). STILT total CO_2 concentrations are plotted against CT values in a time series as shown in Figure 4.22c. The mean atmospheric CO_2 concentrations for CT and STILT in 2012 are 394.92 ± 8.54 ppm and 392.33 ± 11.84 ppm, respectively. Throughout the year, there is strong correlation between STILT and CT CO_2 values (Figure 4.23a and c), particularly in January – April (CT max = 407.11, CT min = 398.11, CT SD = 1.92; STILT max = 407.65, STILT min = 397.46, STILT SD = 1.91) and September – December (CT max = 414.02, CT min = 381.21, CT SD = 7.37; STILT max = 410.95, STILT min = 377.52, STILT SD = 7.44) periods. However, the results differ in the period from May – August when maximum and minimum CT CO_2 concentrations are 403.36 ppm and 374.61 ppm, respectively, compared to a max of 405.05 ppm and a min of 344.09 ppm for STILT. Figure 4.23b reveals that, though there is reasonable agreement in the timing of the day-to-day variations in atmospheric CO_2 concentrations, there is considerable disparity in the magnitude of the daily variations between CT and STILT, with a standard deviation of 8.06 ppm and 12.28 ppm, respectively.

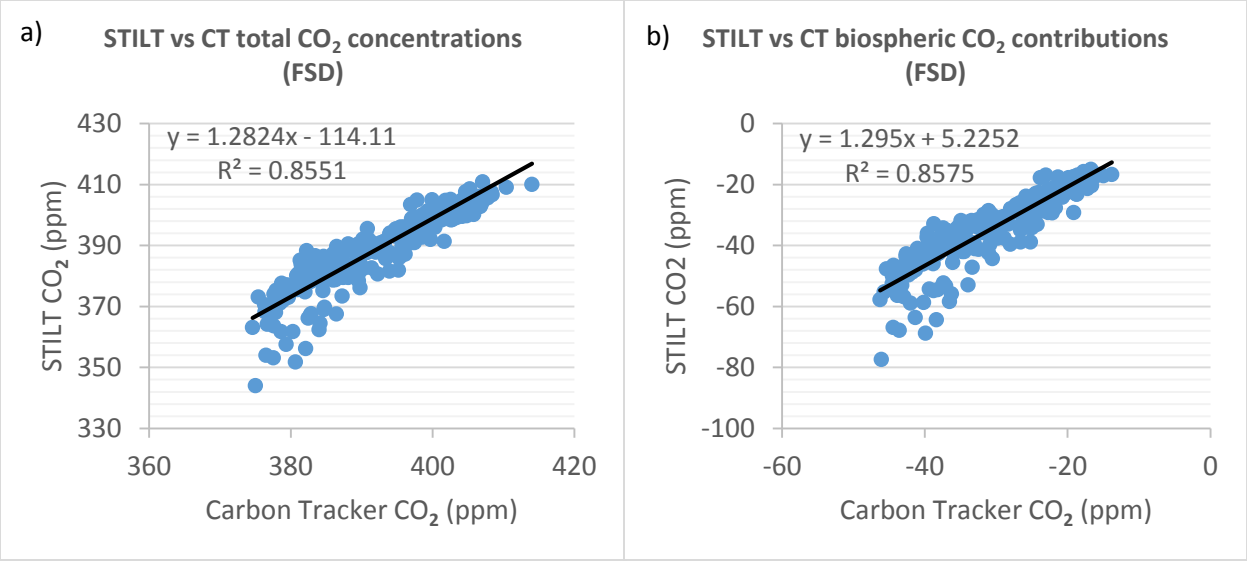

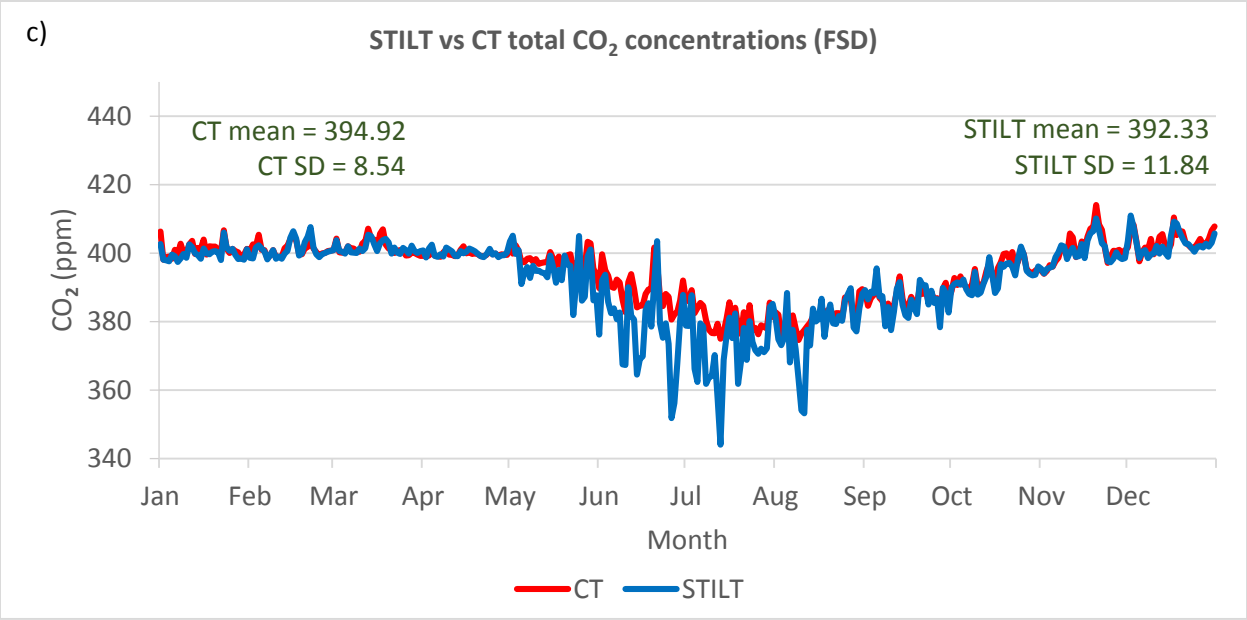

Figure 4. 22. STILT modelled CO_2 concentrations compared against CarbonTracker measurements obtained from a 1° X 1° horizontal grid. The results shown here are daily afternoon (21:00 UTC) data for 2012. (a) STILT vs CT total CO_2 concentration at Fraserdale (b) STILT vs CT biosphere contributions towards CO_2 concentrations at Fraserdale. (c) Time series from January to December 2012, showing comparison between STILT and CT total CO_2 concentrations at Fraserdale.

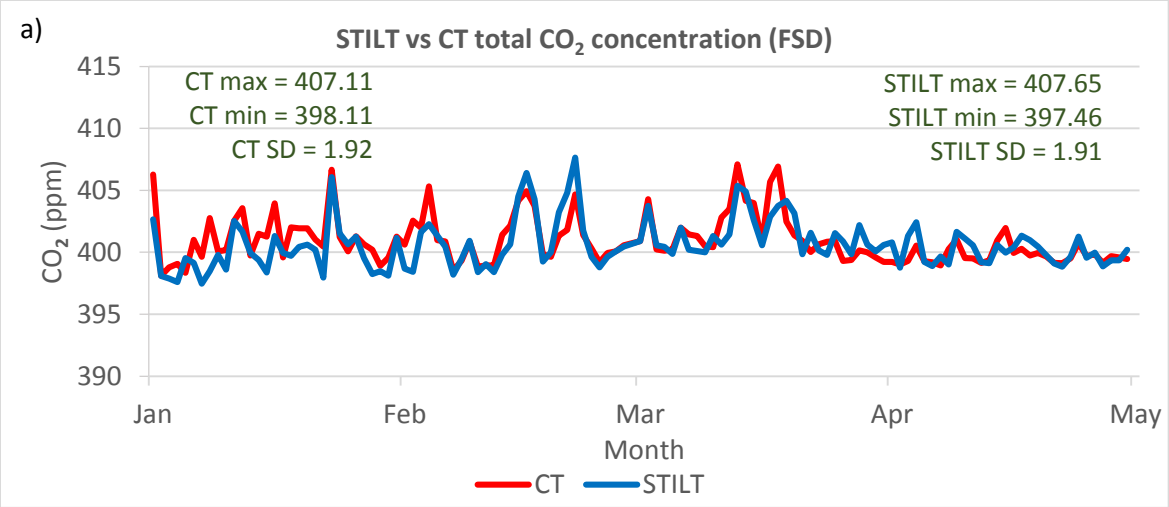

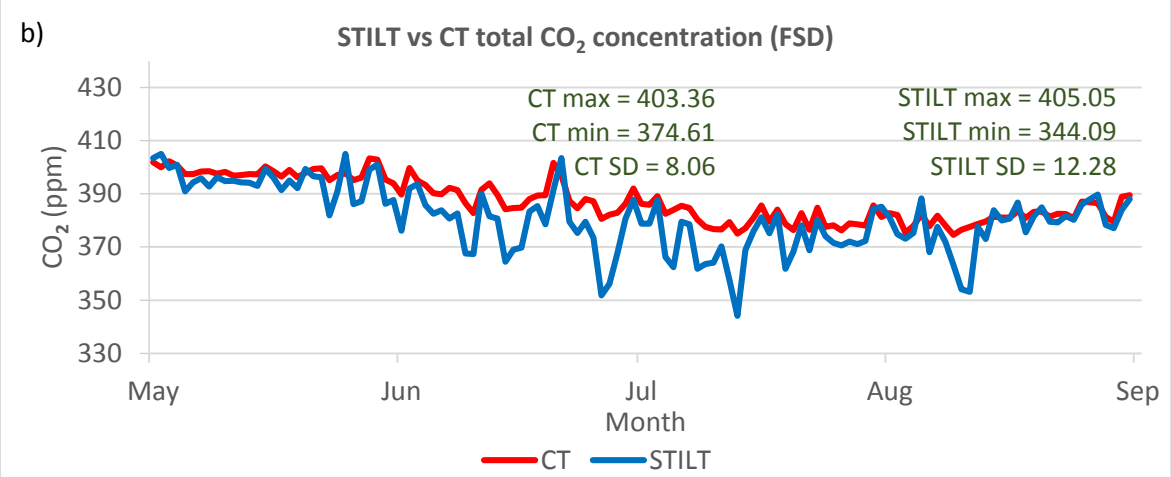

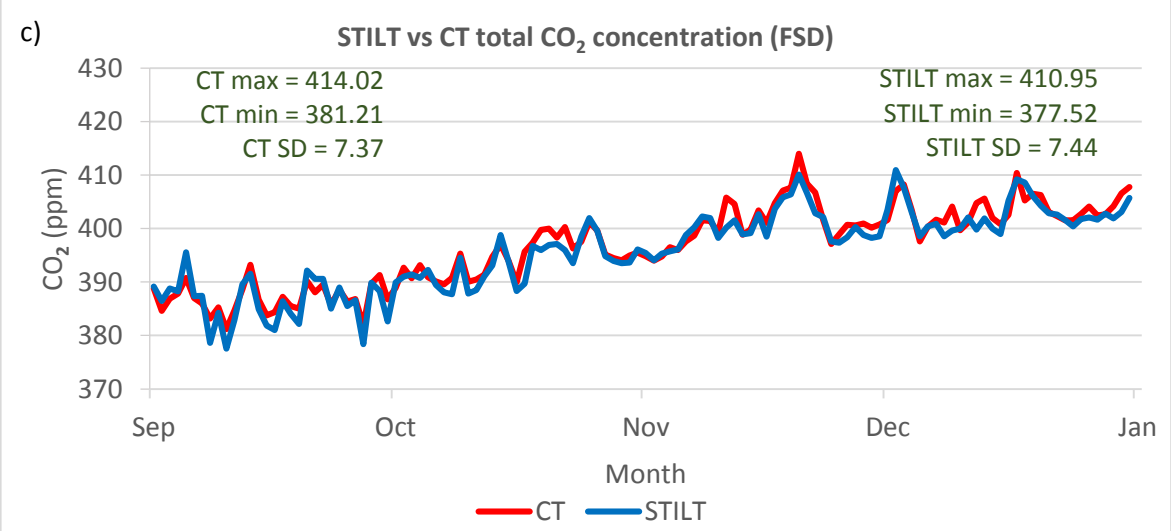

Figure 4. 23. Time series of STILT modelled CO_2 concentrations compared against CarbonTracker measurements, using 2012 afternoon (21:00 UTC) data at Fraserdale. (a) January to April. (b) May to August (c) September to December.

4.2.3 Evaluation of STILT and Carbon Tracker CO_2 Concentrations

Smoothed curves fitted to the daily afternoon data derived from the digital filtering technique of Nakazawa et al. (1997) are shown in Figure 4.24a and b, for Churchill and Fraserdale, respectively. This modified digital filtering approach includes Fourier harmonics, Reinsch-type cubic spline and Butterworth filter. It was developed at Tohoku University, and has been applied extensively to CO_2, CH_4, and isotopic flask measurements (Nakazawa et al., 1991a, 1991b, 1992, 1993; Higuchi et al., 2003; Patra et al., 2008; Saeki et al., 2013). Here, STILT-simulated CO_2 concentrations and CT measurements are evaluated with observed CO_2 mixing ratios from the tower sites. Both STILT and CT CO_2 values agree well with the observations at Churchill, capturing both the maximum and minimum concentrations. There is a slight disparity (~1 ppm) in the fitted curves between January to April, and in December, with the STILT values being relatively closer to the tower observations. The mean values of the fitted curves are 395.14 ± 6.13 ppm, 395.58 ± 6.70 ppm and 395.25 ± 6.34 ppm for STILT, CT, and observed measurements, respectively. Also, there is reasonable agreement at Fraserdale, but with more disparity in the fitted data. In January, the STILT model appears to slightly underestimate atmospheric CO_2 concentration, while CT measurements record a little above observed values. Between March and May, both STILT and CT overestimate CO_2 concentrations by about 2 ppm. An earlier rapid decline in atmospheric CO_2 is simulated by STILT, deviating considerably from the CT measurements which are in strong agreement with the tower observations. Consequently, the STILT minimum atmospheric CO_2 concentration is about 5 ppm lower, although the mean values of the fitted curves are quite comparable at 393.06 ± 10.11 ppm, 394.96 ± 8.71 ppm, and 394.01 ± 8.15 ppm, for STILT, CT and observation, respectively. Maximum CO_2 values occur in December; about 406 ppm for STILT, 407 ppm for CT, and 404 ppm for the tower observation.

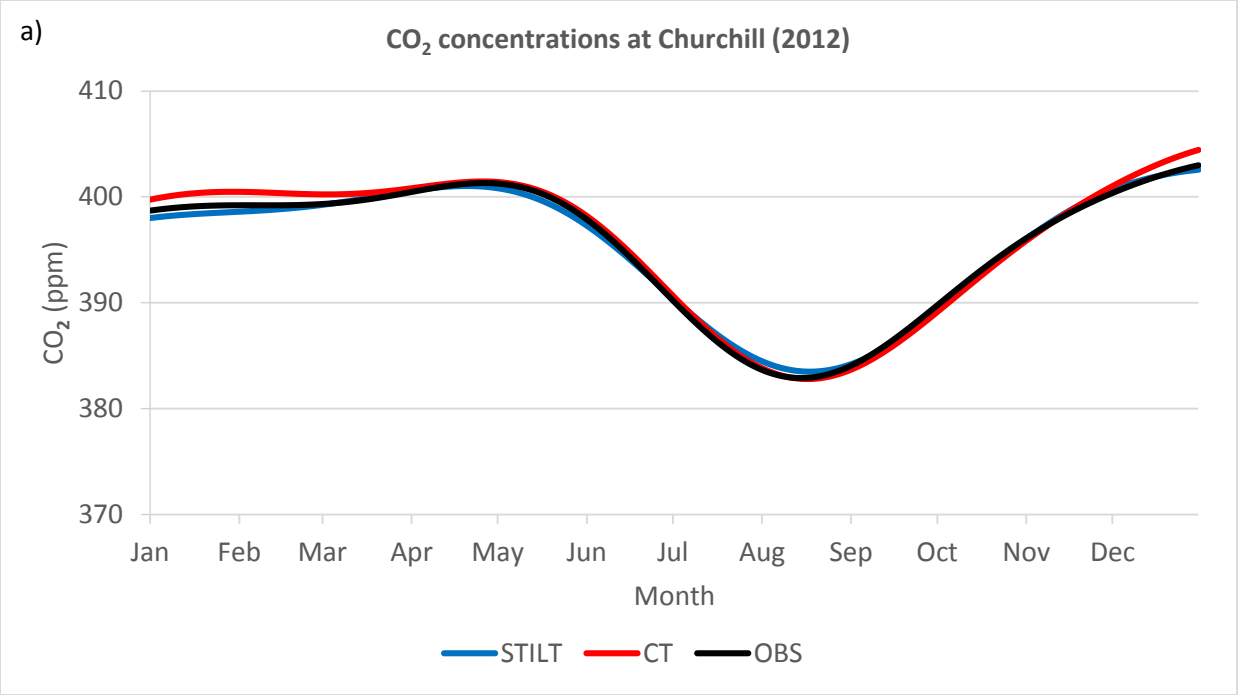

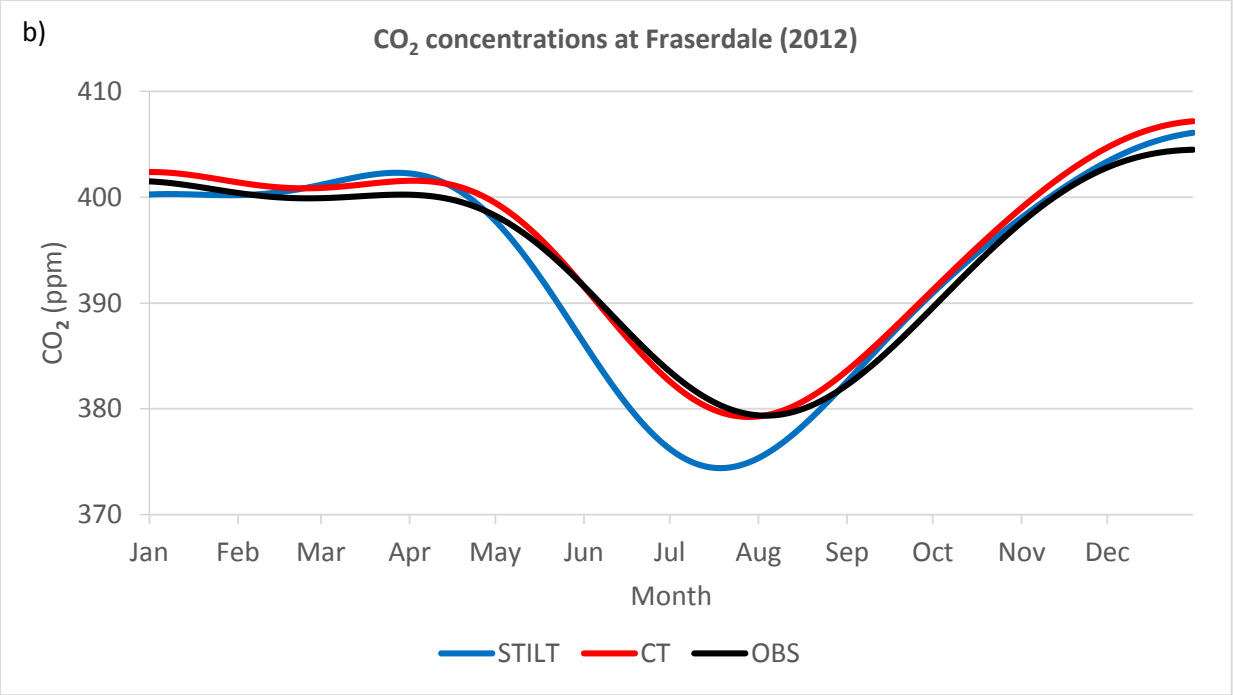

Figure 4. 24. Fitted curves to the daily afternoon (21:00 UTC) data for STILT, CarbonTracker (CT), and tower observations (OBS), obtained via the curve-fitting procedure described in Nakazawa et al. (1997). In this study, the number of harmonics for seasonal cycle "n" is set equal to 2, and the cut-off period of Butterworth filter for short term variation is set to be 4 months to attenuate the highest-order component of the Fourier harmonics to 50 per cent. (a) Churchill. (b) Fraserdale.

In order to further assess the difference between STILT, CT, and observation (OBS), their performances are examined with respect to three features of the seasonal CO_2 cycle: (i) timing of the seasonal minimum; (ii) magnitude of the seasonal minimum, and (iii) seasonal amplitude. Indeed, the seasonal cycle of atmospheric CO_2 concentration is basically a reflection of the photosynthetic decay cycle of the terrestrial biosphere. Figure 4.25 shows a comparison of the smoothed seasonal cycles obtained for STILT, CT and OBS data by applying the curve-fitting procedure of Nakazawa et al. (1997). The timing of the 2012 seasonal minimum at Churchill shows that there is good agreement between STILT, CT, and OBS, with the minimum CO_2 occurring on August 19, August 18, and August 16, respectively. The magnitude of the seasonal minimum at Churchill is -12 ppm for STILT, and -13 ppm for CT and OBS. The seasonal amplitude, which is defined operationally as the difference between the maximum and minimum concentration values in the same year, is well captured at Churchill by STILT (19 ppm for both STILT and OBS) and CT (21 ppm). At Fraserdale, the seasonal minimum CO_2 occurs on July 20, July 30, and August 5, according to STILT, CT, and OBS, respectively (Figure 4.25b). This indicates that STILT and CT were unable to adequately resolve the timing of the seasonal minimum, with an occurrence of about 6 (CT) to 16 (STILT) days earlier than OBS. Also, the magnitude of the seasonal minimum varies from -15 ppm for OBS to -19 ppm for STILT, demonstrating that the STILT model overestimates photosynthetic carbon uptake at Fraserdale. Consequently, the seasonal amplitude is about 6 ppm (2 ppm) higher for STILT (CT) than OBS.

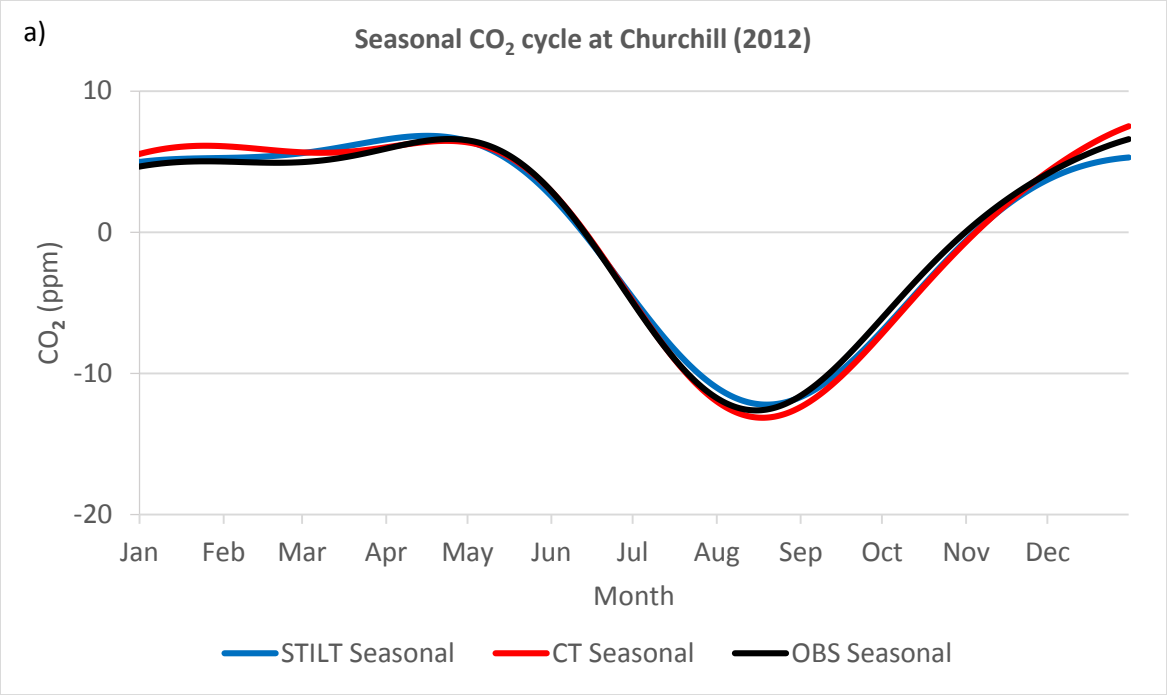

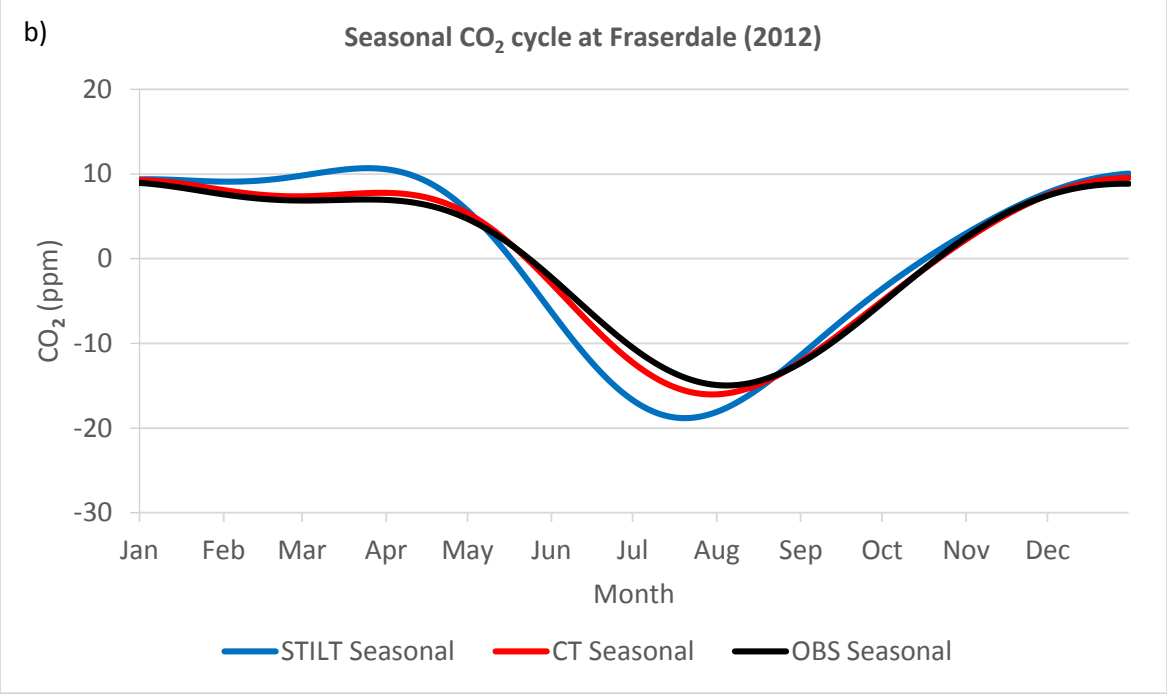

Figure 4. 25. Comparison of the smoothed seasonal cycles obtained for STILT, CT and OBS data by applying the digital filtering technique of Nakazawa et al. (1997). In this study, the number of harmonics for seasonal cycle "n" is set equal to 2, and the cut-off period of Butterworth filter for short term variation is set to be 4 months to attenuate the highest-order component of the Fourier harmonics to 50 per cent. (a) Churchill. (b) Fraserdale.

4.3 Discussions

4.3.1 Model Biases

STILT-modelled results for the 2008–2011 study period (Figure 4.11 – 4.14) indicate that the simulated CO_2 values compare reasonably against observations, although the model performs better in Churchill ($R^2 = 0.87$) compared to Fraserdale ($R^2 = 0.56$). The mean model bias, defined as the average difference between modelled and observed CO_2 values, revealed that STILT underestimated atmospheric CO_2 concentrations throughout the study period (Table 4.4 and 4.5, Figure 4.17), with a greater bias at Fraserdale (-2.50 ppm) compared to Churchill (-0.57 ppm). Furthermore, analysis of the 2012 daily afternoon data, as well the smoothed seasonal CO_2 cycle demonstrated that model bias was greatest during summer, particularly at Fraserdale (Figure 4.24 and 4.25). This study seeks to address questions such as: What factors are responsible for these model biases? Are the biases caused by inherent model errors, or inaccurate surface flux estimates from CarbonTracker? Why do the model biases reach a maximum during summertime, mostly at Fraserdale? Generally, discrepancies between modelled and observed values exist due to a number of influences, including uncertainties in advection, PBL mixing, a priori surface fluxes, and background values.

4.3.2 Errors in Horizontal Velocities

Errors in atmospheric transport based on uncertainties in horizontal winds may lead to errors in estimates of surface flux contributions to the receptor. The magnitude of errors in wind fields, and their spatial and temporal covariances, have been quantified using direct comparison of assimilated winds to radiosonde observations (Lin and Gerbig, 2005). The uncertainty in modelled CO_2 concentration due to advection errors could be as large as 5.9 ppm, particularly during the growing season (Gerbig et al., 2008). Thus, the bias in the STILT-modelled CO_2 can be partly explained in terms of uncertainties in the NARR wind fields, and advection error. Fraserdale incurred a greater magnitude of error due to its location in the boreal forest. A very close relationship exists between biospheric fluxes and atmospheric concentrations, and therefore, errors in model particle trajectories and simulated footprints will be amplified in regions with greater vegetative influence. In addition, stronger spatial variability in biospheric fluxes—characteristic of a region such as Fraserdale—causes stronger variability in atmospheric mixing ratios, and consequently, larger biases in modelled CO_2 results (Gerbig et al., 2003a; Lin et al., 2004a). During summer months, in the presence of active vegetation, model transport uncertainties due to advection lead to errors in simulated CO_2 from biospheric fluxes within the near-field (surface influence region within ~3 days of the measurement location). In this study, STILT-modelled summer (afternoon) minimum CO_2 concentration at Fraserdale was ~5 ppm lower than tower observations (Figure 4.24b); a value consistent with the findings of Lin and Gerbig, 2005.

4.3.3 Uncertainties in Vertical Mixing Processes

In addition to errors in horizontal velocities, biases in simulated CO_2 concentrations also exist due to uncertainties in vertical mixing and velocities (Denning et al., 1996b). Inaccurate model representation of vertical mixing processes may cause significant biases in the vertical redistribution of the influence from surface fluxes to a measurement site located within the PBL (Gerbig et al., 2008). It is difficult to quantify the uncertainties in vertical transport, and to propagate these errors in mixing heights to derive uncertainties in CO_2 mixing ratios. Typically, deeper vertical mixing causes smaller atmospheric signals since the PBL-plume becomes diluted and therefore, the surface flux influence is considerably diminished. However, strong diurnal variations in mixing depth further complicates the uncertainties between daytime and nighttime mixing heights. Indeed, the nocturnal boundary layer (NBL) is characterized by larger uncertainties in the mixing layer, and consequently, much more biases in modelled mixing ratios. To examine the effect of uncertainties in mixing heights and the growth/decay of the PBL on STILT-modelled CO_2 concentration, morning (9:00 UTC) and afternoon (21:00 UTC) data were analyzed separately. R-squared values shown in Figure 4.15 and 4.16 indicate that throughout the study period (2008-2011), the variations in the modelled CO_2 values around the mean were better explained by the observed values during afternoon periods. Also, the times series of STILT-modelled CO_2 concentrations compared against observations revealed there was stronger agreement in the afternoon data (Figure 4.26 and 4.27). Improved model simulations in the afternoon was more clearly evident at Fraserdale due to the stronger diurnal variations in biospheric surface fluxes. During the nighttime (and early morning), atmospheric CO_2 concentration increases not only because of plant respiration, but also because of CO_2 accumulation in the shallow nocturnal boundary layer. Stable atmospheric conditions develop at

night as the earth's surface cools rapidly, and thermal turbulence decreases. Accordingly, vertical mixing is suppressed and there is a buildup of CO_2 concentrations. The results of this study show that modelled atmospheric CO_2 concentrations during the night are almost consistently lower than observed values (Figure 4.26), disclosing that the nocturnal mixing height is overestimated. The deeper mixing depth causes a smaller surface flux influence, as well as the dilution of the PBL plume. The overall effect is an underestimation of the actual atmospheric CO_2 concentration. Uncertainties in mixing heights can also affect model results during the daytime, particular in summer (Figure 4.27). However, model biases are significantly larger during nighttime compared to daytime as shown in Figure 4.18 and 4.19. At Fraserdale for example, the mean model bias in 2008 was -3.93 ± 8.98 ppm for the morning data, and only -1.13 ± 5.62 ppm in the afternoon. Other studies have shown that biases in modelled CO_2 concentrations due to discrepancies in PBL mixing, could have an average uncertainty of about 40% for the daytime, and much larger values as high as 100% for nocturnal mixing layers, with bias errors greater than 50% (Gerbig et al., 2008; Mallia et al., 2015). Comparing between radiosonde-derived mixing heights and mixing heights obtained from ECMWF meteorological data during May–June 2005 in Europe, Gerbig et al. (2008) estimated that uncertainties for CO_2 mixing ratios was on average 3.5 ppm.

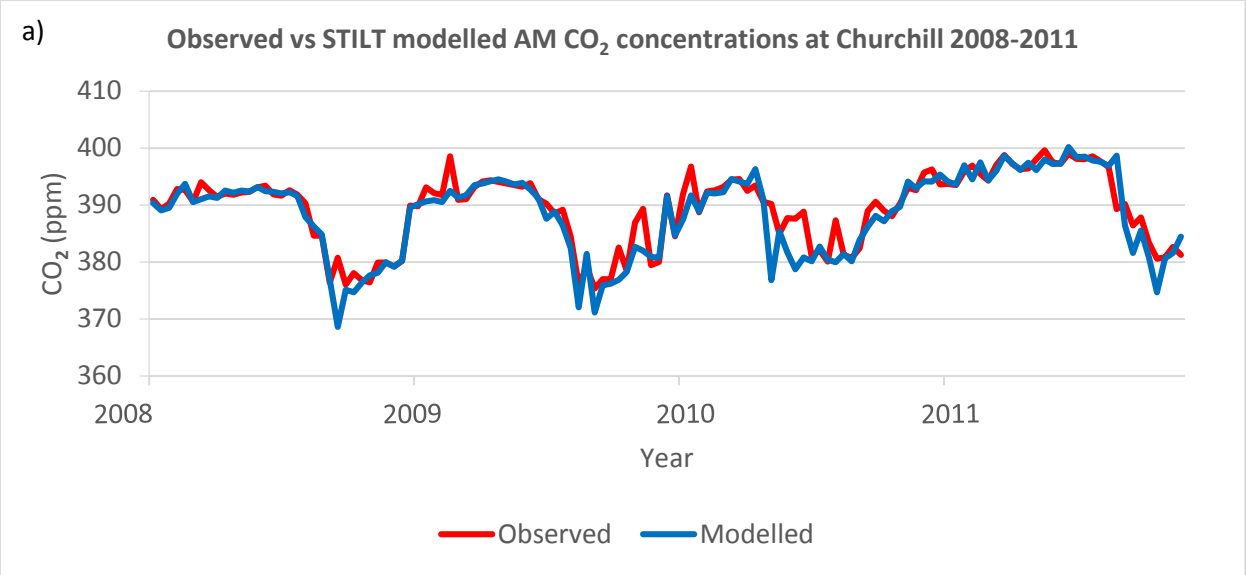

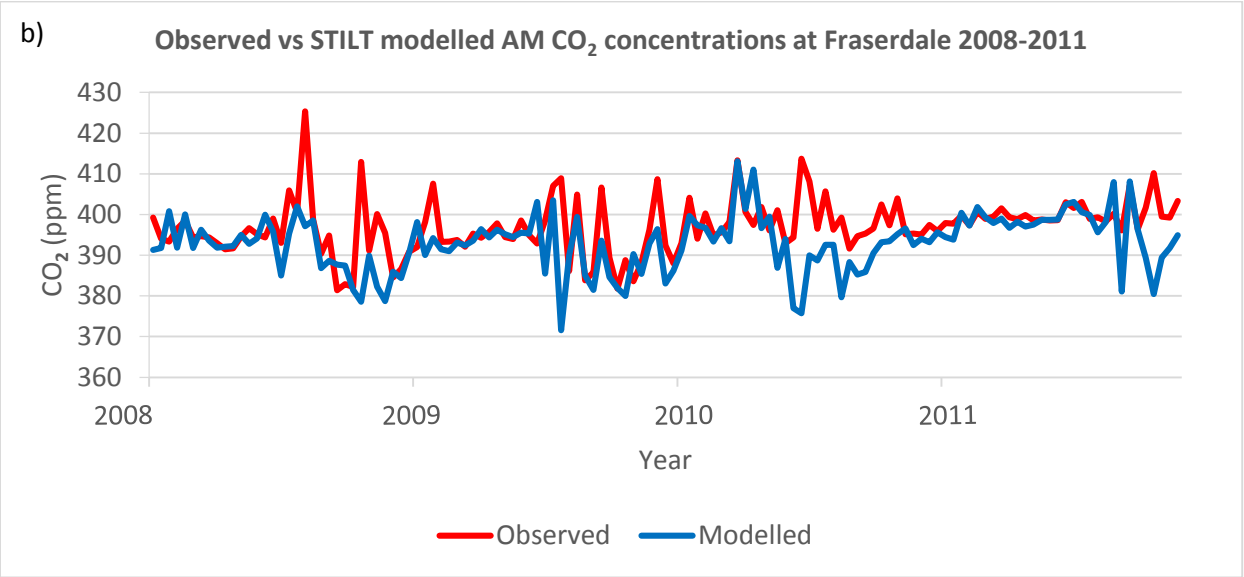

Figure 4. 26. Times series of Observed CO_2 concentrations compared against STILT-modelled CO_2, using weekly morning (9:00 UTC) data from 2008-2011. (a) Churchill. (b) Fraserdale.

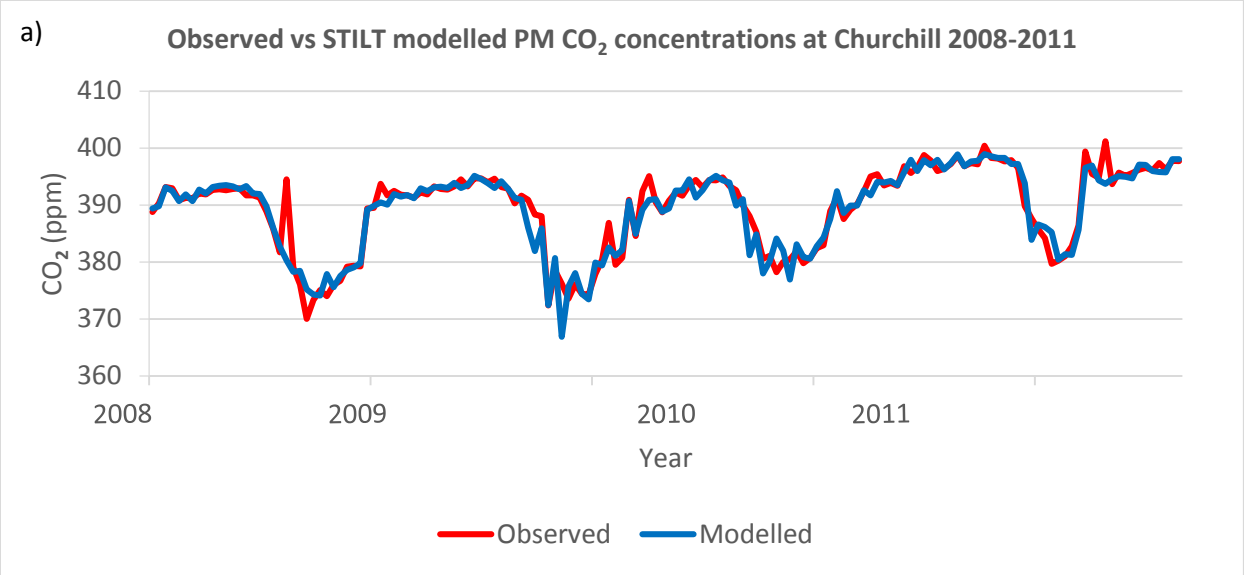

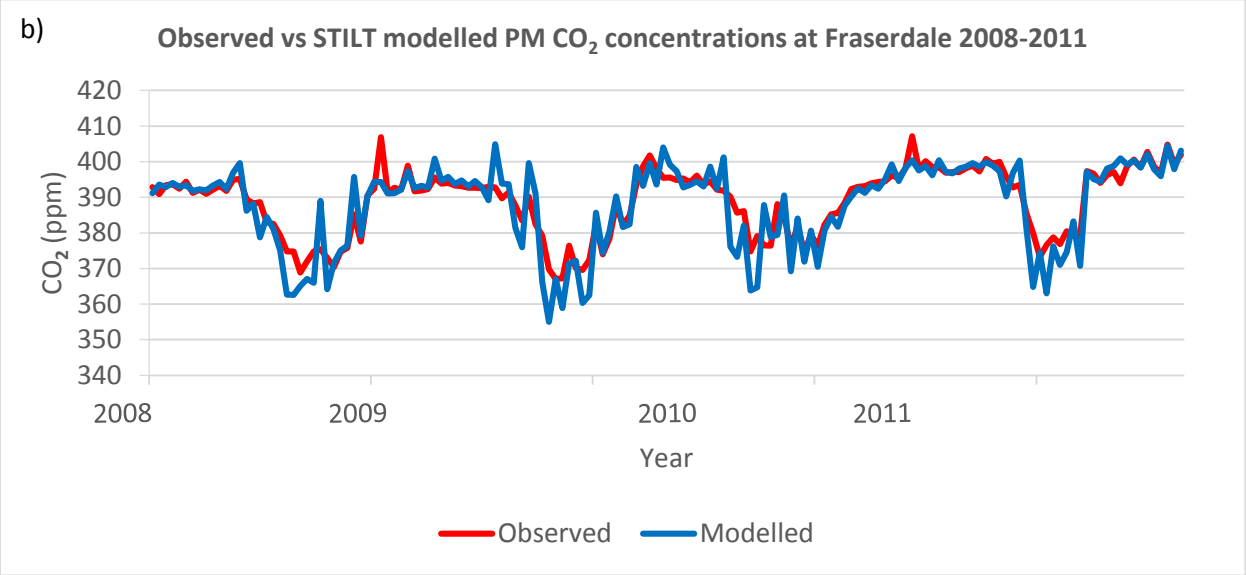

Figure 4. 27. Times series of Observed CO_2 concentrations compared against STILT-modelled CO_2, using weekly afternoon (21:00 UTC) data from 2008-2011. (a) Churchill. (b) Fraserdale.

4.3.4 Uncertainties in Surface Fluxes and Background Concentrations

A priori surface flux estimates and CO_2 mole fractions used in this study are obtained from Carbon Tracker (CT2013). The CT data assimilation framework involves forecasting atmospheric CO_2 mole fractions from a combination of CO_2 surface exchange models and an atmospheric transport model (TM5) driven by meteorological fields from the European Centre for Medium-Range Weather Forecasts (ECMWF). Subsequently, inverse modelling techniques are employed to minimize the difference between model forecasts and observations, thereby "optimizing" the magnitude of the surface fluxes (Peters et al., 2007). The CT-derived net CO_2 exchange between the terrestrial biosphere and the atmosphere may differ from actual observations. Therefore, small inconsistencies in *a priori* surface flux fields may result in considerable biases in STILT-modelled atmospheric CO_2 concentrations. To examine this potential source of error, STILT-simulated CO_2 concentrations and CT measurements are evaluated with observed CO_2 mixing ratios from the tower sites.

Smoothed curves are fitted to the 2012 data using daily afternoon values at Churchill and Fraserdale. The curve-fitting method is derived from the digital filtering procedure of Nakazawa et al. (1997). This statistical technique serves as an important tool for the quantification of several features of atmospheric CO_2 measurements, as well as the interpretation of carbon cycle dynamics. Some of the most prominent features include: (i) the presence of a seasonal cycle produced mainly by photosynthetic-decay processes of the terrestrial biosphere; (ii) an upward secular trend, produced largely by fossil fuel combustion; (iii) short-term fluctuations superimposed on the seasonal cycle, and; (iv) interannual variations in all of the above three features (Nakazawa et al., 1997).

Fitted curves to the daily afternoon data for STILT, CT, and tower observations (OBS) are shown in Figure 4.24. All three curves are in good agreement at Churchill, indicating that atmospheric CO_2 concentrations are properly calculated by both CT and STILT. There is also reasonable agreement at Fraserdale; however, the STILT curve deviates considerably from the observed values during the summer, while CT concentrations remain consistent with OBS values. This reveals that the large biases in STILT-modelled atmospheric CO_2 concentrations during summer cannot be attributed to errors in the *a priori* CT CO_2 estimates. Biases in the STILT results are more likely due to model transport errors associated with uncertainties in horizontal velocities from NARR wind fields. Figure 4.24b shows that the difference between model and observed values increases radically at the onset of the growing season when transport uncertainties and their associated errors in simulated atmospheric CO_2 are amplified in the presence of active vegetation. The maximum bias of about 5 ppm at Fraserdale in mid-July is consistent with the 5.9 ppm value reported by Lin and Gerbig (2005). This error is barely noticeable at Churchill because of the smaller vegetative influence, and a weaker spatial variability in biospheric fluxes, particularly in the near-field region.

Furthermore, comparisons of the smoothed seasonal cycles obtained for STILT, CT, and OBS daily afternoon data are shown in Figure 4.25. Here, the major objective was to examine the performance of STILT and CT based on three notable characteristics of the seasonal CO_2 cycle: (i) timing of the seasonal minimum; (ii) magnitude of the seasonal minimum, and (iii) seasonal amplitude. The disparities between the smoothed curves for Churchill is negligible, demonstrating that all three results are in good agreement with regards to the timing and magnitude of the seasonal minimum (Figure 4.25a). Also, results for the seasonal amplitude are remarkable in the agreement between STILT and observed CO_2 values (19 ppm), while CT follows closely at 21 ppm.

At Fraserdale, however, the timing of the seasonal CO_2 minimum calculated by STILT (CT) is about 16 (6) days earlier than the actual observation (Figure 4.25b). In addition, the magnitude of the seasonal minimum is -19, -16, and -15 ppm, for STILT, CT, and OBS, respectively. Assuming that model transport is perfect, STILT results should be roughly the same as the CT values. In that instance, any large biases between modelled CO_2 concentrations and observation values could be simply ascribed to inherent biases in the *a priori* CO_2 estimates obtained by STILT from CT surface flux and mole fraction fields. Thus, based on the seasonal minimum values of -19, -16, and -15 ppm, for STILT, CT, and OBS, respectively, errors due to *a priori* surface fluxes and mole fractions are about 25% (1ppm), while transport model uncertainties represent an error of about 75% (3ppm).

4.3.5 Model Transport Errors and Meteorological Inputs

It is important to note that transport model uncertainties such as errors in advection and PBL mixing are the dominant sources of uncertainty in this study. This is because, given the same surface fluxes, the modelled surface influence on the mixing ratios at the tower depends on the air parcel trajectories and footprints computed by STILT. These transport information are largely influenced by horizontal advection and vertical mixing. The offline transport simulation approach employed by STILT requires the use of profiles of temperature, humidity, and horizontal winds from the North American Regional Reanalysis (NARR). The meteorological data is used to calculate the profile of turbulent mixing within the PBL (i.e. the mixing height). Studies have shown that weather information from forecasted or analyzed meteorological fields may deviate considerably from observations (Lin and Gerbig, 2005). Further, the approach used by weather forecast/reanalysis systems in the assimilation of temperature, humidity and winds from radiosonde observations does not guarantee that the vertical profile of the atmosphere is retained. For example, the level at which an inversion occurs in the assimilated data (and thus also in forecasts) is not necessarily the level at which an inversion was observed (Gerbig et al., 2008).

Operational forecasts and reanalysis systems are also limited by their spatial and temporal resolutions (Stohl et al., 2001; Lin and Gerbig, 2005; Bowman et al., 2013). The 3-hourly NARR fields with a 32-km horizontal grid spacing used in this study may cause model transport errors due to spatial and temporal interpolation of wind fields. The coarse temporal resolution undersamples the wind field in time relative to space thereby impacting on STILT-modelled air parcel trajectories and footprints. Pisso et al. (2010) demonstrated that using customized outputs from the ECMWF model at 0.5°–1° horizontal resolution, reconstructions of stratospheric ozone profiles are significantly improved when wind field frequency is increased from 6- to 1-hourly

resolution. Similarly, Brioude et al. (2012) used meteorological inputs from a 4- and 12-km resolution mesoscale forecast, and reported that the dispersion model benefited immensely when increasing the temporal resolution from 2 h to 1 h and 30 mins. The wind fields from NARR used in this study to drive the STILT model are only available at a 3-hourly resolution, and thus, the uncertainties in the meteorological inputs have been discussed in this section.

4.3.6 The Influence of the Hudson Bay on STILT Model Performance

It was hypothesized that environmental conditions such as wind speeds and direction would have significant impact on simulated atmospheric CO_2 concentrations, since atmospheric CO_2 concentrations are modified by horizontal advection and vertical mixing, on the way to the measurement tower. The advective influence of the Hudson Bay on STILT model performance was considered. Using afternoon CO_2 data at Churchill, each trajectory and footprint map in the 2012 study period was examined to identify measurement times with a substantial Hudson Bay (offshore winds) influence. The corresponding model biases (mean differences between modelled CO_2 concentrations and observed values) were examined and compared with other measurement times without the Hudson Bay influence. The result suggests that model transport errors showed no significant difference when the winds came off the Hudson Bay (Table 4.6). Thus, there is no noticeable impact of the advective influence of the Hudson Bay on STILT-simulated atmospheric CO_2 concentrations during the 2012 study period.

t-Test: Two-Sample Assuming Unequal Variances		
	HB	*OTHERS*
Mean	-0.40706906	-0.65723017
Variance	2.48945396	6.55362723
Observations	81	201
Hypothesized Mean Difference	0	
df	234	
t Stat	0.99399409	
P(T<=t) one-tail	0.16062624	
t Critical one-tail	1.65139147	
P(T<=t) two-tail	0.32	
t Critical two-tail	1.97015364	

Table 4. 6. Statistical test to determine the advective influence of the Hudson Bay on model transport errors. The null hypothesis is that there is no significant difference in model biases when the winds came off the Hudson Bay. The alternative hypothesis is that model transport errors are exacerbated by the advective influence of the Hudson Bay. Since the p-value of the test is > 0.05, the null hypothesis is accepted.

5.0 CONCLUSIONS

5.1 Summary

Seasonal and inter-annual variability in the atmospheric concentration of greenhouse gases (GHGs) play a vital role in regulating global climate. In recent years, changes in atmospheric burden of CO_2 and other GHGs have resulted in noticeable modifications of the climate system. These statistically significant variations of the mean state of the climate or of its variability have persisted for decades, and are mainly attributed to anthropogenic emissions of CO_2. In addition, terrestrial ecosystems are responsible for significant inter-annual changes in the global growth rate of CO_2, and there are still large uncertainties in the spatial distribution and magnitude of natural carbon sources and sinks. The response (and feedback) of global ecosystems to climate changes and anthropogenic perturbations is an active area of scientific research. Interestingly, much of our understanding of the terrestrial carbon cycle comes not from direct measurements of photosynthesis and respiration by eddy covariance (EC) methods, but rather, from measurements of atmospheric CO_2 mixing ratios on continental towers and the inferred terrestrial fluxes needed to match the observations. The surface flux information retrieved from CO_2 concentrations at tower sites contain an integrated signal of CO_2 exchange representing footprint areas of 10^3–10^4 km^2. Inverse modelling and isotope analysis have recognized that temperate and boreal ecosystems in the Northern hemisphere sequester large amounts of carbon annually—as much as 2 Pg C y^{-1}.

In the Hudson Bay Lowland (HBL) region, Environment Canada's Greenhouse Gas Measurement Program coordinates a network of tower sites to monitor carbon emissions and sinks from terrestrial ecosystems. In this study, two measurement towers are employed to provide information on the carbon balance of the HBL: (1) The Churchill site, located at the northern edge of the HBL (58°45′N, 94°04′W) and on an ecotone between the Arctic tundra and the boreal forest; and (2) The Fraserdale site, located on the southern edge of the HBL and on the northern perimeter of the boreal forest at 49°52'N, 81°37'W.

Preliminary analyses were carried out to describe and explain the seasonal and inter-annual variations of atmospheric CO_2 concentration for a 5-year (2008-2012) weekly flask measurement record. Diurnal and daily patterns were examined using hourly CO_2 data for the year 2012. The seasonal cycle revealed the influence of the terrestrial biosphere on observed CO_2 mixing ratios in the region. Summertime was characterized by a net CO_2 uptake due to plant photosynthesis during the growing season, while wintertime features higher atmospheric CO_2 concentrations due to little/no terrestrial carbon sink. Similarly, CO_2 concentration values were lower during the day and higher at night. The diurnal cycle of CO_2 is produced not only by the daily cycle of the atmosphere-biosphere carbon exchange, but also by the daily evolution of the planetary boundary layer (PBL). Atmospheric CO_2 accumulation occurs at nighttime due to plant and soil respiration, as well as a weakly developed (stable) nocturnal boundary layer. Overall, Fraserdale exhibits a stronger variability in CO_2 than Churchill, particularly during the growing season. Differences in the timing, variations, and magnitude of atmospheric CO_2 concentrations over the two sites are explained in terms of their vegetation characteristics.

The Stochastic Time-Inverted Lagrangian Transport model (STILT), driven by the North American Regional Reanalysis (NARR) meteorological dataset, and coupled with the

CarbonTracker data assimilation system (CT2013), was used to simulate atmospheric concentrations of CO_2 in the Hudson Bay Lowlands. The primary objectives were to evaluate the performance of the STILT model, and to examine the accuracy of CarbonTracker surface flux estimates. Weekly CO_2 flask measurements from 2008–2011 were used for temporal analysis, and two measurement sites—Churchill and Fraserdale—were used for spatial comparison. In addition, 2012 daily afternoon CO_2 data were analyzed for a more detailed evaluation of the seasonal cycle.

STILT was run in backward mode, releasing 3000 particles (air parcels) from the measurement tower (receptor) toward upwind regions, and calculating air parcel trajectories over a period of 72 hours. Each particle was transported by both advective wind fields from NARR and turbulent velocity component represented by a Markov chain process. The footprints were obtained from the simulated trajectory information providing estimates of the surface influence region and the sensitivity of the atmospheric concentration measurement to surface fluxes. These STILT-generated footprints which are in units of ppm/μmol m^{-2} s^{-1} were averaged every 3 hours at a 1° x 1° horizontal grid resolution—the same temporal and spatial resolution as the CT CO_2 flux fields (μmol m^{-2} s^{-1}). The total surface flux contributions (ppm) to the measured mixing ratios at the receptor was computed by convolving the STILT particle footprints with known flux estimates from CT, and then averaging over the 72-h period. To compare with observations, the mixing ratio enhancements due to surface fluxes were then added to a background concentration advected from the domain boundary. The background concentrations were calculated by taking the endpoints of the 3000 particle ensemble (72 h backward in time) and interpolating them to the corresponding grid cells and their associated CO_2 concentrations. The sum of the average background concentration and the surface flux contribution constitutes the total modelled CO_2 mixing ratio at

the receptor. These model results were evaluated with observations from the Churchill and Fraserdale measurement sites.

STILT-modelled results demonstrate that the simulated atmospheric CO_2 concentrations compare reasonably against observations. The mean model bias suggested that STILT underestimated CO_2 values throughout the study period. At Churchill, the mean model bias was -0.57 ppm, while Fraserdale had a greater bias of -2.44 ppm. Smoothed seasonal curves fitted to the 2012 daily afternoon CO_2 data revealed that model bias was highest during summertime, particularly over the Fraserdale region. Overall, disparity between modelled and observed CO_2 concentrations are attributed to errors in horizontal advection and PBL mixing, as well as uncertainties in surface fluxes and background concentrations. During the growing season, model transport uncertainties due to advection lead to errors in simulated CO_2 from biogenic surface fluxes within the near-field. Such errors yielded model biases of up to 5 ppm at Fraserdale. Moreover, inadequate model representation of vertical mixing processes cause considerable biases in the simulated concentration footprints. Model errors were greater at nighttime when uncertainties in the mixing height are larger in the nocturnal boundary layer. Improved model simulations during daytime was more noticeable at Fraserdale due to the stronger vegetative influence. At Fraserdale, the mean model bias in 2008 was -3.93 ± 8.98 ppm in the morning, and only -1.13 ± 5.62 ppm in the afternoon. Furthermore, STILT-simulated CO_2 concentrations and CarbonTracker (CT) measurements were evaluated with observed CO_2 mixing ratios (OBS) to assess the uncertainties in *a priori* surface fluxes. Both STILT and CT agree well with the observations at Churchill, capturing both the maximum and minimum concentrations. At Fraserdale, the timing of the 2012 seasonal minimum suggested that STILT and CT were unable to adequately resolve the timing of the seasonal cycle, with an occurrence of about 6 (CT) to 16

(STILT) days earlier than OBS. Besides, the magnitude of the seasonal minimum varies from -15 ppm for OBS to -19 ppm for STILT, demonstrating that the STILT model overestimates terrestrial carbon sink at Fraserdale. As a result, the seasonal amplitude is about 6 ppm (2 ppm) higher for STILT (CT) than OBS.

Finally, the influence of the Hudson Bay on STILT model performance was briefly considered. The Hudson Bay has no noticeable impact on simulated atmospheric CO_2 concentrations during the 2012 study period. Model transport errors showed no significant difference when the winds came off the Hudson Bay.

5.2 Synthesis and Future Studies

Among several other objectives, the primary aim of this study was to examine the accuracy of the Stochastic Time-Inverted Lagrangian Transport (STILT) model. Atmospheric transport models play a vital role in inverse analysis, and consequently, in our understanding of the terrestrial carbon cycle. The capability of a transport model to accurately represent air parcel trajectories is largely dependent on the simulated horizontal velocities and vertical mixing in the PBL. In inversion studies, the inferred terrestrial fluxes are adjusted by minimizing the difference between observations and model predictions. This "optimization" is achieved by using a first guess of the flux component and its associated uncertainty, and tuning a set of linear scaling factors that control the magnitude of the surface fluxes. It is important to note that the quality of the optimized biospheric surface fluxes in any inverse analysis is only as good as the atmospheric transport model used. Inaccurate air parcel trajectories and/or footprint estimations will inadvertently and inevitably result in erroneous spatial distribution of surface flux estimates. The net effect is the

misinterpretation of regional carbon cycle dynamics and the magnitude of terrestrial carbon sources and sinks. Therefore, this study is a crucial first step to further inverse analysis. STILT model performance in this study has been demonstrated to Environment Canada's Climate Research Division, where rigorous studies are routinely carried out on inverse modelling of CO_2 and CH_4 across Environment Canada's greenhouse gas measurement towers. Presently, we have applied STILT to more than 8 measurement sites, comparing STILT–modelled trajectories and footprints to other Lagrangian Particle Dispersion Models (LPDMs). Inter-model comparisons offer an important opportunity to evaluate transport simulations, as well as meteorological forecast input fields.

The next step in this study will be to further investigate the influence of upwind biospheric surface flux contribution to the observed atmospheric CO_2 mixing ratios in the Hudson Bay Lowland region. This will involve a detailed analysis of air parcel trajectories and area of influence, by dividing the study region into six sectors based mainly on a combination of the seasonal wind direction patterns and *a priori* CO_2 source distribution.

Additionally, it would be interesting to apply this "receptor-oriented" analysis framework to methane (CH_4) tower measurements in the HBL. There are still large uncertainties about the CH_4 emission from this region; presently, estimates range from 0.28 to 8.5 Tg C yr^{-1}. Accordingly, there is need for more comprehensive and accurate research. This is relevant since the northern boreal wetland regions are estimated to hold half of all wetlands and soil carbon in the world (~1700 Pg C), which is twice the amount of carbon currently held in the atmosphere. More importantly, these regions are sensitive to global warming and there are concerns about the possible emissions of CH_4 from changing wetlands and thawing permafrost.

REFERENCES

Ahmadov, R., Gerbig, C., Kretschmer, R., Koerner, S., Neininger, B., Dolman, A. J., and Sarrat, C. (2007). Mesoscale covariance of transport and CO_2 fluxes: Evidence from observations and simulations using the WRF-VPRM coupled atmosphere-biosphere model. J. Geophys. Res., 112, D22107, doi:10.1029/2007JD008552.

Ahmadov, R., Gerbig, C., Kretschmer, R., Körner, S., Rödenbeck, C., Bousquet, P., & Ramonet, M. (2009). Comparing high resolution WRF-VPRM simulations and two global CO_2 transport models with coastal tower measurements of CO_2. Biogeosciences, 6(5), 807-817.

Ahrens C. D., (2009). Meteorology Today: An Introduction to Weather, Climate, and the Environment. The 9th edition, Pearson Prentice Hall, Brooks/Cole, Thomson Learning, USA, 549 pp.

Allen, C., et al., 2010: A global overview of drought and heat-induced tree mortality reveals emerging climate change risks for forests. Forest Ecol. Manage., 259, 660–684.

Bakwin, P. S., Davis, K. J., Yi, C., Wofsy, S. C., Munger, J. W., Haszpra, L., & Barcza, Z. (2004). Regional carbon dioxide fluxes from mixing ratio data. Tellus B, 56(4), 301-311.

Bakwin, P. S., Tans, P. P., Hurst, D. F. and Zhao, C. (1998). Measurements of carbon dioxide on very tall towers: results of the NOAA/CMDL program. Tellus 50B, 401–415.

Bakwin, P. S., Zhao, C., Ussler, III, W., Tans, P. P. and Quesnell, E. (1995). Measurements of carbon dioxide on a very tall tower. Tellus 47B, 535–549.

Barkhatov, Y. V., Belolipetsky, P. V., Degermendzhi, A. G., Belolipetskii, V. M., Verkhovets, S. V., Timokhina, A. V., ... & Trephilova, O. V. (2012). Modeling of CO_2 fluxes between atmosphere and boreal forest. Procedia Environmental Sciences, 13, 621-625.

Bergamaschi, P., et al. (2007). Satellite chartography of atmospheric methane from SCIAMACHY on board ENVISAT: 2. Evaluation based on inverse model simulations, J. Geophys. Res., 112, D02304, doi:10.1029/2006JD007268.

Boden, T. A., Marland, G., and Andres, R. J. (2013) Global, Regional, and National Fossil-Fuel CO_2 Emissions. Carbon Dioxide Information Analysis Center, Oak Ridge National Laboratory, U.S. Department of Energy, Oak Ridge, Tenn., U.S.A. doi 10.3334/CDIAC/00001_V2013.

Bohren, C. F., and Albrecht B. A. (1998). Atmospheric Thermodynamics, *Oxford Univ. Press, New York*.

Bousquet, P., Ciais, P., Peylin, P., Ramonet, M., & Monfray, P. (1999). Inverse modeling of annual atmospheric CO_2 sources and sinks: 1. Method and control inversion. Journal of Geophysical Research: Atmospheres (1984–2012), 104 (D21), 26161-26178.

Bouwman, A. F., van der Hoek, K. W., and Olivier, J. G. J. (1995). Uncertainties in the global source distribution of N2O, J. Geophys. Res., 100(D2), 2785– 2800.

Bowman, K. P., Lin, J. C., Stohl, A., Draxler, R., Konopka, P., Andrews, A., & Brunner, D. (2013). Input data requirements for Lagrangian trajectory models. Bulletin of the American Meteorological Society, 94(7), 1051-1058.

Brandt, J.P.; Flannigan, M.D.; Maynard, D.G.; Thompson, I.D.; Volney, W.J.A. (2013), An introduction to Canada's boreal zone: ecosystem processes, health, sustainability, and environmental issues, Environmental Reviews 21(4), 207-226.

Brioude, J., Angevine, W. M., McKeen, S. A., and Hsie, E.-Y. (2012). Numerical uncertainty at mesoscale in a Lagrangian model in complex terrain. Geosci. Model Dev. Discuss., 5, 967–991.

Bryson, R. A. (1966) Air masses, streamlines, and the boreal forest. Geogr. Bull. 4, 228–269.

Burden, F. R., Foerstner, U., McKelvie, I. D., Guenther, A. (2002). Environmental Monitoring Handbook. TRACE GAS EMISSION MEASUREMENTS, Chapter, McGraw-Hill Professional, AccessEngineering.

Byers, H. R. (1974). General Meteorology, 4th Edn. McGraw-Hill, New York, U.S.A.

Caspersen, J. P., et al. (2001), Contributions of land-use history to carbon accumulation in U.S. forests, Science, 290, 1148– 1151.

Chan, D., Yuen, C. W., Higuchi, K., Shashkov, A., Liu, J., Chen, J., & Worthy, D. (2004). On the CO_2 exchange between the atmosphere and the biosphere: the role of synoptic and mesoscale processes. Tellus B, 56(3), 194-212.

Chapin, F.S., III, Sturm, M., Serreze, M.C., McFadden, J.P., Key, J.R., Lloyd, A.H., McGuire, A.D., Rupp, T.S., Lynch, A.H., Schimel, J.P., Beringer, J., Chapman, W.L., Epstein, H.E., Euskirchen, E.S., Hinzman, L.D., Jia, G., Ping, C.-L., Tape, K.D., Thompson, C.D.C., Walker, D.A., and Welker, J.M. (2005). Role of land-surface changes in Arctic summer warming. Science, 310: 657–660. doi:10.1126/science.1117368. PMID:16179434.

Chen, B., Chen, J. M., & Worthy, D. E. (2005). Interannual variability in the atmospheric CO_2 rectification over a boreal forest region. Journal of Geophysical Research: Atmospheres (1984–2012), 110(D16).

Chen, B., J. M. Chen, P. P. Tans, and L. Huang (2006a), Modeling dynamics of stable carbon isotopic exchange between a boreal ecosystem and the atmosphere, Global Change Biol., 12, 1842– 1867.

Chen, B., J. M. Chen, L. Huang, and P. P. Tans (2006b), Simulating dynamics of d13C of CO_2 in the planetary boundary layer over a boreal forest region: Covariation between surface fluxes and atmospheric mixing, Tellus, Ser. B, 58, 537–549.

Chen, B., Chen, J. M., Mo, G., Black, T. A., & Worthy, D. E. (2008). Comparison of regional carbon flux estimates from CO_2 concentration measurements and remote sensing based footprint integration. Global Biogeochemical Cycles, 22(2).

Chen, J. M., Ju, W., Cihlar, J., Price, D., Liu, J., Chen, W., ... & Barr, A. (2003). Spatial distribution of carbon sources and sinks in Canada's forests. Tellus B, 55(2), 622-641.

Chen, J. M., Chen, B., Higuchi, K., Liu, J., Chan, D., Worthy, D., ... & Black, A. (2006). Boreal ecosystems sequestered more carbon in warmer years. Geophysical research letters, 33(10).

Chen, J. M., Chen, B., & Tans, P. (2007). Deriving daily carbon fluxes from hourly CO_2 mixing ratios measured on the WLEF tall tower: An upscaling methodology. Journal of Geophysical Research: Biogeosciences (2005–2012), 112(G1).

Ciais, P., Tans, P. P., Trolier, M., White, J. W. C. and Francey, R. J. (1995). A large northern hemisphere terrestrial CO_2 sink indicated by $^{13}C/^{12}C$ of atmospheric CO_2. Science 269, 1098–1102.

Conway, T. J., Tans, P. P., Waterman, L. S., Thoning, K. W., Kitzis, D. W., Masarie, K. A. and Zhang, N. (1994). Evidence for interannual variability of the carbon cycle from the National Oceanic and Atmospheric Administration/Climate Monitoring and Diagnostics Laboratory Global Air Sampling Network. J. Geophys. Res. 99, 22, 831–22, 855 (data update available from www.cmdl.noaa.gov/ccgg/).

Cotton, W. R., Alexander, G. D., Hertenstein, R., Walko, R. L., McAnelly, R. L., Nicholls, M. (1995) Cloud venting—A review and some new global annual estimates. Earth Sci. Rev., 39, 169–206.

Crevoisier, C., Gloor, M., Gloaguen, E., Horowitz, L. W., Sarmiento, J. L., Sweeney, C., & Tans, P. P. (2006). A direct carbon budgeting approach to infer carbon sources and sinks. Design and synthetic application to complement the NACP observation network. Tellus B, 58(5), 366-375.

D'Abreton, P. C. and Tyson, P. D. (1996). Three-dimensional kinematic trajectory modelling of water vapour transport over Southern Africa. Water SA 22, 297-306.

De Bruin, H. A. R. (1983), A model for the Priestley-Taylor parameter, a, J. Clim. Appl. Meteorol., 22, 572– 578.

Denmead, O. T.,M. R. Raupach, F. X. Dunin, H. A. Cleugh, and R. Leuning (1996), Boundary layer budgets for regional estimates of scalar fluxes, Global Change Biol., 2, 255– 264.

Denning, A. S. (1994). Investigations of the transport, sources, and sinks of atmospheric CO_2 using a general circulation model. Doctoral thesis, Atmospheric Science Paper No. 564, Department of Atmospheric Science, Colorado State University, 336 pp.

Denning, A. S., Collatz, J. G., Zhang, C., Randall, D. A., Berry, J. A., et al., (1996a). Simulations of terrestrial carbon metabolism and atmospheric CO_2 in a general circulation model. Part 1: Surface carbon fluxes. Tellus 48B, 521–542.

Denning, A. S., I. Y. Fung, and D. Randall (1995), Latitudinal gradient of atmospheric CO_2 due to seasonal exchange with land biota, Nature, 376, 240–243.

Denning, A. S., Randall, D. A., Collatz, G. J. and Sellers, P. J. (1996b). Simulations of terrestrial carbon metabolism and atmospheric CO_2 in a general circulation model. Part 2: Spatial and temporal variations of atmospheric CO_2. Tellus 48B, 543–567.

Draxler, R. R. and Hess, G. D. (1998). An overview of the HYSPLIT_4 modeling system for trajectories, dispersion, and deposition. Aust. Meteorol. Mag., 47, 295– 308.

Dredge, L. A. (1992). Field Guide to the Churchill Region, Manitoba: Glaciations, sea level changes, permafrost landforms, and archaeology of the Churchill and Gillam areas, Geological Survey of Canada Miscellaneous Report 53.

Dutton, J. A. (1986). The Ceaseless Wind. An Introduction to the Theory of Atmospheric Motion. Dover, New York.

Ecological Stratification Working Group (1995). A National Ecological Framework for Canada. Agriculture and Agri-Food Canada, Research Branch, Centre for Land and Biological Resources Research and Environment Canada, State of the Environment Directorate, Ecozone Analysis Branch, Ottawa/Hull. Report and national map at 1:7500 000 scale.

Eliassen, A., Hov, O., Isaksen, I. S. A., Saltbones, J., and Stordal, F. (1982). A Lagrangian long-range transport model with atmospheric boundary layer chemistry, *J. Appl. Meteorol., 21, 1645–1661*.

Enting, I. G. (1999). Characterising the temporal validity of the global carbon cycle, Tech. Pap. 40, CSIRO Atmos. Res., Hobart, Tasmania, Australia.

Enting, I. G., Trudinger, C. M., & Francey, R. J. (1995). A synthesis inversion of the concentration and δ13 C of atmospheric CO_2. Tellus B, 47(1-2), 35-52.

Fan, S., Gloor, M., Mahlman, J., Pacala, S., Sarmiento, J., Takahashi, T., & Tans, P. (1998). A large terrestrial carbon sink in North America implied by atmospheric and oceanic carbon dioxide data and models. Science, 282(5388), 442-446.

Field, C. B., and I. Y. Fung (1999). The not-so-big U.S. carbon sink, Science, 285, 544– 545.

Fitzjarrald, D. R. (2002), Boundary layer budgeting, in Vegetation, Water, Humans and the Climate: A New Perspective on an Interactive System, edited by P. Kabat et al., pp. 239–254, Springer-Verlag, New York.

Foley, J.A. (2005). Tipping points in the tundra. Science, 3100: 627–628. doi:10.1126/science.1120104.

Francey, R., C. E. Allison, I. G. Enting, J. W. C. White, M. Trolier, and P. P. Tans (1995), Changes in the oceanic and terrestrial carbon uptake since 1982, Nature, 373, 326– 330.

Friedlingstein, P., J. L. Dufresne, P. M. Cox, and P. Rayner (2003), How positive is the feedback between climate change and the carbon cycle?, Tellus, Ser. B, 55, 692– 700.

Friedlingstein, P., Müller, J. F., & Brasseur, G. P. (1994). Sensitivity of the terrestrial biosphere to climatic changes: Impact on the carbon cycle. Environmental pollution, 83(1), 143-147.

Fung, I. Y., K. Prentice, E. Matthews, J. Lerner, and G. Russell (1983), Three-dimensional tracer model study of atmospheric CO_2: Response to seasonal exchanges with the terrestrial biosphere, J. Geophys. Res., 88, 1281–1294.

Fung, I. Y., S. C. Doney, K. Lindsay, and J. John (2005), Evolution of carbon sinks in a changing climate, Proc. Nat. Acad. Sci., 102, 11,201–11, 206.

Gagnon, A. S., and Gough, W. A. (2005a) Climate change scenerios for the Hudson Bay region: An intermodel comaprison. Climatic Change 69, 269-297.

Gagnon, A. S., and Gough, W. A. (2005b) Trends in the dates of ice freeze-up and breakup over Hudson Bay, Canada. Arctic 58(4), 370-382.

Gerbig, C., Lin, J. C., Wofsy, S. C., Daube, B. C., Andrews, A. E., Stephens, B. B., ... & Grainger, C. A. (2003a). Toward constraining regional-scale fluxes of CO_2 with atmospheric observations over a continent: 1. Observed spatial variability from airborne platforms. Journal of Geophysical Research: Atmospheres (1984–2012), 108(D24).

Gerbig, C., Lin, J. C., Wofsy, S. C., Daube, B. C., Andrews, A. E., Stephens, B. B., ... & Grainger, C. A. (2003b). Toward constraining regional-scale fluxes of CO_2 with atmospheric observations over a continent: 2. Analysis of COBRA data using a receptor-oriented framework. Journal of Geophysical Research: Atmospheres (1984–2012), 108(D24).

Gerbig, C., Lin, J. C., Munger, J. W., & Wofsy, S. C. (2006). What can tracer observations in the continental boundary layer tell us about surface-atmosphere fluxes? Atmospheric Chemistry and Physics, 6(2), 539-554.

Gerbig, C., Körner, S., & Lin, J. C. (2008). Vertical mixing in atmospheric tracer transport models: error characterization and propagation. Atmospheric Chemistry and Physics, 8(3), 591-602.

Gerbig C. (2012). Applications of Lagrangian Modelling: Greenhouse Gases–Overview, in *Lagrangian Modeling of the Atmosphere, Geophys. Monogr. Ser., Vol. 200, Amer. Geophys. Union*, 349 pp, doi:10.1029/2012GM001420.

Gloor, M., Fan, S. M., Pacala, S., Sarmiento, J., & Ramonet, M. (1999). A model-based evaluation of inversions of atmospheric transport, using annual mean mixing ratios, as a tool to monitor fluxes of nonreactive trace substances like CO_2 on a continental scale. Journal of Geophysical Research: Atmospheres (1984–2012), 104(D12), 14245-14260.

Gloor, M., Bakwin, P., Hurst, D., Lock, L., Draxler, R., & Tans, P. (2001). What is the concentration footprint of a tall tower?. Journal of Geophysical Research: Atmospheres (1984–2012), 106(D16), 17831-17840.

Glooschenko, W. A., Roulet, N. T., Barrie, L. A., Schiff, H. I., & McAdie, H. G. (1994). The northern wetlands study (NOWES): An overview. Journal of Geophysical Research: Atmospheres (1984–2012), 99(D1), 1423-1428.

Gough, W. A. and Leung, A. (2002). Nature and fate of Hudson Bay permafrost, Reg. Environ. Change 2, 177–184.

Gourdji, S. M., Hirsch, A. I., Mueller, K. L., Yadav, V., Andrews, A. E., & Michalak, A. M. (2010). Regional-scale geostatistical inverse modeling of North American CO 2 fluxes: a synthetic data study. Atmospheric Chemistry and Physics, 10(13), 6151-6167.

Gourdji, Sharon M et al. (2013). North American CO_2 exchange: Inter comparison of modeled estimates with results from a fine-scale atmospheric inversion. Biogeosciences, 9(1), 457-475.

Gurney, K. R., Law, R. M., Denning, A. S., Rayner, P. J., Baker, D., Bousquet, P., ... & Yuen, C. W. (2002). Towards robust regional estimates of CO_2 sources and sinks using atmospheric transport models. Nature, 415(6872), 626-630.

Haertel, P. (2012). A Lagrangian method for simulating geophysical fluids, in *Lagrangian Modeling of the Atmosphere, Geophys. Monogr. Ser., Vol. 200, Amer. Geophys. Union*, 349 pp, doi:10.1029/2012GM001250.

Haszpra, L. (1999). On the representativeness of carbon dioxide measurements. Journal of Geophysical Research: Atmospheres (1984–2012), 104(D21), 26953-26960.

Haszpra, L., Barcza, Z., Bakwin, P. S., Berger, B. W., Davis, K. J., & Weidinger, T. (2001). Measuring system for the long-term monitoring of biosphere/atmosphere exchange of carbon dioxide. Journal of Geophysical Research: Atmospheres (1984–2012), 106(D3), 3057-3069.

Hegarty, J., Draxler, R. R., Stein, A. F., Brioude, J., Mountain, M., Eluszkiewicz, J., ... & Andrews, A. (2013). Evaluation of Lagrangian particle dispersion models with measurements from controlled tracer releases. Journal of Applied Meteorology and Climatology, 52(12), 2623-2637.

Heimann, M., & Reichstein, M. (2008). Terrestrial ecosystem carbon dynamics and climate feedbacks. Nature, 451(7176), 289-292.

Helliker, B. R., Berry, J. A., Betts, A. K., Bakwin, P. S., Davis, K. J., Denning, A. S., ... & Ricciuto, D. M. (2004). Estimates of net CO_2 flux by application of equilibrium boundary layer concepts to CO_2 and water vapor measurements from a tall tower. Journal of Geophysical Research: Atmospheres (1984–2012), 109(D20).

Higuchi, K., Worthy, D., Chan, D., & Shashkov, A. (2003). Regional source/sink impact on the diurnal, seasonal and inter-annual variations in atmospheric CO_2 at a boreal forest site in Canada. Tellus B, 55(2), 115-125.

Holland, S. (1992) Methane emission in a subarctic wetland environment, M.Sc. Thesis Department of Geography, McMaster University, Hamilton, Ontario, 108 pp, 1992.

Horst, T. W., & Weil, J. (1992). Footprint estimation for scalar flux measurements in the atmospheric surface layer. Boundary-Layer Meteorology, 59(3), 279-296.

IPCC, 2001: Climate Change 2001: The Scientific Basis. Contribution of Working Group I to the Third Assessment Report of the Intergovernmental Panel on Climate Change [Houghton, J.T., Y. Ding, D.J. Griggs, M. Noguer, P.J. van der Linden, X. Dai, K. Maskell, and C.A. Johnson (eds.)]. Cambridge University Press, Cambridge, United Kingdom and New York, NY, USA, 881pp.

IPCC, 2013: Climate Change 2013: The Physical Science Basis. Contribution of Working Group I to the Fifth Assessment Report of the Intergovernmental Panel on Climate Change [Stocker, T.F., D. Qin, G.-K. Plattner, M. Tignor, S.K. Allen, J. Boschung, A. Nauels, Y. Xia, V. Bex and P.M. Midgley (eds.)]. Cambridge University Press, Cambridge, United Kingdom and New York, NY, USA, 1535 pp, doi:10.1017/CBO9781107415324.

IPCC, (2014a). Climate Change 2014: Impacts, Adaptation, and Vulnerability. Part A: Global and Sectoral Aspects. Contribution of Working Group II to the Fifth Assessment Report of the Intergovernmental Panel on Climate Change [Field, C.B., V.R. Barros, D.J. Dokken, K.J. Mach, M.D. Mastrandrea, T.E. Bilir, M. Chatterjee, K.L. Ebi, Y.O. Estrada, R.C. Genova, B. Girma, E.S. Kissel, A.N. Levy, S. MacCracken, P.R. Mastrandrea, and L.L. White (eds.)]. Cambridge University Press, Cambridge, United Kingdom and New York, NY, USA, 1132 pp.

IPCC, (2014b). Climate Change 2014: Impacts, Adaptation, and Vulnerability. Part B: Regional Aspects. Contribution of Working Group II to the Fifth Assessment Report of the Intergovernmental Panel on Climate Change [Barros, V.R., C.B. Field, D.J. Dokken, M.D. Mastrandrea, K.J. Mach, T.E. Bilir, M. Chatterjee, K.L. Ebi, Y.O. Estrada, R.C. Genova, B. Girma, E.S. Kissel, A.N. Levy, S. MacCracken, P.R. Mastrandrea, and L.L. White (eds.)]. Cambridge University Press, Cambridge, United Kingdom and New York, NY, USA, 688 pp.

Jacob, D. J. (1999). Introduction to Atmospheric Chemistry, Princeton Univ. Press, Princeton.

Jobson, B. T., Wu, Z., Niki, H., and Barrie, L. A. (1994). Seasonal trends of isoprene, C2-C5 alkanes, and acetylene at a remote boreal site in Canada. J. Geophys. Res. 99, 1589–1599.

Johnson, K. L. (1987) Wildflowers of Churchill. Winnipeg: Manitoba Museum of Man and Nature.

Jones, A., Thomson, D., Hort, M., and Devenish, B. (2007). The U.K. Met Office's Next-Generation atmospheric dispersion model, NAME III. Air Pollution Modeling and its Application XVII, C. Borrego and A.-L. Norman, Eds., Springer, 580–589.

Kalnay, E., and Coauthors, (1996) The NCEP/NCAR 40-Year Reanalysis Project. Bull. Amer. Meteor. Soc., 77, 437–471.

Kaminski, T., Rayner, P. J., Heimann, M., & Enting, I. G. (2001). On aggregation errors in atmospheric transport inversions. Journal of Geophysical Research, 105, 4703-4715.

Kanamitsu, M., and Coauthors, (2002) NCEP/DOE AMIP-II Reanalysis (R-2). Bull. Amer. Meteor. Soc., 83, 1631–1643.

Keeling, C. D., Bacastow, R. B., Bain-Bridge, A. E., Ekdahl, C. A., Jr., Guenther, P. R. and co-authors (1976). Atmospheric carbon dioxide variations at Mauna Loa Observatory, Hawaii. Tellus 28, 538–551.

Keeling , C. D., Bacastow, R. B., Carter, A. F., Piper, S. C., Whorf, T. P., Heimann, M., Mook, W.G. and Roeloffzen, H. (1989). A three-dimensional model of atmospheric CO_2 transport based on observed winds (1). Analysis of observational data. In: Aspects of Climate Variability in the Pacific and Western Americas. Geophys. Monogr. Ser. 55 (ed D. H. Peterson). Washington, DC, 165-236.

Keeling, C. D., T. P. Whorf, M. Whalen, and J. van der Plicht (1995). Interannual extremes in the rate of rise of atmospheric carbon dioxide since 1980, Nature, 375, 666– 670.

Keeling, C. D., Chin, J. F. S., and Whorf, T. P. (1996). Increased activity of northern vegetation inferred from atmospheric CO_2 measurements. Nature, 382, 146–149.

Keller, C. A., Hill, M., Vollmer, M. K., Henne, S., Brunner, D., Reimann, S., O'Doherty, S., Arduini, J., Maione, M., Ferenczi, Z., Haszpra, L., Manning, A. J., Peter, T. (2012). European Emission of Halogenated Greenhouse Gases Inferred from Atmospheric Measurements. Environ. Sci. Technol. 2012, 46, 217– 225, doi:10.1021/es202453j.

Kistler, R., and Coauthors, (2001) The NCEP–NCAR 50-Year Reanalysis: Monthly means CD-ROM and documentation. Bull. Amer. Meteor. Soc., 82, 247–267.

Konopka, P., Ploeger, F., and Müller, R. (2012). Entropy-based and static stability–based Lagrangian grids, in *Lagrangian Modeling of the Atmosphere, Geophys. Monogr. Ser., Vol. 200, Amer. Geophys. Union*, 349 pp, doi:10.1029/2012GM001253.

Kort, E. A., Eluszkiewicz, J., Stephens, B. B., Miller, J. B., Gerbig, C., Nehrkorn, T., ... & Wofsy, S. C. (2008). Emissions of CH4 and N2O over the United States and Canada based on a receptor-oriented modeling framework and COBRA-NA atmospheric observations. Geophysical Research Letters, 35(18).

Kort, E.A., Andrews, A. E., Dlugokencky, E., Sweeney, C., Hirsch, A., Eluszkiewicz, J., Nehrkorn, T., Michalak, A., Stephens, B., Gerbig, C., Miller, J. B., Kaplan, J., Houweling, S., Daube, B. C., Tans, P., and Wofsy, S. C. (2010). Atmospheric constraints on 2004 emissions of methane and nitrous oxide in North America from atmospheric measurements and receptor-oriented modeling framework. J. Integr. Environ. Sci., 7:2, 125–133.

Kou, X., Zhang, M., Peng, Z., & Wang, Y. (2015). Assessment of the biospheric contribution to surface atmospheric CO_2 concentrations over East Asia with a regional chemical transport model. Advances in Atmospheric Sciences, 32(3), 287-300.

Kretschmer, R., Koch, F.-T., Feist, D. G., Biavati, G., Karstens, U., and Gerbig, C. (2012). Toward assimilation of observation-derived mixing heights to improve atmospheric tracer transport models, in *Lagrangian Modeling of the Atmosphere, Geophys. Monogr. Ser., Vol. 200, Amer. Geophys. Union*, 349 pp, doi:10.1029/2012GM001255, this volume.

Kuck, L. R., et al. (2000), Measurements of landscape-scale fluxes of carbon dioxide in the Peruvian Amazon by vertical profiling through the atmospheric boundary layer, J. Geophys. Res., 105(D17), 2137 – 2146.

Kurz, W.A.; Shaw, C.H.; Boisvenue, C.; Stinson, G.; Metsaranta, J.; Leckie, D.; Dyk, A.; Smyth, C.; Neilson, E.T. (2013). Carbon in Canada's boreal forest — A synthesis. Environmental Reviews 21(4), 260-292.

LAI, C. T., Schauer, A. J., Owensby, C., Ham, J. M., Helliker, B., Tans, P. P., & Ehleringer, J. R. (2006). Regional CO_2 fluxes inferred from mixing ratio measurements: estimates from flask air samples in central Kansas, USA. Tellus B, 58(5), 523-536.

Law, B. E., Falge, E., Gu, L. V., Baldocchi, D. D., Bakwin, P., Berbigier, P., ... & Wofsy, S. (2002). Environmental controls over carbon dioxide and water vapor exchange of terrestrial vegetation. Agricultural and Forest Meteorology, 113(1), 97-120.

Lemprière, T.C., Kurz, W.A., Hogg, E.H., Schmoll, C., Rampley, G.J., Yemshanov, D., McKenney, D.W., Gilsenan, R., Bhatti, J.S., Beatch, A., and Krcmar, E. (2013). Canadian boreal forests and climate change mitigation. Environ. Rev. 21(4): 293-321, 10.1139/er-2013-0039.

Lenton, T. M., H. Held, E. Kriegler, J. W. Hall, W. Lucht, S. Rahmstorf, and H. J. Schellnhuber, 2008: Tipping elements in the Earth's climate system. Proc. Natl. Acad. Sci. U.S.A., 105, 1786–1793.

Levy, P. E., A. Grelle, A. Lindroth, M. Molder, P. G. Jarvis, B. Kruijt, and J. B. Moncrieff (1999), Regional-scale CO_2 fluxes over central Sweden by a boundary layer budget method, Agric. For. Meteorol., 99, 169– 180.

Lin J. C. (2012). Lagrangian Modeling of the Atmosphere: An Introduction, in *Lagrangian Modeling of the Atmosphere, Geophys. Monogr. Ser., Vol. 200, Amer. Geophys. Union*, 349 pp, doi:10.1029/2012GM001355.

Lin, J. C. and Gerbig, C. (2005). Accounting for the effect of transport errors on tracer inversions, Geophys. Res. Lett., 32(1), L01802, doi:10.1029/2004GL021127.

Lin, J. C., Gerbig, C., Daube, B. C., Wofsy, S. C., Andrews, A. E., Vay, S. A., & Anderson, B. E. (2004a). An empirical analysis of the spatial variability of atmospheric CO_2: Implications for inverse analyses and space-borne sensors. Geophysical research letters, 31(23).

Lin, J. C., Gerbig, C., Wofsy, S. C., Andrews, A. E., Daube, B. C., Davis, K. J., & Grainger, C. A. (2003). A near-field tool for simulating the upstream influence of atmospheric observations: The Stochastic Time-Inverted Lagrangian Transport (STILT) model. Journal of Geophysical Research: Atmospheres (1984–2012), 108(D16).

Lin, J. C., Gerbig, C., Wofsy, S. C., Andrews, A. E., Daube, B. C., Grainger, C. A., ... & Hollinger, D. Y. (2004b). Measuring fluxes of trace gases at regional scales by Lagrangian observations: Application to the CO_2 Budget and Rectification Airborne (COBRA) study. Journal of Geophysical Research: Atmospheres (1984–2012), 109(D15).

Lin, J. C., Gerbig, C., Wofsy, S. C., Daube, B. C., Matross, D. M., Chow, V. Y., ... & Munger, J. W. (2006). What have we learned from intensive atmospheric sampling field programmes of CO_2?. Tellus B, 58(5), 331-343.

Lloyd, J., et al. (2001), Vertical profiles, boundary layer budgets, and regional flux estimates for CO_2 and its 13C/12C ratio and for water vapor above a forest/bog mosaic in central Siberia, Global Biogeochem. Cycles, 15(2), 267–284.

Mallia, D. V., Lin, J. C., Urbanski, S., Ehleringer, J., & Nehrkorn, T. (2015). Impacts of upwind wildfire emissions on CO, CO_2, and PM2. 5 concentrations in Salt Lake City, Utah. Journal of Geophysical Research: Atmospheres, 120(1), 147-166.

Markham, W. E. (1986). The ice cover, in Martini, I. P. (ed.), Canadian Inland Seas. Elsevier, Amsterdam.

Marshall, I. B., Schut, P. H., and Ballard, M. (1999). A National Ecological Framework for Canada: Attribute Data. Agriculture and Agri-Food Canada, Research Branch, Centre for Land and Biological Resources Research, and Environment Canada, State of the Environment Directorate, Ecozone Analysis Branch, Ottawa/Hull.

Masarie, K. A., & Tans, P. P. (1995). Extension and integration of atmospheric carbon dioxide data into a globally consistent measurement record. Journal of Geophysical Research: Atmospheres (1984–2012), 100(D6), 11593-11610.

Matross, D. M., Andrews, A., Pathmathevan, M., Gerbig, C., Lin, J. C., Wofsy, S. C., ... & Hollinger, D. Y. (2006). Estimating regional carbon exchange in New England and Quebec by combining atmospheric, ground-based and satellite data. Tellus B, 58(5), 344-358.

Maxwell, J. B. (1986a) The ice cover, in Martini, I. P. (ed.), Canadian Inland Seas. Elsevier, Amsterdam.

Maxwell, J. B. (1986b) A climate overview of the Canadian inland seas, in Martini, I. P. (ed.), Canadian Inland Seas. Elsevier, Amsterdam.

Mclaughlin Jim and Webster Kara (2014). Effects of Climate Change on Peatlands in the Far North of Ontario, Canada: A Synthesis, *Arctic, Antarctic, and Alpine Research, Vol. 46(1)*, 84–102, doi:10.1657/1938-4246-46.1.84.

McNaughton, K. G., and T. W. Spriggs (1986), A mixed-layer model for regional evaporation, Boundary Layer Meteorol., 34, 243–262.

Meehl, G.A., Stocker, T.F., Collins, W.D., Friedlingstein, P., Gaye, A.T., Gregory, J.M., Kitoh, A., Knutti, R., Murphy, J.M., Noda, A., Raper, S.C.B., Watterson, I.G., Weaver, A.J., and Zhao, Z.-C. (2007). Global climate projections [online]. In Climate change 2007: The physical science basis. Contribution of Working Group I to the Fourth Assessment Report of the Intergovernmental Panel on Climate Change. Edited by S. Solomon, D. Qin, M. Manning, Z. Chen, M. Marquis, K.B. Averyt, M.Tignor, and H.L. Miller. Cambridge University Press, Cambridge and New York. pp. 748–845. Available from http://www.ipcc.ch/pdf/assessment-report/ar4/wg1/ar4-wg1-chapter10.pdf.

Mesinger, F., et al. (2006) North American regional reanalysis, Bull. Am. Meteorol. Soc., 87, 343–360.

Miller, S. M., Wofsy, S. C., Michalak, A. M., Kort, E. A., Andrews, A. E., Biraud, S. C., ... & Sweeney, C. (2013). Anthropogenic emissions of methane in the United States. Proceedings of the National Academy of Sciences, 110(50), 20018-20022.

Miller, S. M., Worthy, D. E., Michalak, A. M., Wofsy, S. C., Kort, E. A., Havice, T. C., ... & Zhang, B. (2014). Observational constraints on the distribution, seasonality, and environmental predictors of North American boreal methane emissions. Global Biogeochemical Cycles, 28(2), 146-160.

Mortsch, L. D. (1990). Eastern Canadian Boreal and Subarctic Wetlands: A Resource Document, Atmospheric Environment Service, Environment Canada and Canadian Institute for Research in Atmospheric Chemistry, Toronto.

Nakazawa, T., Aoki, S., Murayama, S., Fukabori, M., Yamanouchi, T., Murayama, H., Shiobara, M., Hashida, G., Kawaguchi, S. and Tanaka, M. (1991a). The concentration of atmospheric carbon dioxide at Japanese Antarctic station, Syowa, Tellus, 43B, 126–135.

Nakazawa, T., Ishizawa, M., Higuchi, K. A. Z., & Trivett, N. (1997). Two curve fitting methods applied to CO_2 flask data. Environmetrics, 8(3), 197-218.

Nakazawa, T., Miyashita, K., Aoki, S. and Tanaka, M. (1991b). Temporal and spatial variations of upper tropospheric and lower stratospheric carbon dioxide, Tellus, 43B, 106–117.

Nakazawa, T., Morimoto, S., Aoki, S. and Tanaka, M. (1993). Time and space variations of the carbon isotopic ratio of tropospheric carbon dioxide over Japan, Tellus, 45B, 258–274.

Nakazawa, T., Murayama, S., Miyashita, K., Aoki, S. and Tanaka, M. (1992). Longitudinally different variations of lower tropospheric carbon dioxide concentrations over the North Pacific Ocean, Tellus, 44B, 161–172.

Nehrkorn, T., Eluszkiewicz, J., Wofsy, S. C., Lin, J. C., Gerbig, C., Longo, M., and Freitas, S. (2010). Coupled weather research and forecasting–stochastic time-inverted Lagrangian transport (WRF–STILT) model. Meteor. Atmos. Phys., 107, 51–64.

Oda, T. and Maksyutov, S. (2011) A very high-resolution (1 km x 1 km) global fossil fuel CO_2 emission inventory derived using a point source database and satellite observations of nighttime lights. Atmos. Chem. Phys., 11, 543-556, doi:10.5194/acp-11-543-2011.

Olivier, J. G. J., Van Aardenne, J. A., Dentener, F., Ganzeveld, L., and Peters, J. A. H. W. (2005). Recent trends in global greenhouse gas emissions: Regional trends and spatial distribution of key sources, in Non-CO_2 Greenhouse Gases (NCGG4), edited by A. van Amstel, pp. 325 – 330, Millpress, Rotterdam, Netherlands.

Pacala SW, Hurtt GC, Baker D, Peylin P, Houghton RA, Birdsey RA, Heath L, Sundquist ET, Stallard RF, Ciais P, et al. (2001) Science 292:2316–2320.

Pacala, S. W., Hurtt, G. C., Baker, D., Peylin, P., Houghton, R. A. et al. (2001), Consistent land- and atmosphere-based U.S. carbon sink estimates. Science 292, 2316–2320.

Pathmathevan, M., Wofsy, S. C., Matross, D. M., Xiao, X., Lin, J. C. and co-authors. (2006). A satellite-based biosphere parameterization for net ecosystem CO_2 exchange: Vegetation Photosynthesis and Respiration Model (VPRM). http://people.deas.harvard.edu/˜swofsy/VPRM˙submitted.zip.

Patra, P. K., et al. (2008), TransCom model simulations of hourly atmospheric CO_2: Analysis of synoptic-scale variations for the period 2002–2003, Global Biogeochem. Cycles, 22, GB4013, doi:10.1029/2007GB003081.

Pattey, E., I. B. Strachan, R. L. Desjardins, and J. Massheder (2002), Measuring nighttime CO_2 flux over terrestrial ecosystems using eddy covariance and nocturnal boundary layer methods, Agric. For. Meteorol., 113, 145– 158.

Peters, W., Jacobson, A. R., Sweeney, C., Andrews, A. E., Conway, T. J., Masarie, K., ... & Tans, P. P. (2007). An atmospheric perspective on North American carbon dioxide exchange: CarbonTracker. Proceedings of the National Academy of Sciences, 104(48), 18925-18930, with updates documented at http://carbontracker.noaa.gov

Peters, W., Jacobson, A. R., Sweeney, C., Andrews, A. E., Conway, T. J., Masarie, K., ... & Tans, P. P. (2007). An atmospheric perspective on North American carbon dioxide exchange: CarbonTracker. Proceedings of the National Academy of Sciences, 104(48), 18925-18930.

Pisso, I., Marecal, V., Legras, B., and Berthet, G. (2010). Sensitivity of ensemble Lagrangian reconstructions to assimilated wind time step resolution. Atmos. Chem. Phys., 10, 3155–3162.

Potosnak, M. J., Wofsy, S. C., Denning, A. S., Conway, T. J., Munger, J. W., & Barnes, D. H. (1999). Influence of biotic exchange and combustion sources on atmospheric CO_2 concentrations in New England from observations at a forest flux tower. Journal of Geophysical Research: Atmospheres (1984–2012), 104(D8), 9561-9569.

Potter, C. S. and Klooster, S. A. (1997) Global model estimates of carbon and nitrogen storage in litter and soil pools: Response to change in vegetation quality and biomass allocation. Tellus, 49, doi:10.1034/j.1600-0889.49.issue1.1.x.

Potter, C. S., Davidson, E. A., and Verchot, L. (1996) Estimation of global biogeochemical controls and seasonality in soil methane consumption. Chemosphere, 32(11), 2219–2246.

Potter, C. S., Klooster, S. A., and Brooks, V. (1999) Interannual variability in terrestrial net primary production: Exploration of trends and controls on regional to global scales. Ecosystems, 2, 36–48, doi:10.1007/s100219900056.

Price, D.T., Alfaro, R.I., Brown, K.J., Flannigan, M.D., Fleming, R.A., Hogg, E.H., Girardin, M.P., Lakusta, T., Johnston, M., McKenney, D.W., Pedlar, J., Stratton, T., Sturrock, R., Thompson, I., Trofymow, J.A., and Venier, L.A. (2013). Anticipating the consequences of climate change for Canada's boreal forest ecosystems. Environ. Rev. 21(4): 322-365, 10.1139/er-2013-0042.

Pugh, T. A. M., et al. (2012). A Lagrangian model of air-mass photochemistry and mixing using a trajectory ensemble: The Cambridge Tropospheric Trajectory model of Chemistry and Transport (CiTTyCAT) version 4.2, *Geosci. Model Dev., 5, 193-221*.

Raupach, M. R. (1995), Vegetation-atmosphere interaction and surface conductance at leaf, canopy and regional scales, Agric. Forest Meteorol., 73, 151– 170.

Raupach, M. R. (2000), Equilibrium evaporation and the convective boundary layer, Boundary Layer Meteorol., 96, 107– 141.

Raupach, M. R. (2001), Combination theory and equilibrium evaporation, Q. J. R. Meteorol. Soc., 127, 1149– 1181.

Raupach, M. R., O. T. Denmead, and F. X. Dunin (1992), Challenges in linking atmospheric CO_2 concentrations to fluxes at local and regional scales, Aust. J. Botany, 40, 697– 716.

Reynolds, O. (1895). On the dynamical theory of incompressible viscous fluids and the determination of the criterion, *Philos. Trans. R. Soc. London, Ser. A, 186*, 123-164.

Riley, J.L. (1982). Hudson Bay Lowland floristic inventory, wetland catalogue, and conservation strategy, Nat. Can., 109, 543-555.

Roulet, N. T., Jano, A., Kelly, C. A., Klinger, L. F., Moore, T. R., Protz, R., Ritter, J. A., and Rouse, W. R. (1994) Role of the Hudson Bay lowland as a source of atmospheric methane. J. Geophys. Res., 99(D1), 1439-1454.

Rouse, W. R. (1991). Impacts of Hudson Bay on the terrestrial climate of the Hudson Bay Lowlands, Arctic Alpine Res. 23, 24–30.

Saeki, T., et al. (2013), Carbon flux estimation for Siberia by inverse modeling constrained by aircraft and tower CO_2 measurements, J. Geophys. Res. Atmos., 118, 1100–1122, doi:10.1002/jgrd.50127.

Salby, M. L. (2012). Physics of the Atmosphere and Climate, *Cambridge Univ. Press, New York.*

Saucier, F. J. and Dionne, J. (1998). A 3-D coupled ice-ocean model applied to Hudson Bay, Canada: The seasonal cycle and time-dependent climate response to atmospheric forcing and runoff. J. Geophys. Res. 103, 27689–27705.

Schmid, H. P. (1997). Experimental design for flux measurements: matching scales of observations and fluxes. Agricultural and Forest Meteorology, 87(2), 179-200.

Schmid, H. P., & Oke, T. R. (1990). A model to estimate the source area contributing to turbulent exchange in the surface layer over patchy terrain. Quarterly Journal of the Royal Meteorological Society, 116(494), 965-988.

Schut, P., Shields, J., Tarnocai, C., Coote, D., and Marshall, I. (1994). Soil landscapes of Canada—An environmental reporting tool, paper presented at Canadian Conference on GIS Proceedings, Can. Inst. of Surv. And Mapping, Ottawa.

Scire, J. S., Strimaitis, D. G., and Yamartino, R. J. (2000). A User's Guide for the CALPUFF Dispersion Model (Version 5.0), *521 pp., Earth Tech, Inc., Concord, Mass*.

Seaman, N. L. (2000). Meteorological modeling for air-quality assessments, *Atmos. Environ., 34, 2231-2259*.

Seibert, P., and Frank, A. (2004). Source-receptor matrix calculation with a Lagrangian particle dispersion model in backward mode, Atmos. Chem. Phys., 4, 51–63.

Steinacker, R. (1984). Airmass and frontal movement around the Alps. Rivista di Meteorologia Aeronautica 44, 85-93.

Stirling, I. and Derocher, A. E. (1993) Possible impacts of climatic warming on polar bears. Arctic 46, 240–245.

Stirling, I., Lunn, N. J., and Iacozza, J. (1999) Long-term trends in the population ecology of polar bears in western Hudson Bay in relation to climatic change. Arctic 52, 294–306.

Stohl, A., and Wotawa G. (1995). A method for computing single trajectories representing boundary layer transport, *Atmos. Environ., 29, 3235-3238*.

Stohl, A. (1996a). On the use of trajectories for establishing source-receptor relationships of air pollutants. Ph.D. Thesis, University of Vienna.

Stohl, A. (1996b) Trajectory statistics–a new method to establish source-receptor relationships of air pollutants and its application to the transport of particulate sulfate in Europe. Atmospheric Environment 30, 579-587.

Stohl, A. (1998a). Computation, accuracy and applications of trajectories—a review and bibliography. Atmospheric Environment, 32(6), 947-966.

Stohl, A., Hittenberger, M., and Wotawa, G. (1998b). Validation of the Lagrangian particle dispersion model FLEXPART against large scale tracer experiment data, Atmos. Environ., 32, 4245–4264.

Stohl, A. and Thomson, D. J. (1999) A density correction for Lagrangian particle dispersion models, Bound.-Lay. Meteorol., 90, 155–167.

Stohl, A., Haimberger, L., Scheele, M. P., and Wernli, H. (2001). An intercomparison of results from three trajectory models. Meteor. Appl., 8, 127–135.

Stohl, A., Forster, C., Eckhardt, S., Spichtinger, N., Huntrieser, H., Heland, J., Schlager, H., Wilhelm, S., Arnold, F., and Cooper, O. (2003). A backward modeling study of intercontinental pollution transport using aircraft measurements, J. Geophys. Res., 108 (D12), 4370, doi:10.1029/2002JD002862.

Stohl, A., Forster, C., Frank, A., Seibert, P., and Wotawa, G. (2005). Technical note: The Lagrangian particle dispersion model FLEXPART version 6.2., *Atmos. Chem. Phys., 5*, 2461–2474.

Stohl, A., Seibert, P., Arduini, J., Eckhardt, S., Fraser, P., Greally, B. R., Lunder, C., Maione, M., Mühle, J., O'Doherty, S., Prinn, R. G., Reimann, S., Saito, T., Schmidbauer, N., Simmonds, P. G., Vollmer, M. K., Weiss, R. F., and Yokouchi, Y. (2009). An analytical inversion method for determining regional and global emissions of greenhouse gases: Sensitivity studies and application to halocarbons, Atmos. Chem. Phys., 9, 1597-1620, doi:10.5194/acp-9-1597-2009.

Strong, J., Whyatt, J. D., Hewitt, C. N., and Derwent, R. G. (2010). Development and application of a Lagrangian model to determine the origins of ozone episodes in the UK, *Atmos. Environ.*, *44*, *631–641*.

Styles, J. M., J. Lloyd, D. Zolotoukhine, K. A. Lawton, N. Tchebakova, R. J. Francey, A. Arneth, D. Salamakho, O. Kolle, and E.-D. Schulze (2002), Estimates of regional surface carbon dioxide exchange and carbon and oxygen isotope discrimination during photosynthesis from concentration profiles in the atmospheric boundary layer, Tellus, Ser. B, 54, 768– 783.

Sulman, M. H. M., Huntley, H. S., Lipphardt Jr., B. L., and Kirwan Jr., A. D. (2012). Out of flatland: Three-dimensional aspects of Lagrangian transport in geophysical fluids, in *Lagrangian Modeling of the Atmosphere, Geophys. Monogr. Ser., Vol. 200, Amer. Geophys. Union*, 349 pp, doi:10.1029/2012GM001279.

Tans, P. P., Bakwin, P. S., & Guenther, D. W. (1996). A feasible global carbon cycle observing system: a plan to decipher today's carbon cycle based on observations. Global change biology, 2(3), 309-318.

Tans, P. P., Fung, I. Y., & Takahashi, T. (1990). Observational contrains on the global atmospheric CO_2 budget. Science, 247(4949), 1431-1438.

Tans, P.P. 1991. An observational strategy for assessing the role of terrestrial ecosystems in the global carbon cycle: scaling down to regional levels. In: Scaling processes between leaf and landscape levels (ed. J. Ehleringer and C. Field). Academic Press, San Diego.

Taylor, G. I. (1921). Diffusion by continuous movements. *Proc. London Math. Soc., s2-20, 196-212*.

Thomson, D. J., and Wilson, J. D. (2012). History of Lagrangian stochastic models for turbulent dispersion, in *Lagrangian Modeling of the Atmosphere, Geophys. Monogr. Ser., Vol. 200, Amer. Geophys. Union*, 349 pp, doi:10.1029/2012GM001238.

Thomson, D. J., Physick, W. L., and Maryon, R. H. (1997) Treatment of interfaces in random walk dispersion models, J. Appl. Meteorol., 36, 1284–1295.

Trenberth, K.E., Jones, P.D., Ambenje, P., Bojariu, R., Easterling, D., Klein Tank, A., Parker, D., Rahimzadeh, F., Renwick, J.A., Rusticucci, M., Soden, B., and Zhai, P. (2007). Observations: surface and atmospheric climate change [online]. In Climate change 2007: the physical science basis. Contribution of Working Group I to the Fourth Assessment Report of the Intergovernmental Panel on Climate Change. Edited by S. Solomon, D. Qin, M. Manning, Z. Chen, M. Marquis, K.B. Averyt, M. Tignor, and H.L. Miller. Cambridge University Press, Cambridge and New York. pp. 235–336. Available from http://www.ipcc.ch/pdf/assessment-report/ar4/wg1/ar4-wg1-chapter3.pdf.

Trivett, N. and Köhler, A. (1999). Guide on sampling and analysis techniques for chemical constituents and physical properties in air and precipitation as applied at stations of the Global Atmosphere Watch: Carbon Dioxide. WMO Global Atmosphere Watch, No. 134.

Vogelezang, D. H. P. and Holtslag, A. A. M. (1996) Evaluation and model impacts of alternative boundary-layer height formulations. Boundary Layer Meteorol., 81, 245– 269.

Walcek, C. J. (2002). Effects of wind shear on pollution dispersion, *Atmos. Environ., 36, 511-517*.

Walko, R. L., Tremback, C. J., and Bell, M. J. (2001). HYPACT User's Guide, 113 pp., ASTER Div., Mission Res. Corp., Fort Collins, Colo.

Wang, J. S., McElroy, M. B., Logan, J. A., Palmer, P. I., Chameides, W. L., Wang, Y., and Megretskaia, I. A. (2008). A quantitative assessment of uncertainties affecting estimates of global mean OH derived from methyl chloroform observations, J. Geophys. Res., 113, D12302, doi:10.1029/2007JD008496, 2008.

Wiken, E. B. (compiler). (1986) Terrestrial Ecozones of Canada. Ecological Land Classification Series No. 19. Environment Canada, Hull, Que. 26 pp. and map.

Wiken, E. B., David Gauthier, Ian B. Marshall, Ken Lawton, and Harry Hirvonen (1996). A perspective on Canada's Ecosystems: An overview of the Terrestrial and Marine Ecozones. Occasional paper N. 14, Canadian Council on Ecological Areas, Ottawa, Ont. 95 pp.

Wilson, J. D., Flesch, T. K., and Crenna B. P. (2012). Estimating surface-air gas fluxes by inverse dispersion using a backward Lagrangian stochastic trajectory model, in *Lagrangian Modeling of the Atmosphere, Geophys. Monogr. Ser., Vol. 200, Amer. Geophys. Union*, 349 pp, doi:10.1029/2012GM001269.

Wofsy, S. C. and Harriss, R. C. 2002. The North American Carbon Program (NACP). Report to the Interagency Working Group of the US Global Change Research Program. National Center for Atmospheric Research, Boulder, CO, USA. http://www.esig.ucar.edu/nacp/

Wong, C. S., Chan, Y. H., Page, J. S., Bellegay, R. D., & Pettit, K. G. (1984). Trends of atmospheric CO_2 over Canadian WMO background stations at ocean weather station P, Sable Island, and Alert. Journal of Geophysical Research: Atmospheres (1984–2012), 89(D6), 9527-9539.

Worthy, D. E .J., Levin, I., Trivett, N. B. A., Kuhlmann, A. J., Hopper, J. F., and Ernst, M. K. (1998). Seven years of continuous methane observations at a remote boreal site in Ontario, Canada, J. Geophys. Res. 103, 15, 995-16, 007.

Yee, Stanley (2008). The role of representative terrain units in the water balance of a polygonal peat plateau catchment in Churchill, Manitoba. Unpublished M.Sc. Thesis York University.

Zeng N, Mariotti A, Wetzel P (2005) Global Biogeochem Cycles 19:GB002273.

Zhao, C. L., Tans, P. P., & Thoning, K. W. (1997). A high precision manometric system for absolute calibrations of CO2 in dry air. Journal of Geophysical Research: Atmospheres (1984–2012), 102(D5), 5885-5894.

Zhao, C. L., & Tans, P. P. (2006). Estimating uncertainty of the WMO mole fraction scale for carbon dioxide in air. Journal of Geophysical Research: Atmospheres (1984–2012), 111(D8).

Zhao, C., Andrews, A. E., Bianco, L., Eluszkiewicz, J., Hirsch, A., MacDonald, C., Nehrkorn, T., and Fischer, M. L. (2009) Atmospheric inverse estimates of methane emissions from Central California. J. Geophys. Res., 114, D16302, doi:10.1029/2008JD011671.